UNIVERSITY OF CALGARY

Applications of atomic ensembles for photonic quantum information processing and fundamental tests of quantum physics

by

Mohammadsadegh Khazali

A THESIS

SUBMITTED TO THE FACULTY OF GRADUATE STUDIES

IN PARTIAL FULFILLMENT OF THE REQUIREMENTS FOR THE

DEGREE OF DOCTOR OF PHILOSOPHY

PHYSICS AND ASTRONOMY

CALGARY, ALBERTA

January, 2016

Abstract

Quantum optics provides tools for the accurate control of light using atoms and also for manipulating atomic states using light. These techniques are being used for many applications, including quantum information processing and the generation of exotic quantum states. This thesis contains proposals for implementing a photonic quantum memory and a photon-photon gate, which are essential elements of photonic quantum information processing. Furthermore it proposes a scheme for the creation of many-body entangled states.

First a proposal for a new quantum memory protocol, called the atomic frequency sweep quantum memory, is presented. A two-level polariton model is derived that explains the coherent storage and retrieval of light through the manipulation of the atomic resonance frequency.

This is followed by a scheme for a deterministic photonic controlled-PHASE gate based on the strong interaction between two stationary collective Rydberg excitations in an atomic ensemble. Distortion effects caused by nonuniform interaction are quantified and compensation techniques for these effects are proposed.

Finally a proposal is presented that uses Rydberg dressing for the generation of energy cat states in an atomic medium, i.e. superposition states of all the atoms being in the ground or excited state, where these two states are connected by an optical transition and thus have a significant difference in energy. Considering the fragility of the state, the effects of many different imperfections and decoherence sources are quantified. The resulting cat state would allow testing of energy decoherence models with greatly improved sensitivity.

List of published papers

-H Kaviani*, M Khazali*, R Ghobadi, E Zahedinejad, K Heshami and C Simon, *"Quantum storage and retrieval of light by sweeping the atomic frequency"*, New J. Phys. **15** 085029 (2013).

* These authors contributed equally to this work.

-M. Khazali, K. Heshami, C. Simon, *"Photon-photon gate via the interaction between two collective Rydberg excitations"*, Phys. Rev. A **91**, 030301(Rapid Communication) (2015).

-M. Khazali, H. W. Lau, A. Humeniuk, C. Simon, *"Large Energy Superpositions via Rydberg Dressing"*, arXiv:1509.01303v2 (2015) (To appear in Phys. Rev. A).

Acknowledgements

I would like to express my special appreciation to my advisor Professor Christoph Simon, for his endless support, guidance, patience, enthusiasm, and insight in every step of my PhD studies. I will always be indebted to him for recognizing my talent and helping me to become an independent researcher.

I benefited from the useful class of Professor Barry Sanders, and also his comments in the supervisory meetings. I would like to thank the scholars that I meat in conferences for useful discussions, Vladan Vuletic, Sebastian Hufferberth, Philippe Grangier, Charles Adams, Alexey Gorshkov, Tilman Pfau, and Mark Saffman.

I should thank university's undergrad director, Michael Wieser, who let me have a wonderful experience of teaching physics to 750 students at the university.

I would like to acknowledge working with my collaborators, Adam Humeniuk, Hamid Kaviani, Dr. Khabat Heshami, and Hon-Wai Lu. I also thank Dr. Bing He, Dr. Adam DSouza, Dr. Daniel Oblak and Dr. Farid Ghobadi for useful discussions. I should also thank the constant support of the kind graduate administrator of the department, Tracy Korsgaard.

I would like to thank my parents for allowing me to realize my potentials. All the support they have provided me over the years was the greatest gift anyone has ever given me. Words cannot express my feelings, nor my thanks for all their sacrifices in my life. I would like to thank my beautiful sister for all her kindness. I would like to thank my Father-in-law and specially Mother-in-law for her help and support over the first few months that I became father. Just saying thank you will never repay your kindness. I would like to thank my beautiful wife Samaneh, for her love, care and encouragement during different stages of my life. Her support was in the end what made this dissertation possible. I cannot imagine my life without you! Last but not least, I would like to thank my little one that I was missing

the most when I was at school. You have been my motivation for hard working long before we met.

Table of Contents

List of Tables

List of Figures and Illustrations

List of Symbols, Abbreviations and Nomenclature

Symbol	Definition
AFS	Atomic Frequency Sweep
BBR	Black Body Radiation
CRIB	Controled Reversible Inhomogeneous Broadening
DSP	dark state polariton
EIT	Electromagnetically Induced Transparency
QKD	quantum key distribution
SVE	Slowly Varying Envelope
Δ	Detuning
Ω	Rabi Frequency

Chapter 1

Introduction

The counter-intuitive concepts of quantum mechanics have inspired a range of new ideas and technologies over the last decades. Quantum computation [1] is much faster than classical computation for certain tasks such as factorization [2], searching [3] and the simulation of quantum systems [4, 5, 6]. The exponential speedup of factorization with quantum computers poses a threat to current encryption protocols. This can be addressed by the unbreakable security of quantum key distribution, which comes from the fact that measurements disturb the quantum state; this can be used to reveal the presence of an eavesdropper [7, 8, 9]. In addition to quantum computation and communication, the field of quantum metrology has demonstrated very high precision measurements that are out of reach for classical devices [10, 11, 12].

The key elements that enable these improvements are the concepts of superposition and entanglement, which were recognized already in the early years of quantum mechanics [13, 14, 15]. A quantum system can be in a linear superposition of more than one distinct state, e.g. a particle can be in two places at the same time. Under a unitary evolution this superposition can interfere like in the electron double slit experiment. Superposition can also involve states of more than one particle, in which case the particles can be in correlated states and thus become entangled. Entangled states can not be described by identifying the individual states of each system. For example, in a two-spin Bell state $(|\uparrow\rangle_1|\uparrow\rangle_2 + |\downarrow\rangle_1|\downarrow\rangle_2)/\sqrt{2}$, the state of one particle depends on the state of the other.

Quantum theory does not distinguish between the microscopic and macroscopic worlds. This can be seen in Scrödinger's famous thought experiment, which brings a cat into a superposition state of being dead and alive at the same time [15]. However, quantum concepts like

superposition have not been observed at the macroscopic scale. This is typically interpreted as being due to the increasing fragility of quantum superposition at larger scales because of environment-induced decoherence [16, 17, 18]. However, there are also spontaneous wave-function collapse models (e.g. trace dynamics and gravity induced collapse models) that can reproduce quantum behavior for microscopic systems and classical behavior for macroscopic systems, while making predictions that are different from both quantum and classical physics in the mesoscopic range [19]. The creation of mesoscopic superpositions involving physical degrees of freedom such as spatial separation and energy can be used as an experimental test of such collapse models.

The implementation of quantum technology requires the practical realization and manipulation of the mentioned effects in a quantum system. The main difficulty is in the interaction of the system with the environment, which destroys the coherence and entanglement. In the past decades dramatic progress in quantum control has been achieved in different platforms including quantum optics and atomic physics.

Photons are ideal carriers of quantum information due to their fast transmission nature and weak interaction with the environment, which increases their coherence time. However for the same reason they are not an ideal platform for quantum memories and deterministic two qubit gates where one needs stationary qubits and large photon-photon interaction respectively. Atomic media on the other hand are an ideal platform for both tasks and could be used as an interface. Therefore on demand light-matter and matter-matter interaction, which allows the coherent transfer of quantum information between photonic and atomic qubits and strong non-linearity between the two qubits, is essential in the realization of photonic quantum information technology. Implementation of quantum memory is essential in photonic quantum information tasks such as creating deterministic single photon sources, synchronizing the steps in quantum computation and implementation of quantum repeaters for long range quantum communications [20, 21, 22]. Implementation of photonic two qubit

gates could specifically improve quantum repeaters performance and also complete a set of universal gates as a platform for quantum computation.

Efficient quantum interfaces require strong light-matter interaction at the single quantum level. This can be achieved by trapping both atoms and electromagnetic field in high finesse cavity [23, 24, 25, 26, 27]. An experimentally less demanding way that is easier to scale up, is to enhance coupling by using a large atomic ensemble [28, 29]. As the number of atoms in the ensemble increase the probability that the incident photon fails to interact with the atoms reduces exponentially. The focus of this thesis is entirely on the light interaction with atomic ensembles. In atomic ensembles there are two different protocols for on demand control of atom-photon interaction. Some protocols for quantum memory introduce a control beam in a three-level atomic configuration to manipulate the interaction between the signal pulse and the atoms (e.g. EIT [30], and Raman schemes [31, 32, 33]). Other protocols use the phenomenon of photon echo [34] to achieve controlled atom-photon interaction (e.g. AFC [35], CRIB [36], and GEM [37]). In this type of memory the atom-photon interaction is controlled by a dephasing-rephasing process owing to the inhomogeneous broadening of the medium. There have been different schemes towards the realization of deterministic two-photon gates using atomic interface [38, 39, 40, 41, 42, 43, 44] where the most successful one is based on Rydberg interaction [45].

As much as atoms can be used to create and manipulate the quantum state of light coherently, modern optical techniques provide a tool for the coherent manipulation of atoms using light. Atomic media not only are promising platform for quantum computation [44] but are also appealing for the creation of large many-body quantum states [46, 47, 48, 49, 50, 51, 52, 53, 54, 55].

Laser excitation of atoms to very high principal number states (known as Rydberg states) with large dipole moments, results in a strong interaction between the excited atoms[44], see Sec. 5.8. This strong switchable interaction and its resulting phenomena like Rydberg

Blockade (which prevents more than one excitations within Blockade radius, see Sec. 5.9) and a plateau type interaction caused by off-resonant excitation to the Rydberg level (see Sec. 5.10) have been widely used in variety of applications, see sec. 5.2. Of special interest in the context of this thesis are applications of Rydberg states for the realization of photonic gates [44, 45, 56, 57, 58, 59] and for the generation of many body entangled states [60, 61, 62].

In this thesis, we use the light-matter and Rydberg interaction in atomic ensembles to propose new schemes for photonic quantum information processing and for testing collapse models. The thesis is organized as follows.

-Chapter 2 discusses basic concepts of atom-field interaction. These techniques can be applied for manipulation of the atomic states coherently using optical field and also the quantum state of light using atoms.

-Chapter 3 is a brief introduction about quantum communication and quantum memories.

-Chapter 4 introduces a quantum memory protocol that helps in unification and better understanding of two other existing protocols. The results of this project are published in:

H Kaviani*, M Khazali*, R Ghobadi, E Zahedinejad, K Heshami and C Simon, "Quantum storage and retrieval of light by sweeping the atomic frequency", New J. Phys. 15 085029 (2013) * These authors contributed equally to this work.

-Chapter 5 is an introduction of Rydberg physics, where the exaggerated properties of highly excited atoms are introduced and their different interaction types are discussed.

-Chapter 6 proposes a controlled-phase gate between stored photons, where non-linearity comes from many-body interaction between collective excitation of Rydberg atoms. The results of this project are published in:

M. Khazali, K. Heshami, C. Simon, "Photon-photon gate via the interaction between two collective Rydberg excitations", Phys. Rev. A 91, 030301(Rapid Communication) (2015)

-In Chapter 7 a scheme is proposed to create large energy superposition based on Rydberg dressing interaction [64], allowing tests of energy decoherence models with greatly improved

sensitivity. The results of this project will be appear in Phys. Rev. A and can be find in:

M. Khazali, H. W. Lau, A. Humeniuk, C. Simon, "Large Energy Superpositions via Rydberg Dressing", arXiv:1509.01303v2 (2015) (to appear in PRA)

Chapter 2

Atom-Field Interaction

2.1 Preface

Modern optical techniques provide a tool for accurate controlling of light using atoms and also manipulating atomic states using light. A strong laser field can be applied for manipulating the atomic populations, off resonant dressing of the states, optical trapping, and also creating an induced transparency. Section 2.2 explains this interaction and corresponding atomic dynamics, which will be used widely in this thesis. The interaction between atoms and a single photon is explored in section 2.3. In addition the propagation dynamics of a single photon and the coupled atomic polarization field is discussed, which will be used in chapter 4.

2.2 Interaction Between Two Level Atom and Classical Field

An electron with charge q and mass m within the atomic potential of $V(r)$ interacts with an external electric field under the minimal coupling Hamiltonian [65]

$$H = \frac{1}{2m}[\mathbf{p} - q\mathbf{A}(\mathbf{r},t)]^2 + qU(\mathbf{r},t) + V(r), \tag{2.1}$$

where $\mathbf{p}$ is the canonical momentum operator, $\mathbf{A}(\mathbf{r},t)$ and $U(\mathbf{r},t)$ are the vector and scalar potentials of external field. Considering the electrons wave-function $\psi(\mathbf{r},t)$, applying a local gauge transformation of

$$\psi(\mathbf{r},t) \rightarrow \psi(\mathbf{r},t)e^{i\chi(\mathbf{r},t)}, \tag{2.2}$$

preserves its local probability $P(\mathbf{r},t) = |\psi(\mathbf{r},t)|^2$ while it modifies the Schrödinger equation by the following transformation [65]

$$\mathbf{A}(\mathbf{r},t) \rightarrow \mathbf{A}(\mathbf{r},t) + \frac{\hbar}{q}\nabla\chi(\mathbf{r},t) \tag{2.3}$$

$$U(\mathbf{r},t) \rightarrow U(\mathbf{r},t) - \frac{\hbar}{q}\frac{\partial\chi(\mathbf{r},t)}{\partial t}. \tag{2.4}$$

Since the size of an atom is much smaller than the wavelength of the laser field ($\mathbf{k}.\mathbf{r} \ll 1$), dipole approximation states that spatial variation of the field is negligible over atomic extension $\mathbf{A}((\mathbf{r}_0+\mathbf{r}),t) \approx \mathbf{A}(\mathbf{r}_0,t)$, where $\mathbf{r}$ is the position of electron with respect to the nucleus at $\mathbf{r}_0$. By applying a gauge transformation of $\chi(\mathbf{r},t) = -e\mathbf{A}(\mathbf{r}_0,t).\mathbf{r}/\hbar$ and considering the radiation gauge regime where $U(\mathbf{r},t) = 0$ and $\nabla.\mathbf{A} = 0$, Schrödinger equation will be

$$i\hbar\dot{\psi}(\mathbf{r},t) = [H_{atom} + H_{int}]\psi(\mathbf{r},t), \tag{2.5}$$

where

$$H_{atom} = \frac{p^2}{2m} + V(r) \tag{2.6}$$

$$H_{int} = -q\mathbf{r}.\mathbf{E}(\mathbf{r},t), \tag{2.7}$$

is the atomic and interaction Hamiltonians and $E = -\dot{A}$ is the electric field.

Let us consider $|e\rangle$ and $|g\rangle$ as eigenstates of the atomic Hamiltonian H_{atom}, with corresponding energies of $E_g = 0$ and $E_e = \hbar\omega_e$. By the completeness relation ($|e\rangle\langle e| + |g\rangle\langle g| = \mathbf{1}$) we can write the atomic Hamiltonian in the atomic bases as

$$\begin{aligned}\hat{H}_{atom} &= (|e\rangle\langle e| + |g\rangle\langle g|)\hat{H}_{atom}(|e\rangle\langle e| + |g\rangle\langle g|) \\ &= \hbar\omega_e\hat{\sigma}_{ee},\end{aligned} \tag{2.8}$$

where $\hat{\sigma}_{ee} = |e\rangle\langle e|$ is the projection operator. Considering the interaction of atoms with a laser field of

$$\mathbf{E}(\mathbf{r},t) = \frac{e^{i(\omega_L t - \mathbf{k}.\mathbf{r})} + e^{-i(\omega_L t - \mathbf{k}.\mathbf{r})}}{2}\mathbf{E_0}, \tag{2.9}$$

the interaction Hamiltonian in the atomic bases can be written as

$$\hat{H}_{int} = \langle g|q\hat{\mathbf{r}}.\mathbf{E}(\hat{\mathbf{r}}_0,t)|e\rangle\hat{\sigma}_{ge} + \langle e|q\hat{\mathbf{r}}.\mathbf{E}(\hat{\mathbf{r}}+0,t)|g\rangle\hat{\sigma}_{eg} + \langle g|q\hat{\mathbf{r}}.\mathbf{E}(\hat{\mathbf{r}}_0,t)|g\rangle\hat{\sigma}_{gg} + \langle e|q\hat{\mathbf{r}}.\mathbf{E}(\hat{\mathbf{r}}_0,t)|e\rangle\hat{\sigma}_{ee}. \tag{2.10}$$

Permanent dipoles $\langle e|\hat{\mathbf{r}}|e\rangle = 0$, $\langle g|\hat{\mathbf{r}}|g\rangle = 0$ are zero for the atoms in free space and isolated from external fields due to the parity. Applying the unitary transformation of ($\hat{U} = e^{-i\omega_a t\hat{\sigma}_{ee}}$), the Hamiltonian in the interaction picture looks like

$$\hat{H}_0^I = \frac{\hbar\Omega}{2}(\hat{\sigma}_{eg}e^{i(\omega_a+\omega_L)t} + \hat{\sigma}_{ge}e^{-i(\omega_a+\omega_L)t} + \hat{\sigma}_{ge}e^{-i\Delta t} + \hat{\sigma}_{eg}e^{i\Delta t}) \tag{2.11}$$

where $\Omega = \frac{\mathbf{E_0}.\mathbf{d}}{\hbar}$ is called the Rabi frequency and $\mathbf{d} = \langle g|q\mathbf{r}|e\rangle$ is the dipole matrix element (which can be considered real without the loss of generality) and $\Delta = \omega_e - \omega_L$ is detuning. In the regime of weak coupling $\Omega << \omega_e$ we can apply the "rotating wave approximation" to simplify the Hamiltonian. This approximation states that fast oscillating terms with frequencies $\omega_e + \omega_L >> \Delta, \Omega$ will average to zero on any interesting time scales of the system (Δ^{-1} or Ω^{-1}) and therefore can be neglected.

To partially remove the time dependence we apply another unitary transformation $\hat{U} = e^{i\Delta\hat{\sigma}_{ee}t}$ to equation 2.11 to find

$$\hat{H} = \hbar\Delta\hat{\sigma}_{ee} + \frac{\hbar\Omega}{2}[\hat{\sigma}_{eg} + \hat{\sigma}_{ge}]. \tag{2.12}$$

Considering an initial state defined in the Hilbert space of $\{|e\rangle, |g\rangle\}$ i.e.

$$|\psi(t)\rangle = C_g(t)|g\rangle + C_e(t)|e\rangle, \tag{2.13}$$

with initial amplitudes of $C_e(0) = 0$ and $C_g(0) = 1$; evolution of the excited state amplitude ($C_e(t)$) under the Hamiltonian of Eq. 2.12 will be

$$C_e(t) = i\frac{\Omega}{\tilde{\Omega}}e^{-\frac{i\Delta t}{2}}\sin(\frac{\tilde{\Omega}t}{2}). \tag{2.14}$$

Effective Rabi frequency in this equation is presented by $\tilde{\Omega} = \sqrt{\Delta^2 + \Omega^2}$. Time evolution of excitation probability is plotted in Fig. 2.1, which indicates that increasing the detuning reduces the excitation probability and increases the effective Rabi frequency.

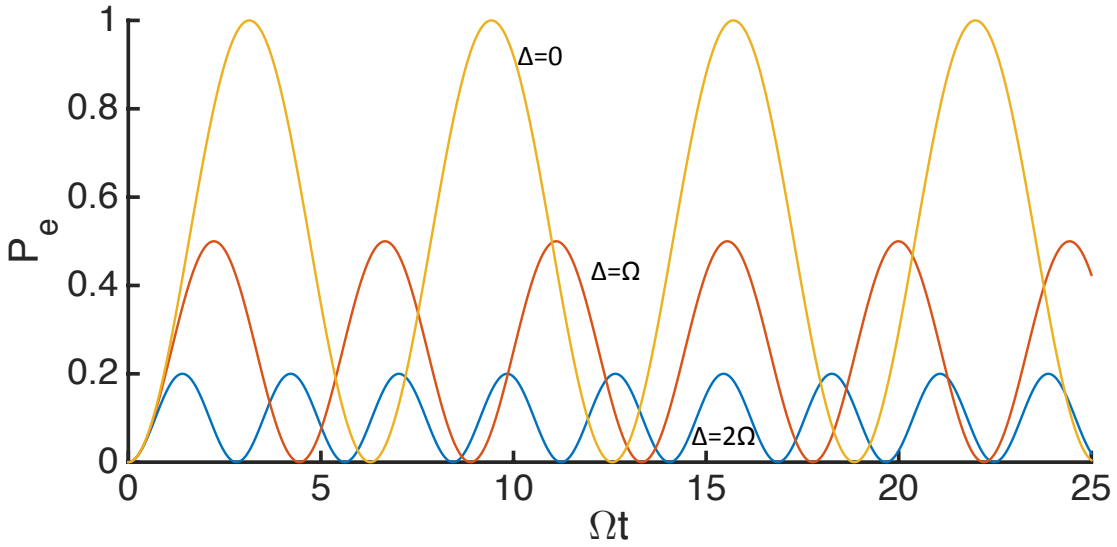

Figure 2.1: (Color online) excitation probability over time for different detunings of $\Delta = 0$ (yellow line), $\Delta = \Omega$ (red line) and $\Delta = 2\Omega$ (blue line). Increasing the detuning reduces the excitation probability and increases the effective Rabi frequency.

2.3 Atom-photon Interaction and Equations of Motion

In this section we derive the propagation dynamics of a single photon and also the created polarization field in the atomic medium. These results are especially important for the following chapter.

2.3.1 Quantized Fields

A non-classical signal field in the Schrödinger picture can be written as a dimensionless operator

$$\hat{\mathbf{E}}(z) = i\boldsymbol{\epsilon} \int g(\omega)\hat{a}(\omega)e^{ikz}d\omega + h.c. \tag{2.15}$$

where

$$g(\omega) = \sqrt{\frac{\hbar\omega}{4\pi\epsilon_0 Ac}} \tag{2.16}$$

is the mode amplitude, with A being the cross section of the signal, c is the speed of light and $\boldsymbol{\epsilon}$ the signal polarization. The photon annihilation operator satisfies the commutation

relation

$$[\hat{a}(\omega), \hat{a}^{\dagger}(\omega')] = \delta(\omega - \omega'). \tag{2.17}$$

The annihilation operator in the Heisenberg picture is

$$\hat{a}(\omega, t) = \hat{a}(\omega) e^{-i\omega t}. \tag{2.18}$$

The quantum properties of the two level atoms can be quantified by the collective polarization operator, which is the average of the atomic polarization in a small volume δV containing $N_z \gg 1$ atoms at position z

$$\hat{\mathbf{P}}(z) = \frac{n(z)}{N_z} \sum_{j=1}^{N_z} (\mathbf{d}_{ge} \hat{\sigma}_{ge}^{j} + h.c) \tag{2.19}$$

where $\mathbf{d_{ge}} = \langle e|\mathbf{r}|g\rangle$ is the dipole moment and $n(z)$ is the local atomic density. The longitudinal size of each segment should be $\delta z \ll \lambda_s$ to make sure that the optical phase is constant over each segment. The flipping operators $\hat{\sigma}_{ge}^{i}, \hat{\sigma}_{eg}^{i}$, satisfy the bosonic commutation relation

$$[\hat{\sigma}_{ge}^{i}, \hat{\sigma}_{eg}^{j}] = \delta_{ij} \tag{2.20}$$

and in the Heisenberg picture can be written as

$$\hat{\sigma}_{eg}^{j}(t) = \hat{\sigma}_{eg}^{j} e^{-i\omega_{eg} t} \tag{2.21}$$

where $\omega_{eg} = \frac{E_{eg}}{\hbar}$ is the energy separation between two atomic states.

2.3.2 Slowly Varying Envelope (SVE) Approximation

Realistic electromagnetic fields are not plane waves; they have finite spatial and temporal extent. In the regime of SVE approximation (see Eq. 2.25), the field ($\hat{\mathbf{E}}(z,t)$) is considered as a carrier plane wave ($e^{i(k_0 z - \omega_0 t)}$) multiplied by an envelope ($\hat{\boldsymbol{\mathcal{E}}}(z,t)$) that its significant change in time and space occurs at a rate much slower than the period and the wavelength respectively. Considering the case where the signal bandwidth is much smaller than its central frequency ω_0, the dependence of $g(\omega)$ (defined in Eq. 2.16) on frequency will be

relatively weak and we approximate it as constant over the range of band-width ($g_s = g(\omega_0)$). As a result electric field can be written as

$$\hat{\mathbf{E}}(z,t) = \hat{\boldsymbol{\mathcal{E}}}(z,t) g_s e^{i(k_0 z - \omega_0 t)} + h.c = e^{i(k_0 z - \omega_0 t)} i\boldsymbol{\epsilon} g_s \int \hat{a}(\omega, t) e^{i\frac{\omega}{c}z} d\omega + h.c., \tag{2.22}$$

where ω_0 and $k_0 = \frac{\omega_0}{c}$ are signal's central frequency and wave-vector. The slowly varying operator $\hat{\mathcal{E}}(z,t)$ satisfies the commutation relation in a spatio-temporal rather than in spectral mode

$$[\hat{\boldsymbol{\mathcal{E}}}(z,t), \hat{\boldsymbol{\mathcal{E}}}^{\dagger}(z',t')] = \delta(t - z/c - (t' - z'/c)). \tag{2.23}$$

The slowly varying operator for the atomic polarization is expressed accordingly as

$$\hat{\mathbf{P}}(z,t) = \hat{\boldsymbol{\mathcal{P}}}(z,t) e^{i(k_0 z - \omega_0 t)}. \tag{2.24}$$

The slowly varying condition for both electromagnetic and polarization envelopes, is given by

$$\begin{pmatrix} \partial_t \\ \partial_z \end{pmatrix} (\hat{\boldsymbol{\mathcal{E}}},\, \hat{\boldsymbol{\mathcal{P}}}) \ll \begin{pmatrix} \omega_0 \\ k_0 \end{pmatrix} (\hat{\boldsymbol{\mathcal{E}}},\, \hat{\boldsymbol{\mathcal{P}}}). \tag{2.25}$$

2.3.3 Maxwell Equations

Maxwell's equations are the signal field's equation of motion in an atomic medium. Atomic medium can be considered as a dielectric medium, which results in the Maxwell equations of

$$\begin{aligned} \nabla.\hat{\mathbf{D}} &= \rho_{free} \\ \nabla.\hat{\mathbf{B}} &= 0 \\ \nabla \times \hat{\mathbf{E}} &= -\partial_t \hat{\mathbf{B}} \\ \nabla \times \hat{\mathbf{H}} &= \mathbf{J_{free}} + \partial_t \hat{\mathbf{D}}, \end{aligned} \tag{2.26}$$

where $\hat{\mathbf{D}}$ is the displacement field, $\hat{\mathbf{H}}$ is the magnetic field, $\hat{\mathbf{E}}$ is the electric field and $\hat{\mathbf{B}}$ is the magnetic induction. Free charge density and currents (ρ_{free} and $\mathbf{J_{free}}$) are both zero in a neutral atom ensemble that we consider in this thesis. Furthermore our considered mediums are non-magnetic; as a result $\hat{\mathbf{B}} = \mu_0 \hat{\mathbf{H}}$ where μ_0 is the permeability of free space.

To find a wave equation for the electric field we start by time derivation of the $\hat{\mathbf{H}}$ equation

$$\nabla \times \partial_t \hat{\mathbf{H}} = \partial_t^2 \hat{\mathbf{D}}. \tag{2.27}$$

where $\partial_t \hat{\mathbf{H}}$ can be substituted by $\frac{1}{\mu_0}\nabla \times \hat{\mathbf{E}}$ from the third Maxwell equation (Eq. 2.27) to find

$$\nabla \times \nabla \times \hat{\mathbf{E}} = \mu_0 \partial_t^2 \hat{\mathbf{D}}. \tag{2.28}$$

Using the vector calculus, the double curl in the left can be replaced by

$$\nabla \times \nabla \times \hat{\mathbf{E}} = \nabla(\nabla.\hat{\mathbf{E}}) - \nabla^2 \hat{\mathbf{E}}. \tag{2.29}$$

The signal is a transverse propagating wave with zero divergence. As a result Equation 2.28 simplifies to

$$\nabla^2 \hat{\mathbf{E}} = \mu_0 \partial_t^2 \hat{\mathbf{D}}. \tag{2.30}$$

Displacement operator is defined as

$$\hat{\mathbf{D}} = \epsilon_0 \hat{\mathbf{E}} + \hat{\mathbf{P}}, \tag{2.31}$$

where $\hat{\mathbf{P}}$ is the polarization density (see Eq. 2.19) and ϵ_0 is the vacuum permittivity. Substituting Eq. 2.31 into Eq. 2.30 results to the wave equation

$$[\nabla^2 - \frac{1}{c^2}\partial_t^2]\hat{\mathbf{E}} = \mu_0 \partial_t^2 \hat{\mathbf{P}} \tag{2.32}$$

where $c = \frac{1}{\sqrt{\epsilon_o \mu_0}}$ is the speed of light. This equation relates the propagation of the signal field with the component of atomic polarization that interacts with the signal field. Since in chapter 4, signal propagates within the optical fiber, we are interested in a one dimensional propagation method and therefore drop the transverse coordinate.

SVE approximation provides a chance to only deal with the propagation of the envelope $\hat{\boldsymbol{\mathcal{E}}}(z,t)$ defined in Eq. 2.22, without the fast oscillating carrier wave, which simplifies the equation of motion. Substituting Eq. 2.22 and Eq. 2.24 into Eq. 2.32 results to

$$[\nabla^2 - \frac{1}{c^2}\partial_t^2][\hat{\boldsymbol{\mathcal{E}}} g_s e^{i(k_0 z - \omega_0 t)}] = \mu_0 \partial_t^2 [\hat{\boldsymbol{\mathcal{P}}} e^{i(k_0 z - \omega_0 t)}]. \tag{2.33}$$

Applying the derivation on the oscillating carrier wave part and dividing out both sides by $[e^{i(k_0 z-\omega_0 t)}]$ followed by a scalar product of $\boldsymbol{\epsilon}^*$ results to

$$[(\partial_z^2-\frac{1}{c^2}\partial_t^2)+2i\frac{\omega_0}{c}(\partial_z+\frac{1}{c}\partial_t)-(\frac{\omega_0^2}{c^2}-\frac{\omega_0^2}{c^2})]\hat{\mathcal{E}}=-\frac{\mu_0}{g_s}\boldsymbol{\epsilon}^*.(\partial_t^2-2i\omega_0\partial_t-\omega_0^2)\hat{\boldsymbol{\mathcal{P}}}. \tag{2.34}$$

Considering the SVE condition explained in Eq. 2.25, we drop the small terms to find

$$(\partial_z+\frac{1}{c}\partial_t)\hat{\mathcal{E}}=\frac{\mu_0\omega_0^2}{2g_s k_0}\boldsymbol{\epsilon}^*.\hat{\boldsymbol{\mathcal{P}}}. \tag{2.35}$$

Considering equations 2.19 and 2.24 and defining a set of collective operators

$$\begin{aligned}\hat{\sigma}_{gg}&=\frac{1}{N_z}\sum_{j=1}^{N_z}\hat{\sigma}_{gg}^j \\ \hat{\sigma}_{ee}&=\frac{1}{N_z}\sum_{j=1}^{N_z}\hat{\sigma}_{ee}^j \\ \hat{\sigma}_{ge}&=\frac{1}{N_z}\sum_{j=1}^{N_z}\hat{\sigma}_{ge}^j e^{i(\omega_0 t-k_0 z)}\end{aligned} \tag{2.36}$$

the equation of motion looks like

$$(\partial_z+\frac{1}{c}\partial_t)\hat{\mathcal{E}}=igN\hat{\sigma}_{ge}, \tag{2.37}$$

where

$$g=\frac{\boldsymbol{\epsilon}^*.\mathbf{d_{eg}}}{\hbar}g_s, \tag{2.38}$$

is the atom-photon coupling constant.

2.3.4 Bloch Equations

The Hamiltonian of two level atoms that are interacting with a single photon (see Eq. 2.15) within the dipole approximation and rotating wave approximation is given by

$$\hat{H}=\int\hbar\omega\hat{a}^\dagger(\omega)\hat{a}(\omega)d\omega+\frac{1}{N_z}\sum_{j=1}^{N_z}\hbar\omega_e\hat{\sigma}_{ee}^j-\frac{\hbar g}{N_z}\sum_{j=1}^{N_z}\int(\hat{a}(\omega)e^{ikz_j}\hat{\sigma}_{eg}^j+h.c.)d\omega \tag{2.39}$$

where ω_e is the resonant frequency of state $|e\rangle$ and g is the atom photon coupling constant defined in equation 2.38. The atomic projection-transition operators are defined by $\hat{\sigma}_{ij}=$

$|i\rangle\langle j|$. Since we are aiming for the storage of weak fields with a few photons, most of the atoms remain in the ground state. As a result we can use the expectation values of the population operators $\langle\hat{\sigma}_{gg}\rangle = 1$, $\langle\hat{\sigma}_{ee}\rangle = 0$ and ignore their dynamics. The dynamics of the atomic transition operators can be obtained from the Heisenberg equation

$$\begin{aligned}\partial_t\hat{\sigma}_{ge} &= \frac{i}{\hbar}[\hat{H},\hat{\sigma}_{ge}] + \frac{\partial}{\partial_t}\hat{\sigma}_{ge} + \hat{F}_{ge} \\ &= \frac{i\omega_e}{N_z}\sum_{i,j=1}^{N_z}[\hat{\sigma}^i_{ee},\hat{\sigma}^j_{ge}]e^{i(\omega_0 t - k_0 z)} - \frac{ig}{N_z}\sum_{i,j=1}^{N_z} e^{i(\omega_0 t - k_0 z)}[\hat{\sigma}^i_{eg},\hat{\sigma}^j_{ge}]\int \hat{a}(\omega)e^{ikz_i}d\omega + i\omega_0\hat{\sigma}_{ge} + \hat{F}_{ge},\end{aligned} \tag{2.40}$$

where $\hat{F}_{ge}$ is the Langevin noise. By substituting the collective operators of Eq. 2.36 and slowly varying photonic operator introduced in Eq. 2.22 we find

$$\frac{\partial}{\partial_t}\hat{\sigma}_{ge} = -i\Delta\hat{\sigma}_{ge} - ig(\hat{\sigma}_{ee} - \hat{\sigma}_{gg})\hat{\mathcal{E}} + \hat{F}_{ge}, \tag{2.41}$$

where $\Delta = \omega_e - \omega_0$ is the detuning. Since the time scales of interest in the following chapter are far shorter than the decoherence time, we ignore the Langevin term.

In chapter 4 we replace photonic and atomic coherence field operators with their corresponding wave functions $\mathcal{E} = \langle 0|\hat{\mathcal{E}}|\psi_i\rangle$ and $\sigma_{ge} = \langle 0|\hat{\sigma}_{ge}|\psi_i\rangle$ where $|\psi\rangle$ is the single excitation in the atom-photon Hilbert space. Due to the linearity the wave-function dynamics of a single excitation would be the same with the field operator dynamics, and can be represented as

$$\begin{aligned}(\partial_z + \frac{1}{c}\partial_t)\mathcal{E} &= igN\sigma_{ge} \\ \frac{\partial}{\partial_t}\sigma_{ge} &= -i\Delta\sigma_{ge} - ig\mathcal{E}.\end{aligned} \tag{2.42}$$

2.4 Conclusion

In this section we discussed the evolution dynamics of atoms interacting with laser field. We also discussed the propagation dynamics of a single photon field and its corresponding polarization field in the atomic medium. These results will be used widely in the following chapters.

Chapter 3

Quantum Communication and Quantum Memories

3.1 Preface

This chapter provides a brief introduction to quantum communication and the importance of quantum memories in the realization of quantum networks. It also introduces two well-known quantum memory protocols based on photon echo and slow light. In chapter 4 we propose a quantum memory that can be considered as a bridge between these two well-known protocols.

3.2 Quantum Network

Creating global quantum network (i.e. quantum Internet) is an appealing goal [66]. It is desired for the quantum key distribution (QKD), where the quantum protocols (e.g. BB84) lead to inherently safe transfer of information. Even small transition rate allows frequent key changes that can be deployed in classical cryptography. The quantum Internet would connect quantum computers through quantum teleportation, resulting in a more powerful cluster similar to the idea of classical Internet. Other proposals for the application of quantum networks include private database queries based on a quantum-key-distribution [67], proposals for blind quantum computing [68], quantum clock networks [69] and protocols for improving telescopes [70].

3.3 Encoding the Information (Qubit)

Quantum Information can be encoded into a two mutually exclusive states of a quantum system, which is called a qubit [71]. A pure qubit state is a linear superposition of the basis

states or in the other word it is a linear combination of $|0\rangle$ and $|1\rangle$: $|\psi\rangle = \alpha|0\rangle + \beta|1\rangle$, where α and β are probability amplitudes fulfilling the equation $|\alpha|^2 + |\beta|^2 = 1$. Because of the superposition characteristic of quantum states, a qubit carries much more information comparing to classical bit. While a classical system can be explained with n bits a complete description of a quantum system requires $2^n - 1$ complex numbers. In photonic systems information can be encoded into many degrees of freedom namely polarization, number of photons in the Fock state, spatial and temporal separations that leads to dual rail qubits and time bins respectively.

3.4 No Cloning Theorem

Unlike the classical bits, qubits can not be copied, which is known as the no-cloning theorem [72]. Therefore to store the quantum information one needs to transfer the actual quantum state to the quantum memory in a way that the stationary qubit acquires all the information, and nothing left in the flying qubit. This means that we cannot have back up similar to classical computers. No cloning also deprives quantum communication from the classical repeater station in long distance communications as well as classical error correction, where the quantum version of each has been pursued [71, 73, 74].

3.5 Quantum Repeater

Direct quantum communication over 144km has been realized with free propagating photons in Vienna [75], and also direct QKD has been reported over 300km in optical fibers in Geneva [76]. Very recently a measurement device independent QKD has been reported over 404km in an ultralow-loss optical fiber [77]. However direct transmission over long distances suffers from loss and decoherence. A successful direct transmission of a photon over 1000km would take 300 years in a fiber with 0.2dB/km loss rate and with the source repetition of 10GHz. Considering the no-cloning theorem one possible solution is quantum repeater.

Quantum repeaters [73, 74] are based on the idea of splitting a long distance into small segments, where each segment contains stored entangled photons across it that are generated independently. Following entanglement swapping between adjacent nodes will lead to the entanglement distribution over the far distances. Created entanglement can be used for quantum key distribution using Ekert protocol [78] and also quantum teleportation [79, 80].

Considering the current non-deterministic nature of entanglement swapping gates and entangled photon sources, successful entangled photons should be stored in quantum memories until the successful process in the neighboring segments are made. Application of quantum memory can improve the operation time of quantum repeaters from an exponential scale with respect to the number of segments to a polynomial one [81]. Therefore quantum memory has a crucial role in the generation of scalable network.

3.6 Quantum Memories for Light

A quantum memory is a system that can store and retrieve quantum states on demand. Considering a photonic quantum memory, non-classical states of light could include single photons, qubit states, entanglement, and in the continuous variable case, squeezing. Implementation of quantum memory is essential in photonic quantum information tasks such as creating deterministic single photon sources, synchronizing the steps in quantum computation and implementation of quantum repeaters for long range quantum communication [82, 83, 84].

The physical system of quantum memory could be atoms, ions or defects in solids. As explained before the focus of this thesis is on the atomic ensemble. A photonic quantum memory converts flying qubit (an incident photon) into a stationary qubit (an atomic excitation) that are in resonance, via an electric dipole transition. However the continuing presence of dipole interaction results in the re-emission of photons by the atom. This absorption and re-emission happens continuously and is known as Rabi flopping [85]. The Rabi frequency

of this cycle Ω depends on the strength of this coupling. This coupling alone does not result in the storage of photonic state.

There are two types of schemes to control atom-photon interaction for on demand storage and retrieval of photons. In one type a long lived spin state $|s\rangle$ is used, which is uncoupled from the signal mode, to freeze the Rabi oscillation. A control field that couples $|e\rangle$ and $|s\rangle$ states manipulates the atom-signal's interaction. The two famous examples of these memories are electromagnetically induced transparency (EIT) [86] and Raman [87, 88, 89], where the former one will be explained in Sec. 3.6.1. Other schemes use the phenomenon of photon echo to control the atom-photon interaction. In this method the signal is stored in an inhomogeneously broadened medium where the atom-photon interaction is controlled by dephasing-rephasing process. Controlled reversible inhomogeneous broadening (CRIB) [90] and atomic frequency comb (AFC) [91] quantum memories are examples of this type where the former one is explained in Sec. 3.6.2.

3.6.1 EIT

In the electromagnetically induced transparency scheme, shining a strong control field makes an opaque medium transparent to the weak signal field. Looking at the lambda scheme level in Fig. 3.1a, one can see that in the absence of control field signal will be absorbed in the excited state $|e\rangle$. However the presence of control field creates a coupling between $|e\rangle$ and $|s\rangle$ states with the coupling terms of $(\Omega|e\rangle\langle s| + h.c.)$. Diagonalizing the Hamiltonian results in $H = \Omega(|+\rangle\langle+| - |-\rangle\langle-|)$ where the atomic dressed states are $|\pm\rangle = (|e\rangle \pm |s\rangle)/\sqrt{2}$ [92, 93]. As can be seen in fig. 3.1b non of the dressed states are in resonance with the signal. The new resonance peaks are known as Autler-Townes doublet [94]. Susceptibility of probe field is shown in fig. 3.1c as a function of detuning from $|e\rangle - |s\rangle$ resonance. The absorption associated with the imaginary part of susceptibility completely vanishes due to destructive interference of two contributing dressed states.

In addition to transparency, group velocity of the signal reduces significantly due to the

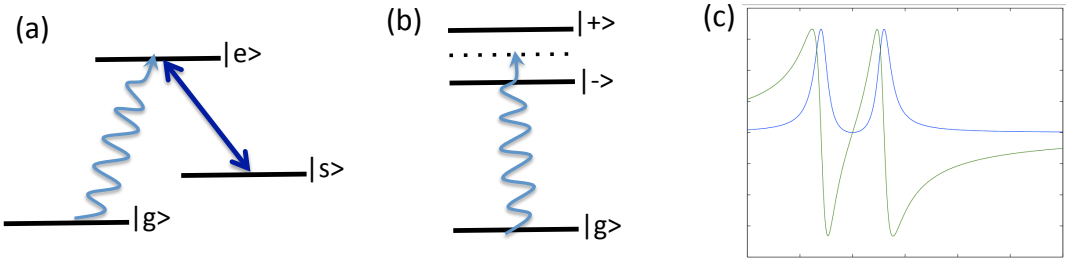

Figure 3.1: (Color online) Electromagnetically Induced Transparency (EIT). a) While the weak signal is propagating within the medium, control field couples the excited and metastable spin states. b) Coupling of excited and spin states results in an effective Autler-Townes splitting. None of these dressed states are in resonance with the signal. c) Imaginary (blue line) and real (green line) parts of the susceptibility as a function of signal's detuning. Imaginary part depicts a transparency window at the atomic transition resonance. The real part has a steep slope at this resonance causing slow propagation of the field.

strong dispersion within the transparency window. The trajectory of a multi-mode pulse is given by the condition of preserving all the components of a photon with bandwidth $\delta\omega$ in phase $\delta\omega\delta t = \delta k\delta z$ where the wave vector is $k = \frac{n\omega}{c}$. As a result the group velocity of the pulse would be $v_g = \frac{dz}{dt} = \frac{d\omega}{dk} = \frac{c}{n+\omega dn/d\omega}$. The steep variation of $Re(\chi)$ at the center of transparency window lead to a large $n' = dn/d\omega$ which results in the slow light.

To apply EIT for quantum storage of photons [95, 96, 97, 98, 99, 100], one can attenuate the control field when the pulse is compressed and accommodated into the medium. This attenuation reduces the Autler-Townes doublet splitting (transparency window) and makes the $Re(\chi)$ steeper which results to slower velocity. This process continue until the two peaks collapse and the group velocity approaches to zero and photon is absorbed in atomic excitation. The reverse process results in the retrieval of photon.

The dark state polariton (DSP) model shows that under the adiabatic process photon does not couple to the radiative excited state $|e\rangle$ [95]. DSP ($|\psi\rangle = \cos(\theta)\hat{E}(z,t) + \sin(\theta)\hat{\sigma}_{gs}(z,t)$) is a quasi-particle with superposition of both photonic ($\hat{E}$) and atomic excitation ($\hat{\sigma}_{gs}$) natures.

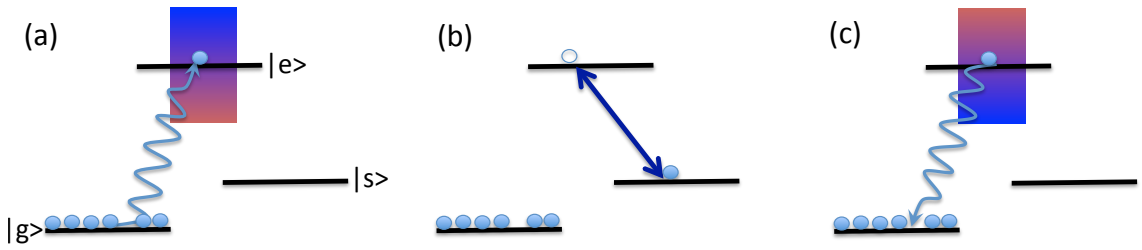

Figure 3.2: (Color online) Level scheme of Controlled Reversible Inhomogeneous Broadening. a) A gradient of external field over the ensemble makes the transition in resonance with a broadband signal. b) After the storage, the external field should be turned of followed by shelving the excitation in a metastable spin state $|s\rangle$ applying a control field. For the retrieval, shining the control field brings back the excitation to the excited state $|e\rangle$. c) Applying a reversed spatial gradient field results to the rephasing and retrieval of signal.

The ratio of this superposition is determined by the strength of control field $\tan(\theta) = \frac{g\sqrt{N}}{\Omega}$, where the nominator and denominator are representing the signal and control coupling strength to the atomic transitions. The dynamic of the DSP can be obtained from the Maxwell-Bloch equations as

$$(\frac{\partial}{\partial t} + c\cos^2\theta(t)\frac{\partial}{\partial z})\psi(z,t) = 0, \tag{3.1}$$

where the group velocity of DSP approaches zero and speed of light in the two extreme limits of being all in atomic mode ($\Omega = 0$) and photonic mode ($\Omega \gg g\sqrt{N}$) respectively.

3.6.2 CRIB

In controlled reversible inhomogeneous broadening (CRIB) scheme, spatial gradient of external electric or magnetic field, shifts the ground-excited states transition frequency (ω_{eg}) based on the position of the atoms. Therefore while each atom has a narrow frequency bandwidth, the entire ensemble can be in resonance over a broad frequency range, thanks to the spatially inhomogeneous broadening.

After the absorption of single photon the ensemble acquires a delocalized collective exci-

tation

$$|\psi\rangle = \sum_{j=1}^{N} e^{i(kz_j+\delta_j t)}|g_1...e_j...g_N\rangle. \tag{3.2}$$

where j labels the excited atom in the ensemble and δ_j is the detuning of jth atom from signal's central frequency. Depending on the position of excited atom in the spatially inhomogeneous broadened medium, they experience different phase evolution rates which, makes them out of phase over time. The distortion of spatial phase pattern prevents re-emission of photons and results to the storage of signal. Signal retrieval requires the rephasing of the collective excitation by reversing the dephasing process. That can be done through inverting the spatial gradient of external field, in a way that previously blue shifted atoms become correspondingly red shifted. As a result collective excitation eventually becomes in phase and re-emit photon.

For long time storage, the excitation must be shelved in a metastable state $|s\rangle$. This will be done through the following steps as illustrated in Fig. 3.2: after the storage the external field is turned off followed by the application of control field which transfers the population from $|e\rangle$ to $|s\rangle$ states. For the retrieval shining the control field brings back the excitation to the $|e\rangle$ level and the following reversed spatial gradient field results to the rephasing and retrieval of signal. This memory can only be used for temporal pulses shorter than excited states lifetime, otherwise the pulse will be lost before its shelving in the long lived spin state.

Based on the relative direction of spatial gradient field and incoming signal, there are two types of longitudinal and transversal CRIB memories. The former one is also called gradient echo memory (GEM) [101] where broadening is along the photon direction of propagation. The other difference of the two types are in the direction of photon retrievals where in transversal CRIB efficient retrieval can be performed in the backward direction, which requires the application of an additional control field while in GEM retrieval could be in the forward direction which would get in phase over time without the application of external control field.

3.7 Conclusion

In this section we introduced the concept of quantum networks and explained the role of quantum memories in improving the quantum communication rates over the long distances. We also talked about two quantum memory approaches in the atomic ensemble and explained an example of each type in detail.

Chapter 4

Quantum Storage and Retrieval of Light by Sweeping the Atomic Frequency

4.1 Preface

This chapter proposes a quantum memory protocol based on dynamically changing the resonance frequency of an ensemble of two-level atoms. By sweeping the atomic frequency in an adiabatic fashion, photons are reversibly transferred into atomic coherences. We present a polaritonic description for this type of storage, which shares some similarities with electromagnetically induced transparency based quantum memories. On the other hand the proposed memory is also linked to the gradient echo memory due to the effective spatial gradient that pulses experience in the medium. We discuss a possible implementation of the protocol in hollow-core photonic crystal fibers.

This work was mainly done in collaboration with a master student, Hamidreza Kaviani. I contributed to this project by performing analytical calculations namely formulating the polaritonic model, exploring the effects of decohernce, dispersion and adiabaticity on the polariton dynamics. I also helped in modifying the numerical program to match the numerical and analytical results.

4.2 Introduction

Storage and retrieval of photons on demand is essential for quantum information processing tasks such as long-distance quantum communication and distributed quantum computing [102, 103, 104]. Quantum memories for photons can be realized by coherent control of the atom-photon interaction. Some protocols for quantum memory introduce a control

beam in a three-level atomic configuration to manipulate the interaction between the signal pulse and the atoms (e.g. Electrically Induced Transparency (EIT) [86] and Raman schemes [87, 88, 89]). Other protocols use the phenomenon of photon echo [105, 106] to achieve controlled atom-photon interaction. In this type of memory the atom-photon interaction is controlled in a more indirect way by a dephasing-rephasing process owing to the inhomogeneous broadening of the medium. Atomic Frequency Comb memory (AFC) [91], Controlled Reversible Inhomogeneous Broadening memory (CRIB) [90] and Gradient Echo Memory (GEM) [101] are examples of this type of protocols. In contrast to EIT and Raman protocols, which require at least three atomic levels, photon echo based protocols can be implemented using just two atomic levels, relying on long excited state lifetimes for storage. Such long lifetimes for optical transitions are common for example in rare-earth ion doped crystals.

Recently it has been shown that some of these protocols can be emulated by dynamically changing certain characteristics of an ensemble of two-level atoms. For instance, it has been shown that by dynamically controlling the transition dipole moment of an ensemble of two-level atoms, one can emulate Raman-type quantum memories [107]. More recently it has been shown that changing the refractive index of the host medium of two-level atoms is equivalent to the GEM memory [108].

Here we study another way of manipulating the atom-photon interaction, namely by sweeping the atomic frequency of a homogeneously broadened ensemble of two-level atoms in time. The energy levels of the two-level atoms can be changed by applying a magnetic or electric field depending on the system.

We demonstrate that the proposed "Atomic Frequency Sweep (AFS)" protocol can be described in terms of polaritons, which share some similarities with the dark-state polariton in EIT [109]. By changing the detuning, the pulse slows down and is stored in atomic coherences. Changing the detuning in AFS plays the role of changing the control field in

EIT. However there are also differences between AFS and EIT based protocols, in particular, in our protocol the pulse does not shrink when it enters the medium, in contrast with EIT. Moreover here the polaritons are associated with the optical transition.

On the other hand, the AFS protocol is similar to the GEM protocol for the regime in which pulses are short compared to the medium length. While we change the detuning in time during the propagation of the pulse through the medium, the pulse effectively sees a spatial gradient in the energy levels of the atoms, and the excited atomic coherences become dephased.

Due to its similarities with both EIT and GEM, the AFS protocol thus constitutes a bridge between protocols based on coherent control and those based on photon echo.

This chapter is organized as follows. In section 4.3 we describe the scheme using a polaritonic description. In section 4.4 we discuss the experimental requirements and a possible implementation. In section 4.5 we give our conclusions.

4.3 AFS Quantum Memory: Polaritonic Description

The Maxwell-Bloch equations for the field and atomic polarization (or, equivalently, the single-excitation photonic and atomic wavefunctions) under the dipole, rotating-wave and slowly varying envelope approximations are derived in equations 2.42 as [103, 88, 107]

$$\frac{\partial}{\partial t}\sigma_{ge}(z,t) = -i(\Delta(t) - i\gamma)\sigma_{ge} + i\beta\mathcal{E}(z,t), \tag{4.1}$$

$$(c\frac{\partial}{\partial z} + \frac{\partial}{\partial t})\mathcal{E}(z,t) = i\beta\sigma_{ge}, \tag{4.2}$$

where $\Delta(t)$ is the detuning, γ is decay rate and $\beta = g\sqrt{N}$ is the collective coupling constant, with g the single-atom coupling and N the number of atoms.

Our proposed scheme is best described in a polaritonic picture. We can write Eq. (4.1)

and Eq. (4.2) in k-space as

$$\frac{\partial}{\partial t}\begin{pmatrix}\mathcal{E}(k,t)\\ \sigma_{ge}(k,t)\end{pmatrix} = i\begin{pmatrix}-kc & \beta\\ \beta & -\Delta(t)\end{pmatrix}\begin{pmatrix}\mathcal{E}(k,t)\\ \sigma_{ge}(k,t)\end{pmatrix}. \tag{4.3}$$

For the sake of simplicity, we neglect the decay rate γ for now. We will discuss its effects at the end of this section.

One can solve this set of equations by looking at its eigenmodes:

$$\Psi(k,t) = \cos\theta(k)\mathcal{E}(k,t) + \sin\theta(k)\sigma_{ge}(k,t), \tag{4.4}$$

$$\Phi(k,t) = -\sin\theta(k)\mathcal{E}(k,t) + \cos\theta(k)\sigma_{ge}(k,t), \tag{4.5}$$

where the mixing angle $\theta(k)$ is given by

$$\sin 2\theta(k,t) = \frac{2\beta}{\sqrt{4\beta^2 + (ck+\Delta(t))^2}}, \tag{4.6}$$

$$\cos 2\theta(k,t) = \frac{-(ck+\Delta(t))}{\sqrt{4\beta^2 + (ck+\Delta(t))^2}}. \tag{4.7}$$

In terms of these eigenmodes, the equations of motion become

$$\frac{\partial}{\partial t}\begin{pmatrix}\Psi(k,t)\\ \Phi(k,t)\end{pmatrix} = i\begin{pmatrix}\lambda_1(k,t) & \dot\theta(k,t)\\ \dot\theta(k,t) & \lambda_2(k,t)\end{pmatrix}\begin{pmatrix}\Psi(k,t)\\ \Phi(k,t)\end{pmatrix}, \tag{4.8}$$

where $\lambda_1 = \beta\cot\theta$ and $\lambda_2 = -\beta\tan\theta$ are the eigenvalues of the system and $\dot\theta = -\frac{\dot\Delta}{4\beta}\sin^2 2\theta$ is the time derivative of the mixing angle. One can expand the matrix in equation (4.8) in the basis of Pauli matrices and the identity matrix

$$\begin{pmatrix}\lambda_1(k,t) & \dot\theta(k,t)\\ \dot\theta(k,t) & \lambda_2(k,t)\end{pmatrix} = (\frac{\lambda_1(k,t)+\lambda_2(k,t)}{2})\mathbb{1} + (\frac{\lambda_1(k,t)-\lambda_2(k,t)}{2})\sigma_z + \dot\theta(k,t)\sigma_x. \tag{4.9}$$

Assuming the adiabatic condition $\dot{\theta}(k,t) \ll \frac{\lambda_1(k,t)-\lambda_2(k,t)}{2}$ holds during the storage and retrieval process, we can neglect σ_x term compared to σ_z term in Eq. (4.9) so that the eigenmodes become decoupled.

Now we Taylor-expand the eigenvalues in terms of k. In the regime where the coupling constant is larger than the bandwidth of the input pulse ($\beta \gg \Delta\omega$), we can keep terms up to first order in k and neglect higher orders of k. With that, and transforming the equations back to z space, we find the equations of motion for the eigenmodes Ψ and Φ in real space:

$$\frac{\partial\Psi(z,t)}{\partial t} + c\cos^2\theta(t)|_{k=0}\frac{\partial\Psi(z,t)}{\partial z} = i\lambda_1(t)|_{k=0}\Psi(z,t), \tag{4.10}$$

$$\frac{\partial\Phi(z,t)}{\partial t} + c\sin^2\theta(t)|_{k=0}\frac{\partial\Phi(z,t)}{\partial z} = i\lambda_2(t)|_{k=0}\Phi(z,t). \tag{4.11}$$

From now on, for simplicity we denote $\theta(t)|_{k=0}$ and $\lambda_{1,2}(t)|_{k=0}$, which are the mixing angle and eigenenergies for the central wave vector, by $\theta(t)$ and $\lambda_{1,2}(t)$. Equations (4.10) and (4.11) indicate that the polaritons Ψ and Φ travel with group velocity $v_g = c\cos^2\theta(t)$ and $v_g = c\sin^2\theta(t)$, respectively. Figure 4.1 shows how the mixing angle θ varies with the detuning Δ.

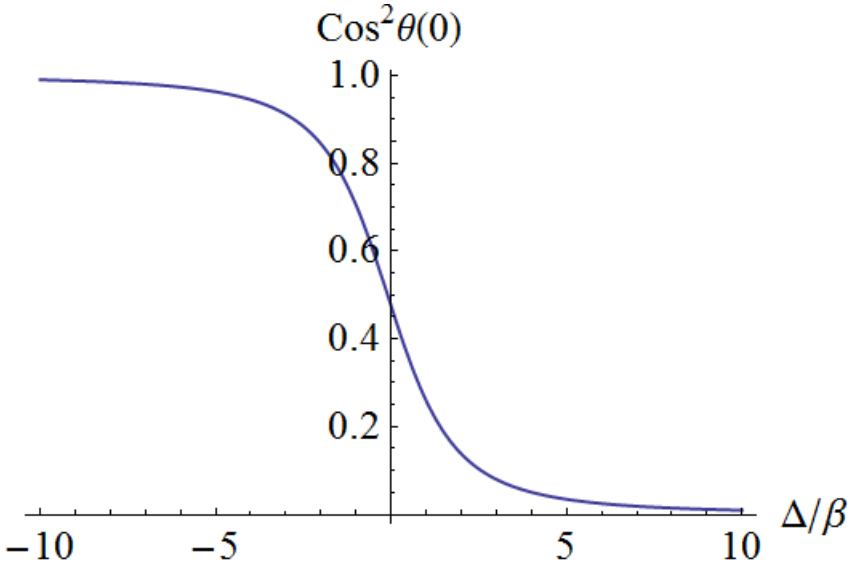

Figure 4.1: Mixing angle $\theta(0)$ as a function of detuning.

Therefore if we start from a large negative (positive) detuning $-\Delta_0$ $(+\Delta_0)$ compared to the coupling, we can couple the input pulse to the polariton Ψ (Φ). By sweeping the detuning adiabatically to a large positive (negative) $+\Delta_0$ $(-\Delta_0)$, we can slow down the light and convert it to the atomic coherence reversibly. The detuning thus plays a role that is analogous to that of the Rabi frequency of the coupling field in the case of EIT.

We have performed numerical simulations that are in excellent agreement with the described polaritonic picture. Figure 4.2 is a simulation of the original Maxwell-Bloch equations Eq. (4.1), Eq. (4.2). It can be seen that by sweeping the atomic frequency across the resonance, light is slowed down and converted to atomic coherence.

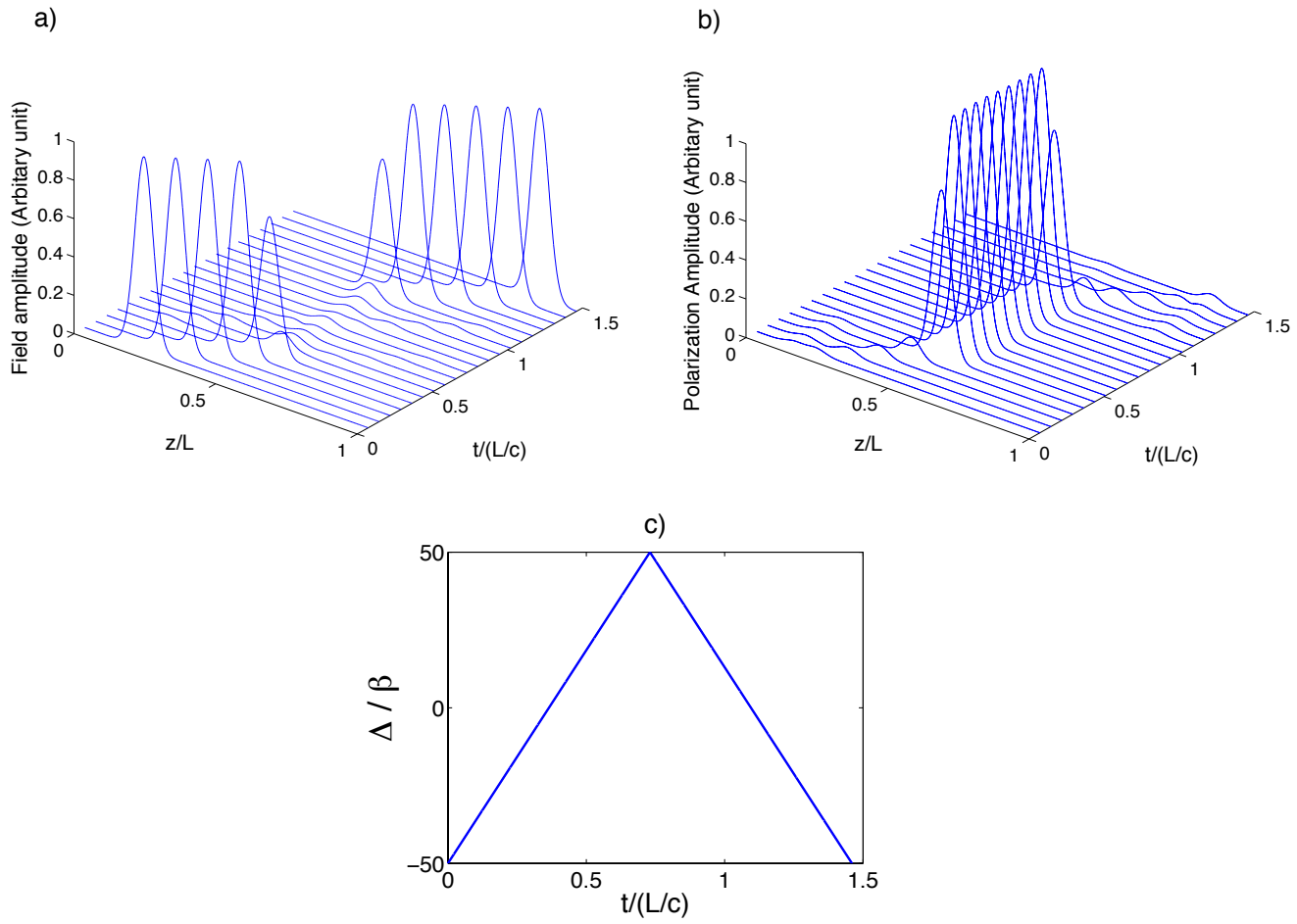

Figure 4.2: Propagation of field (a) and polarization (b) in the medium in time and space. (c) Detuning as a function of time, We start from $\Delta_0 = -50\beta$ and sweep to $+\Delta_0 = 50\beta$ with the rate of $\dot{\Delta} = 0.4\beta^2$. The coupling constant is set to $\beta = 30\Delta\omega$. The initial pulse envelope is $\exp[-(z/z_0)^2]$ where z_0 is $0.045L$. The light is converted into a stationary atomic excitation by sweeping the detuning across the resonance. It is then retrieved by sweeping in reverse direction.

In addition we have compared the group velocity obtained from numerical calculations with the group velocity found in the polaritonic picture. Figure 4.3 shows the excellent agreement between the numerical and analytical group velocities.

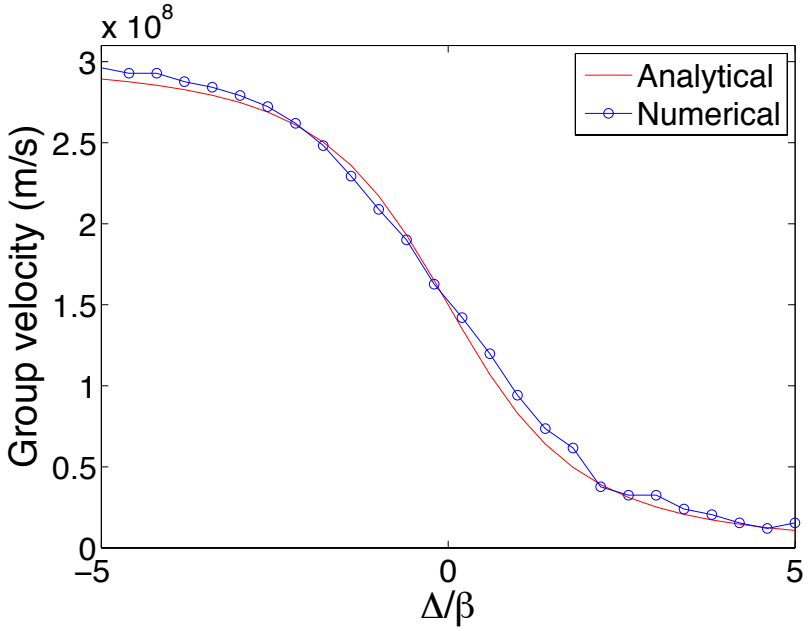

Figure 4.3: Comparison between group velocities resulting from analytical (red) and numerical (blue) calculations. The analytical curve is based on the polaritonic description discussed in the text, while the numerical curve is based on the exact Maxwell-Bloch equations.

Thus far, we have imposed three conditions for obtaining the polaritonic picture. They are summarized below:

$$\beta \ll \Delta_0, \tag{4.12}$$

$$\dot{\theta} \ll \frac{\lambda_1(k) - \lambda_2(k)}{2}, \tag{4.13}$$

$$\Delta\omega \ll \beta. \tag{4.14}$$

We have investigated the physical significance of these conditions numerically. Figure 4.5 shows that if we start with an initial detuning that is not sufficiently larger than the coupling, violating condition (4.12), the light couples to both Ψ and Φ modes, which results in increased loss.

We also examine the adiabatic condition (4.13) in Figure 4.6. If the adiabatic condition is violated at some time during the storage (retrieval) process, the mode of interest leaks to the other eigenmode, which accelerates to the speed of light (decelerates to the speed of zero), again resulting in loss.

Lastly we examine condition (4.14), which allowed the expansion of the eigenenergies in k space, in Figure 4.7. Violating this condition results in dispersion of the pulse in the medium and thus decreases the fidelity of the storage.

It is worth mentioning that the condition 4.12 imposes a lower limit on the rate at which we sweep the atomic frequency. For the case of a linear change of the atomic frequency in time, the sweeping rate is given by $\dot{\Delta} = \frac{2\Delta_0}{T_{sw}}$, where T_{sw} is the duration of sweeping. This expression for the sweeping rate along with condition 4.12 gives us a lower bound on the sweeping rate, $\frac{2\beta}{T_{sw}} \ll \dot{\Delta}$. On the other hand there is an upper bound for the sweeping rate imposed by condition 4.13. If we combine the upper and lower bound we get an interval for the sweeping rate that allows us to store the light efficiently,

$$\frac{2\beta}{T_{sw}} \ll \dot{\Delta} \ll \frac{8\beta^2}{\sin^3(2\theta)}. \tag{4.15}$$

The sweeping time should be of the order of the traveling time of the pulse inside the medium ($1/T_{sw} \approx c/L$). On the other hand, as we discuss in the next section, in the present protocol the pulse has to fit inside the medium ($c/L < \Delta\omega$). This fact along with the condition 4.14 guarantees that the sweeping rate interval 4.15 is not void and there is always a way to change the detuning without violating the conditions 4.12-4.14.

So far we have neglected the decay rate γ in our discussion. In the regime where the coupling constant is much larger than the decay rate ($\beta \gg \gamma$), the decay results in decay rates

$\gamma \sin^2\theta(t)$ and $\gamma \cos^2\theta(t)$ for the polaritons Ψ and Φ, without changing the group velocity. The dependence of the decay on the mixing angle $\theta(t)$ is due to the fact that the decay is associated with the atomic (polarization) part of the polaritons.

4.4 Experimental Requirements

In order to store the light efficiently, the pulse has to fit inside the medium, otherwise those frequency components of the pulse that were not in the medium at the time in which the atoms had the corresponding frequency, do not become absorbed in the medium. This imposes a condition on the frequency bandwidth of the input pulses ($\Delta\omega \gg \frac{c}{L}$). This condition along with the requirement for avoiding dispersion of the pulse in the medium ($\beta \gg \Delta\omega$), and the requirement that the coupling rate is significantly greater than the decay rate ($\beta \gg \gamma$), implies a demanding requirement for the optical depth,

$$d = \frac{\beta^2 L}{c\gamma} \gg \frac{\beta}{\gamma} \gg 1. \tag{4.16}$$

It is worth mentioning that the same condition on the optical depth can be obtained by using the adiabaticity condition ($\dot{\theta} \ll \lambda$) and the initial detuning requirement ($\Delta_0 \gg \beta$).

We numerically calculated the efficiency of the AFS protocol as a function of optical depth (for zero storage time). The results are shown in figure 4.4. This graph shows that high efficiency demands relatively large optical depth. Intuitively the high optical depth requirement can be understood from the fact that the conditions (4.12-4.14) impose a large memory bandwidth (swept frequency range) compared to the pulse spectral bandwidth. Large optical depth is necessary to compensate for the fact that the atoms are spread out over this large frequency range. However, there is room for lowering the precise optical depth requirements by optimizing the sweeping of the atomic frequency in time (see section 4.8). The saturation value of the efficiency in figure 4.4 depends on the decay rate as well as the initial detuning. The decay rate limits the efficiency by the factor of $e^{-4\gamma \int_0^t \sin^2\theta_{k=0}(\tau)d\tau}$. The

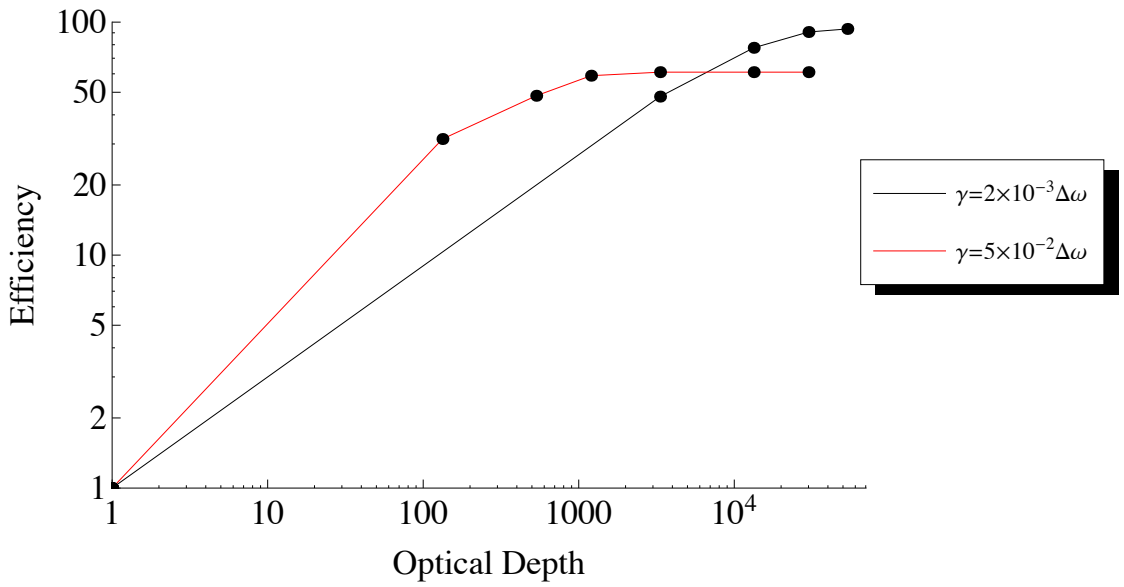

Figure 4.4: Efficiency as a function of optical depth for decay rate of $\gamma = 5 \times 10^{-2}\Delta\omega$ (red) and $\gamma = 2 \times 10^{-3}\Delta\omega$ (black). Here we start from initial detuning $\Delta_0 = -8\beta$ and sweep linearly to $+\Delta_0 = 8\beta$ in a time of $2L/3c$ (For the retrieval process we do the reverse). We fixed the length to 20 cm in accordance with Ref. [110] and changed the optical depth by changing the coupling constant. The initial envelope is $\exp[-(z/z_0)^2]$, where z_0 is $0.15L$.

initial detuning, as we mentioned earlier, determines the portion of the input light that is coupled to the polariton mode of interest (see figure 4.5).

One promising candidate system for implementation of the AFS protocol are atoms in a hollow-core photonic crystal fiber (HCPCF) [110, 111, 112]. On the one hand, this system is suitable for accommodating the entire input pulse, as the length of the HCPCF can be extended to adequate amounts. On the other hand, hot atoms in HCPCF feature large optical depths. In [110], an effective optical depth of 300 has been demonstrated for the inhomogeneously broadened optical line. For a similar length and optical depth as in [110], an efficiency of $\approx 40\%$ for linear sweeping and 57% for nonlinear sweeping is achievable (see section 4.7) with a fidelity of 99%. A longer HCPCF may provide higher optical depths. Storage based on the optical coherence limits the storage time to the optical coherence time. This can be resolved by transferring the excitation to a ground state by applying an optical

pulse. Another pulse can be used to reconvert the ground-state coherence into an optical coherence for readout.

Another challenge for the implementation of the AFS memory protocol is the large range over which the atomic frequency has to be swept. As we discussed earlier, to avoid mixing the eigenmodes of the system, the range of swept atomic frequency should be larger than the coupling constant ($\Delta_0 \gg \beta \gg \Delta\omega$). For the system proposed here (Ref.[110]), the swept frequency range should be of the order of 100 GHz. This challenge can be overcome by increasing the length of medium, which allows decreasing the coupling constant without compromising the optical depth.

4.5 Conclusions and Outlook

The polaritonic description given above made it clear that the AFS memory has significant similarities with EIT based memories. As we mentioned in the introduction, the AFS memory is also connected to the GEM memory in the regime in which the size of the pulses is smaller than the length of the medium. Numerical calculations (shown in Figure 4.9 in Appendix 3) also verify this connection. This suggests the notion of a real-space polariton in the GEM memory which differs from the momentum-space polariton introduced in Ref. [113]. Nevertheless there are some differences between AFS and GEM protocols even in the small pulse regime. In AFS the pulse slows down and stops when the atoms are far detuned from the pulse (after having been swept through the resonance). In contrast, in GEM the pulse stops close to the resonant part of the medium, or, if the optical depth is high enough, even before the resonant part of the medium is reached. This fact leads to the shift in the release time of the output that can be seen in Figure 4.9 of the appendix 3.

The AFS memory is linked to photon echo based memories more generally. When we sweep the atomic frequency in time, the atomic coherences become dephased and thus re-emission is inhibited. By sweeping in reverse direction, the atomic coherences become

rephased and the light is re-emitted. This fact imposes some limits on sweeping the atomic frequency. The sweep should be fast enough compared to the coupling constant to ensure that dephasing happens before reemission. The details of the outlined dephasing-rephasing process for the AFS memory are a subject for future studies.

Our protocol also shares some similarities with the proposal of Ref. [115], where light guided by Coupled Resonator Optical Waveguides (CROW) is stored by dynamically changing the resonance frequency of side cavities that are coupled to the CROW. In the AFS protocol the atoms play the role of the side cavities in Ref. [115].

It is also worth pointing out that there are some similarities between the AFS memory and Ref. [114], which proposes to store light by dynamically controlling the splitting of two atomic transitions. These authors also develop a polaritonic picture for their protocol.

In conclusion we have proposed and analyzed a quantum memory protocol based on sweeping the resonance frequency of two-level atoms. We have shown that this new AFS memory protocol shares features with several other existing memory protocols, including EIT and photon-echo based memories. Besides being interesting in its own right, this new protocol can thus also be seen as a step towards a unified description of the complex zoology of quantum memory protocols.

4.6 Appendix 1. Investigation of AFS requirements

As discussed in the paper, for obtaining the polaritonic picture we have assumed the three conditions of Eq. 4.12-4.14. Condition (4.12) is essential for initially exciting only one of the polaritons. Condition 4.13 guarantees the adiabaticity of the process, thus avoiding leakage from one polariton to the other polariton. Condition 4.14 prevents dispersion, which is important for achieving high fidelity. Here we numerically study these conditions.

First, figures 4.5 (a-g) show what happens when condition (4.12) is violated. It can be seen that by decreasing the initial detuning (while the other conditions are fulfilled), we

excite polariton Φ (i) more and polariton Ψ (ii) less. According to Eq. (4.10) and Eq. (4.11) in the paper, as we change the detuning, polariton Ψ slows down and converts to polarization, while polariton Φ accelerates from zero group velocity to the speed of light and leaves the medium. Therefore excitation of polariton Φ leads to loss. When the starting detuning is much less than the coupling rate (Figure 4.5f), θ is almost $\pi/4$, so according to Eq. 4.10 and Eq. 4.11 both polaritons travel with speed $c/2$ and, since they have opposite phase ($\lambda_1 = \beta$ and $\lambda_2 = -\beta$), there is beating between them. This means that the light undergoes a series of re-emission and absorption processes with rate β (see also Figure 4.5d).

Secondly we examine the adiabaticity condition 4.13. Figures 4.6(a-g) show how the output field changes when we violate the adiabaticity condition. As we increase $\dot{\Delta}$ (while the other two conditions hold), the process becomes less adiabatic, resulting in leakage of polariton Ψ (ii) into polariton Φ (i), which accelerates to the speed of light and leaves the medium. Therefore this condition is necessary for efficient absorption of the light.

Thirdly we study the effect of violating condition (4.14). Figure.4.7 show how the output changes when the coupling rate approaches the bandwidth of the pulse. It can be seen that when β approaches the bandwidth of the pulse, the output pulse becomes broader, which reduces the fidelity of the memory protocol. This can be explained by considering the expansion of the eigenvalues in terms of k. When β is comparable to the bandwidth of the pulse, we no longer can neglect second and higher orders of k in expansion of eigenenergies, resulting in dispersion of the pulse.

4.7 Appendix 2. Optimized Sweeping of Atomic Frequency

Thus far we only considered a linear change of detuning in time. However, the linear change is not the most efficient way of changing the detuning. When the atoms are far detuned from the pulse, the sweeping can be made faster without significantly compromising the efficiency, and when the atoms are in resonance with the pulse, the sweeping can be made slower to

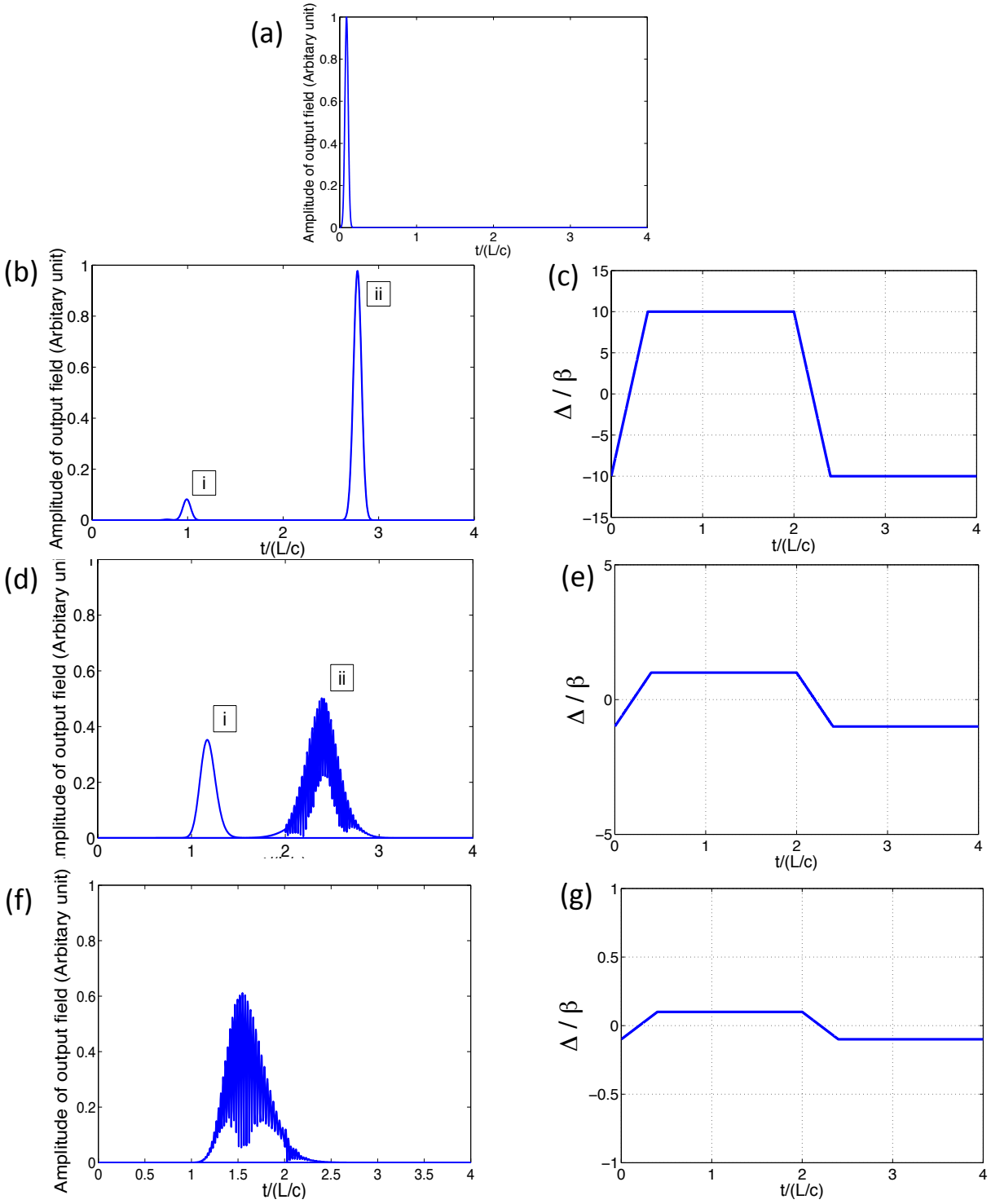

Figure 4.5: Effect of initial detuning on the output of the memory. The bandwidth of the input field is set to $\Delta\omega = 0.1\beta$. (a) shows the temporal shape of the input pulse. Note that the input pulse is initially in the medium . We show the output field for different values of initial detuning b)$\Delta_0 = -10\beta$, d)$\Delta_0 = -\beta$, f)$\Delta_0 = -0.1\beta$. (c), (e), (g) show how the detuning changes in each case. (i) is the transmitted and (ii) is the retrieved pulse.

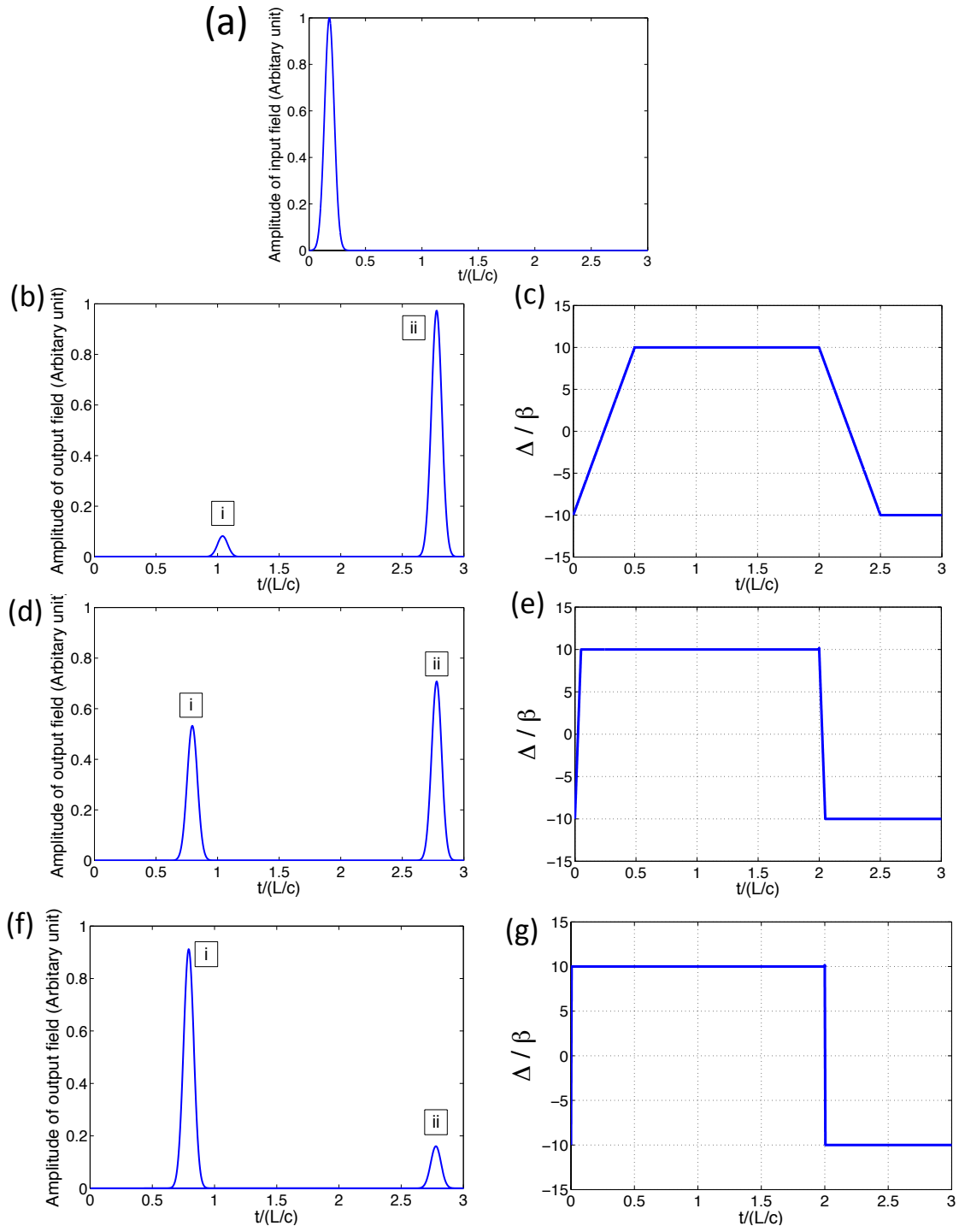

Figure 4.6: Effect of the rate of changing the detuning on the output of the memory. The bandwidth of the input field is set to $\Delta\omega = 0.1\beta$. (a) shows the temporal shape of the input pulse. Note that the input pulse is initially in the medium. The initial detuning for all of the cases is $\Delta_0 = -10\beta$. We sketch the output field for different values of $\dot{\Delta}$, b)$\dot{\Delta} = 0.3\beta^2$, d)$\dot{\Delta} = 3\beta^2$, f)$\dot{\Delta} = 30\beta^2$. (c), (e), (g) show the detuning as a function of time. (i) is the transmitted and (ii) is the retrieved pulse.

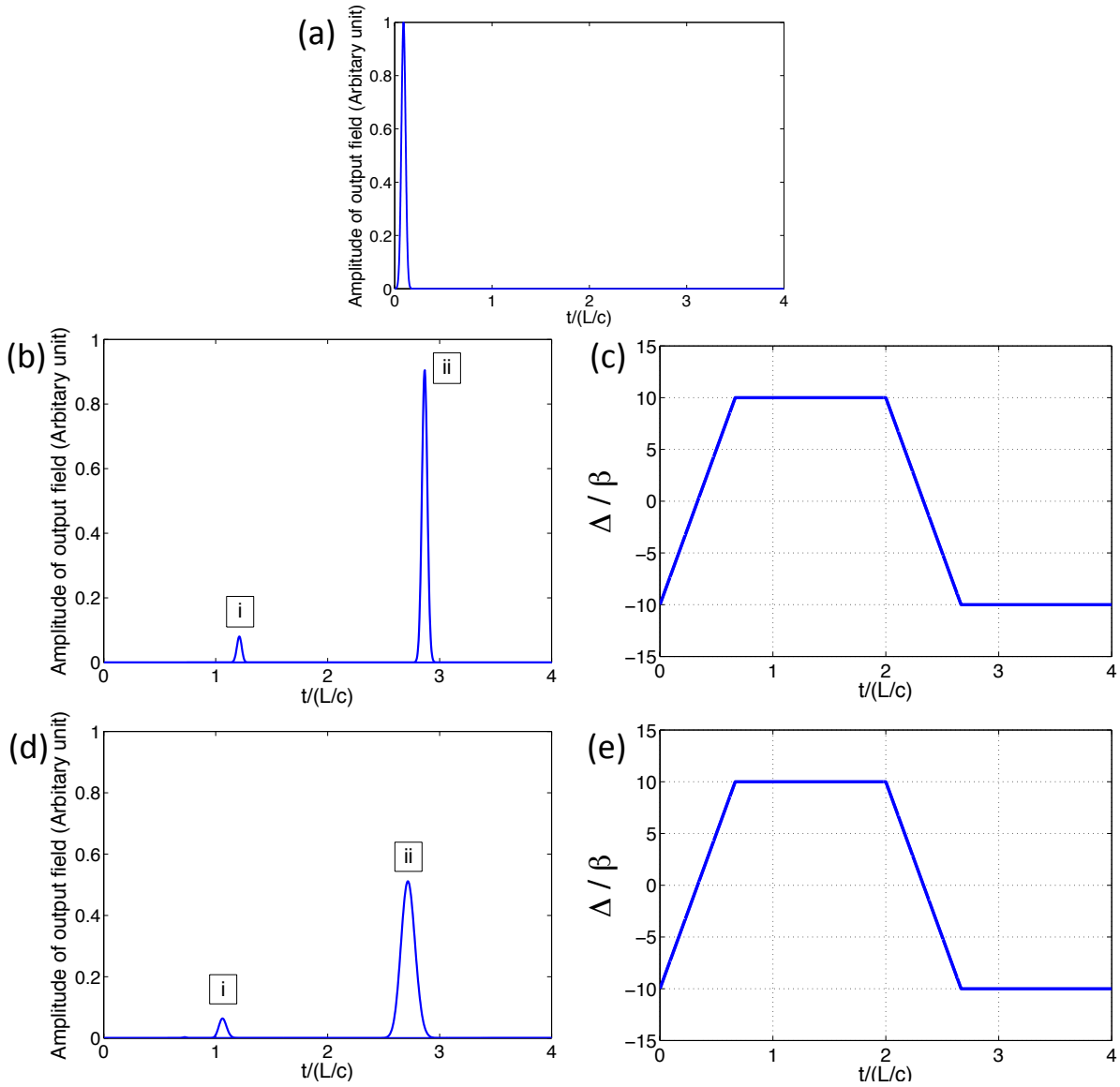

Figure 4.7: Effect of the value of β (compared to the bandwidth of the input pulse) on the output of the memory. (a) shows the temporal shape of the input pulse. Note that the input pulse is initially in the medium. The initial detuning for all of the cases is $\Delta_0 = -10\beta$. We sketch the output field for two different values of β b) $\beta = 16\Delta\omega$, d)$\beta = 4\Delta\omega$. (c), (e) show the detuning as a function of time. (i) is the transmitted and (ii) is the retrieved pulse.

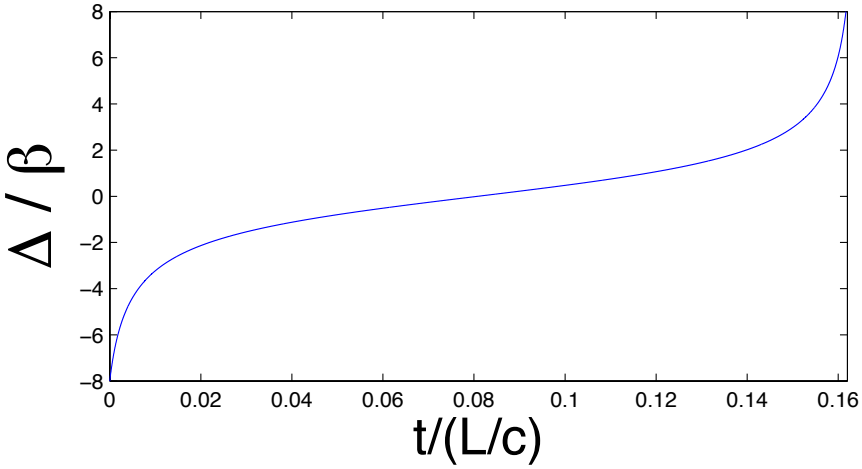

Figure 4.8: nonlinear change of detuning by setting $\dot{\theta} = 0.3 \times (\lambda_1 - \lambda_2/2)$

store the light more efficiently. In general any sweeping that obeys the conditions given in Eq. (4.15) of the paper can store the pulse inside the medium. Here we picked the case in which the decay rate is $\gamma = 5 \times 10^{-2}$ and the optical depth is $d = 300$ and improved the efficiency by setting the rate of sweeping to $\dot{\theta} = 0.3 \times (\lambda_1 - \lambda_2)/2$. Figure 4.8 shows the detuning as a function of time under these conditions. With this nonlinear sweeping we could improve the efficiency from 40% for a linear sweep to 57% for the same input pulse. It may be possible to obtain further improvements by using numerical optimization algorithms.

4.8 Appendix 3. Connection Between AFS and GEM Memory

We have also performed numerical comparisons between GEM [101] and AFS, where in the case of AFS the effective spatial gradient for light propagating at velocity c ($\frac{\dot{\Delta}}{c}$) is set equal to the spatial gradient for GEM. Figure 4.9(a) shows the agreement between outputs of the two protocols. This connection can be captured rigorously by going to the retarded frame ($\tau \rightarrow t - z/c$, $z' = z$). In the retarded frame the time-dependent detuning $\Delta(t)$ is transformed to $\Delta(\tau + z/c)$, which depends on both retarded time and space. However, for pulses smaller than the medium, the term τ can approximately be neglected compared to z/c. As a result

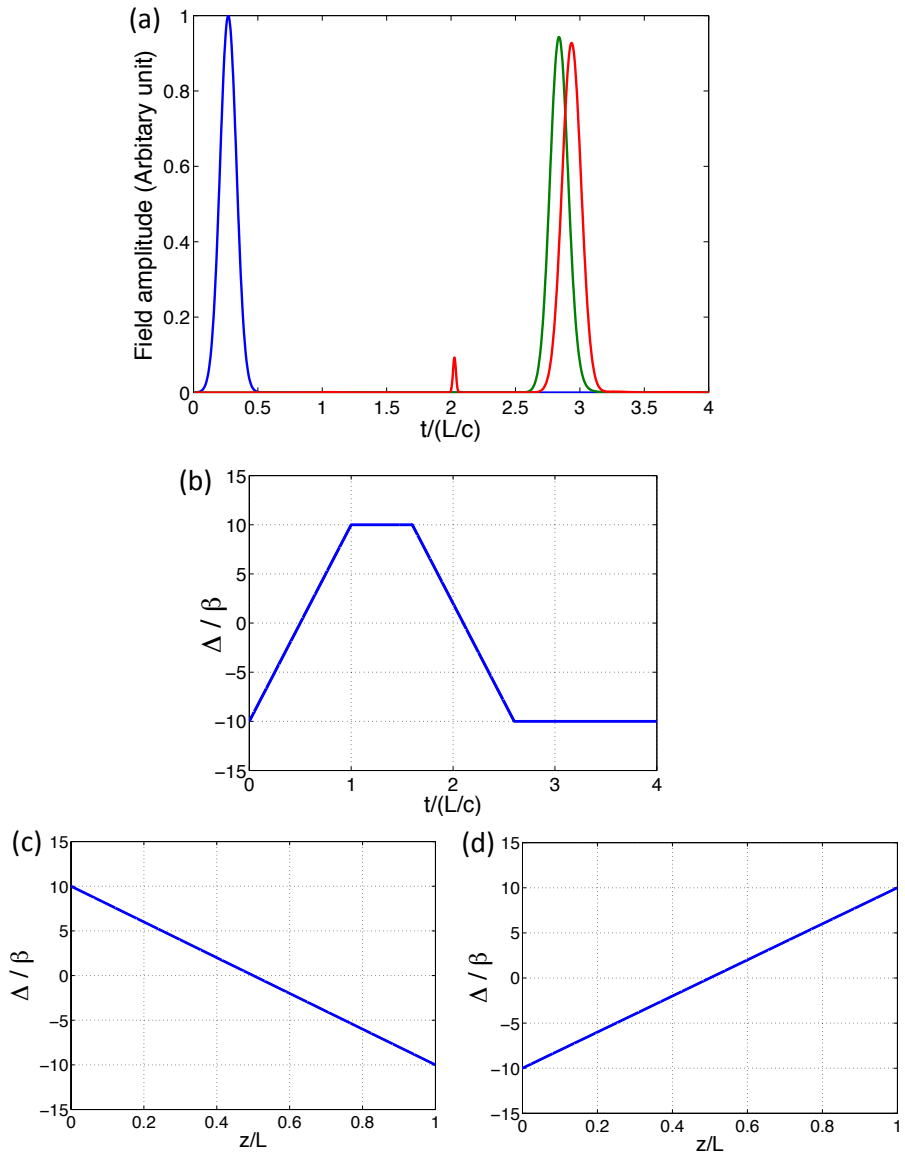

Figure 4.9: (a) Comparison of the AFS memory output (green) with GEM output (red) when we send the same input pulse (blue). (b) illustrates the detuning as a function of time in AFS memory. (c), (d) show the detuning as a function of spatial coordinate respectively for storage and retrieval in GEM memory. In the simulation of GEM, at time t=1.6L/c the detuning of the atoms is flipped. The effective spatial gradient ($\frac{\dot{\Delta}}{c}$) in the AFS memory is set equal to the spatial gradient in GEM for both storage and retrieval.

we end up with a space-dependent detuning $\Delta(z/c)$.

It is important to note that this connection is valid under the assumption that retarded time is much smaller than the temporal extension of medium (L/c), which is true for the short pulses traveling with almost the speed of light. However based on the polaritonic description we know that the pulse slows down in the medium, and as a result the retarded time increases more than the time duration of the pulse and our assumption is no longer valid. What justifies our approximation is that, when the retarded time exceeds L/c, the pulse is almost absorbed. Thus this factor doesn't play an important role. The small discrepancy of the two protocols in figure 4.9 can be explained by the imperfection of this approximation.

Chapter 5

Rydberg Atoms

5.1 Preface

This chapter summarizes the basic physical concepts underlying Rydberg atoms and different types of Rydberg interactions within an ensemble of ultracold atoms.

5.2 Introduction

Rydberg atoms, i.e. the atoms that are excited to high principal numbers (n), were studied in the early days of quantum mechanics [116, 117]. Rydberg excitation of ultracold atoms [118] revolutionized the field and resulted in a variety of applications. Ultracold Rydberg physics has been applied in neutral atom quantum computation [119], quantum non-linear optics [56, 45, 57], strongly correlated plasmas [120, 121], ultracold chemistry (e.g. Rydberg Molecules)[122], studies of exotic quantum phases [123, 124], and many-body entangled states [125, 126]. To reduce the experimental complexity, there is currently an effort to perform Rydberg experiments in hot vapors [127] and also in semiconductors [128, 129], where the latter might be applicable in the generation of on-chip quantum computers.

Laser manipulation of atomic states can serve as an effective switch for controlling the Rydberg interaction. This fast switching over 12 orders of magnitude contrast in the interaction strength, makes Rydberg atoms attractive for quantum science and technology, see Fig. 5.1 and [44]. Comparing to the ionic system with permanent strong Coulomb interaction, switchable weaker interaction between neutral atoms might be an advantage for the realization of many qubit registers.

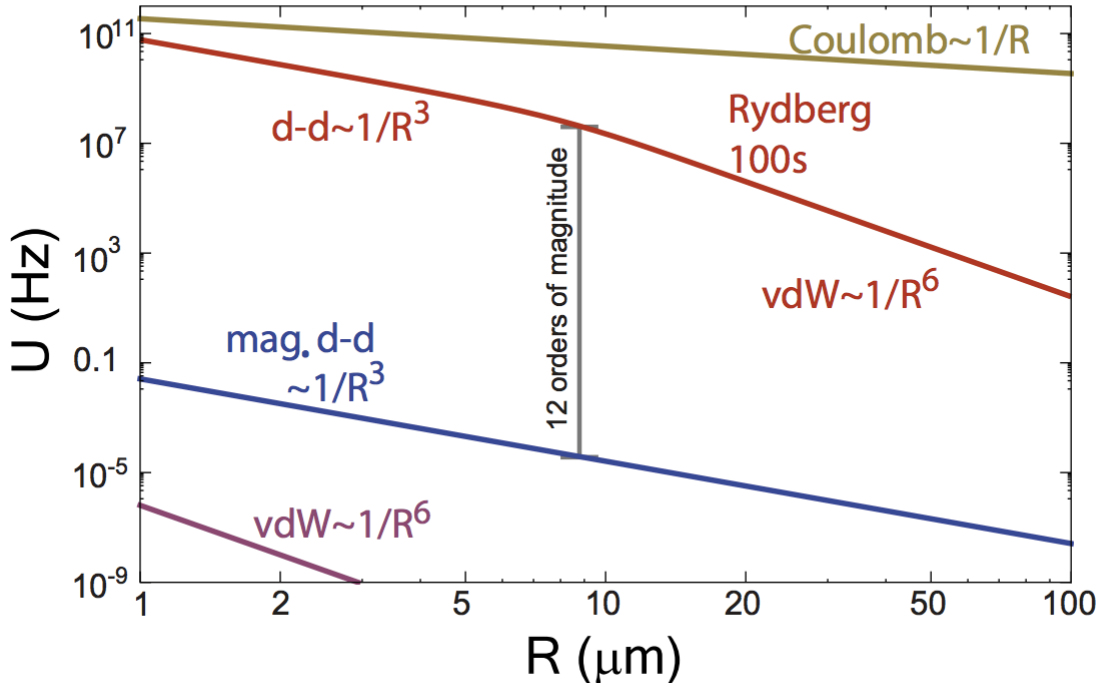

Figure 5.1: (Color online) Interaction between two Rubidium atoms in ground state, two atoms that are excited to $100S$ Rydberg state and two Rb ions. Laser manipulation of atomic states can serve as an effective switch for controlling the Rydberg interaction. This fast switching over 12 orders of magnitude contrast in the interaction strength, makes Rydberg atoms attractive for quantum science and technology. Rydberg interaction changes from dipole-dipole type $\frac{C_3}{r^3}$ at short distances to van der Waals type $\frac{C_6}{r^6}$ at large separations. (This figure is used with the curtesy of [44])

5.3 Rydberg Atom Properties

Rydberg atoms have exaggerated properties compared to the ground state atoms. Their large size ($r \propto n^2$) can be of order of $1\mu m$ when excited to the principal number of $n = 100$, resulting in a large dipole coupling to the neighboring levels $\mu_{rr'} = \langle r|\mu|r'\rangle \propto n^2$. Large dipoles along with small level spacing $\Delta E_{rr'} \propto n^{-3}$ at high principal numbers results in strong long-range switchable van-der-Waals ($\propto n^{11}$) and dipole-dipole ($\propto n^4$) interactions between Rydberg atoms.

On the other hand diminishing overlap of the Rydberg and ground state wave-functions reduces the transition dipole moments to the ground state $\mu_{rg} \propto n^{-3/2}$, which results in

longer lifetimes on the order of $100\mu s$ at $n = 50$. Some of the scaling laws of Rydberg atom characteristics are presented in table 5.1 and are discussed in detail in this chapter.

Property	scaling
Binding energy	n^{-2}
Level spacing	n^{-3}
Orbital radius $\langle r \rangle$	n^2
Dipole moment $\mu_{rr'}$	n^2
Transition dipole moment μ_{rg}	$n^{-3/2}$
Polarizability α	n^7
Radiative lifetime	n^3
Black-body lifetime	n^2
van der Waals interaction	n^{11}
Dipole-Dipole interaction	n^4

Table 5.1: Rydberg atoms scaling lows.

5.4 Energy Levels

The Hydrogen like energy structure of highly excited Rydberg atoms is due to the small overlap of the excited electron and the ionic core. Effects of ionic core structure are included using the state dependent quantum defects δ_{nlj} (see table 5.2) term as

$$E_{nl} = \frac{-R}{(n - \delta_{nlj})^2} \tag{5.1}$$

where $R = 13.61eV$ is the Rydberg constant and n is the principal quantum number. In contrast to hydrogen, the energy of Rydberg states are not degenerate for different orbital quantum numbers (l) belonging to the same n. This is because for low angular momentum $l < 3$, the Rydberg electron penetrates the ionic core and the interaction with the core's electrons results in nonzero energy defects. Larger angular momentum results in a stronger centrifugal force (see Eq. 5.5) that pushes the Rydberg electron's wave-function away from the core and as a result energy of the state would degenerate ($\delta_{nlj} \approx 0 \,\forall\, l \geq 3$). The scaling of the Rydberg energy levels and energy separation of neighboring levels can be found from Eq. 5.1 as $E_r \propto n^{-2}$ and $\Delta E_{rr'} = E_r - E_{r'} \propto n^{-3}$ respectively.

l	j	b_1	b_2
0	1/2	3.1311804	0.1784
1	1/2	2.6548849	0.2900
1	3/2	2.6416737	0.2950
2	3/2	1.34809171	-0.60286
2	5/2	1.34646572	-0.596
3	5/2	0.0165192	-0.085
3	7/2	0.0165437	-0.086

Table 5.2: Quantum defects $\delta_{n,l,j} = b_1(l,j) + b_2(l,j)/(n - b_1(l,j))^2$ data for Rubidium [131, 132]. Dependents on j is small.

5.5 Wave-Function

In the case of Alkaline atoms, where the Rydberg electron is far from the finite size closed shell core the Schrödinger equation of the Rydberg electron can be written as [130]

$$(-\frac{\hbar^2}{2\mu}\nabla^2 + V_C(r))\psi_{nlm}(r) = E_{nl}\psi_{nlm}(r) \tag{5.2}$$

where $\hbar$ and μ are the reduced Planck constant and reduced mass of the Rydberg electron respectively. The widely used effective core potential is [133, 134]

$$V_C(r) = \frac{q^2}{4\pi\epsilon_0 r}[1 + (Z-1)e^{-a_1(l)r} - r(a_3(l) + a_4(l)r)e^{-a_2(l)r})] - \frac{\alpha_c}{2r^4}(1 - e^{-(\frac{r}{r_c})^6}) \tag{5.3}$$

where q is the electron charge, ϵ_0 is the vacuum permittivity and $a_i(l)$ are parameters that depend on the orbital angular momentum [135, 136]; α_c is the core dipole polarizability [137, 138] and r_c is the cut off radius that prevents any divergence at the origin. Eq. 5.3 shows that far from the core, the Rydberg electron experiences a Coulomb like potential. At distances closer to the nucleus, the potential has significant deviations due to the penetration of the Rydberg electron into the core as determined by the second and third terms of Eq. 5.3, and also due to the polarization of the core that is given by the last term of the Eq. 5.3.

The wave-function of the Rydberg electron ψ_{nlm} can be decomposed into radial R_{nl} and angular Y_{lm} terms.

$$\psi_{nlm}(r) = R_{nl}(r)Y_{lm}(\theta,\phi) \tag{5.4}$$

The radial part of the schrödinger equation will be

$$[-\frac{\hbar^2}{2m}(\frac{d^2}{dr^2}+\frac{2}{r}\frac{d}{dr}-\frac{l(l+1)}{r^2})+V_C(r)]R_{nl}(r)=E_{nl}R_{nl}(r). \tag{5.5}$$

Applying the following substitution [139]

$$x=\sqrt{r},\ u(x)=r^{3/4}R(r) \tag{5.6}$$

transforms equation 5.5 to a form that can be solved numerically using the Numerov method namely [140]

$$\frac{d^2u}{dx^2}=f(x)u(x). \tag{5.7}$$

If x increases in the size increments of h then $u(x+h)$ can be found from $u(x)$ and $u(x-h)$ using the equation [140]

$$u(x+h)[1-T(x+h)]+[1-T(x-h)]u(x-h)=[2+10T(x)]u(x)+O(h^6), \tag{5.8}$$

where $T(x)=\frac{h^2f(x)}{12}$. Figure 5.2 plots the Rubidium's wave-function for two states of $|n=50,l=0\rangle$ (plotted in blue) and $|n=100,l=0\rangle$ (plotted in red) which are extended 100 and 400 times beyond the size of Rubidium ground state atom.

5.6 Transition Dipoles

The transition between different atomic states is determined by dipole matrix elements [141]

$$\mu_{nljm,n'l'j'm'}=e\langle n'l'j'm'|\vec{r}|nljm\rangle=(-1)^{j+l'-1/2}C^{j'm'}_{jmlp}\sqrt{2j+1}\begin{Bmatrix} l & 1/2 & j \\ j' & 1 & l' \end{Bmatrix}\langle n'l'||r||nl\rangle \tag{5.9}$$

where e is the charge of the electron, and the equation contains the radial transition term

$$r_{nl,n'l'}=\langle n'l'||r||nl\rangle=\int r^3R_{nl}(r)R_{n'l'}(r)\,dr, \tag{5.10}$$

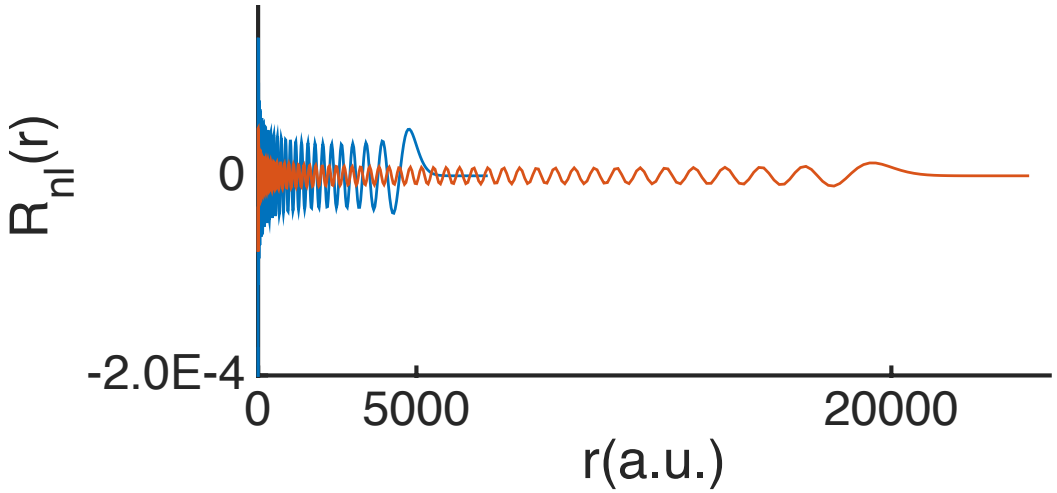

Figure 5.2: (Color online) Rydberg electron's radial wave-function for $|n = 50, l = 0\rangle$ (plotted in blue) and $|n = 100, l = 0\rangle$ (plotted in red). The Rydberg wave-function extends to 5000 a.u. and 20000 a.u. respectively which are far beyond the extension of ground state atom.

which can be calculated numerically. The angular part is given by Clebsch-Gordon coefficients [142] and can be calculated in terms of Wigner-3j-symbols [143]. The angular part gives the dipole selection rules, namely $\Delta m = 0, \pm 1$, $\Delta l = \pm 1$, $\Delta j = 0, \pm 1$, (When coupling the Rydberg pairs in Sec. 5.8, the conservation of total angular momentum for the case that inter-atomic separation is along the quantization axes results to $\Delta M = \Delta m_1 + \Delta m_2 = 0$ [144]). The radial part gives the scaling with respect to n. The transition dipoles from a Rydberg level n to its neighboring levels $n-1 \leq n' \leq n+1$ scale with n^2 (see Fig. 5.3), which results in larger dipoles and therefore stronger interactions at higher principal numbers (see section 5.8 for more discussion). On the other hand the diminishing overlap of the Rydberg and ground state wave-functions reduces the transition dipole moments to the ground state $\mu_{rg} \propto n^{-3/2}$, which results in longer lifetimes, e.g. of the order of $100\mu s$ at $n = 50$.

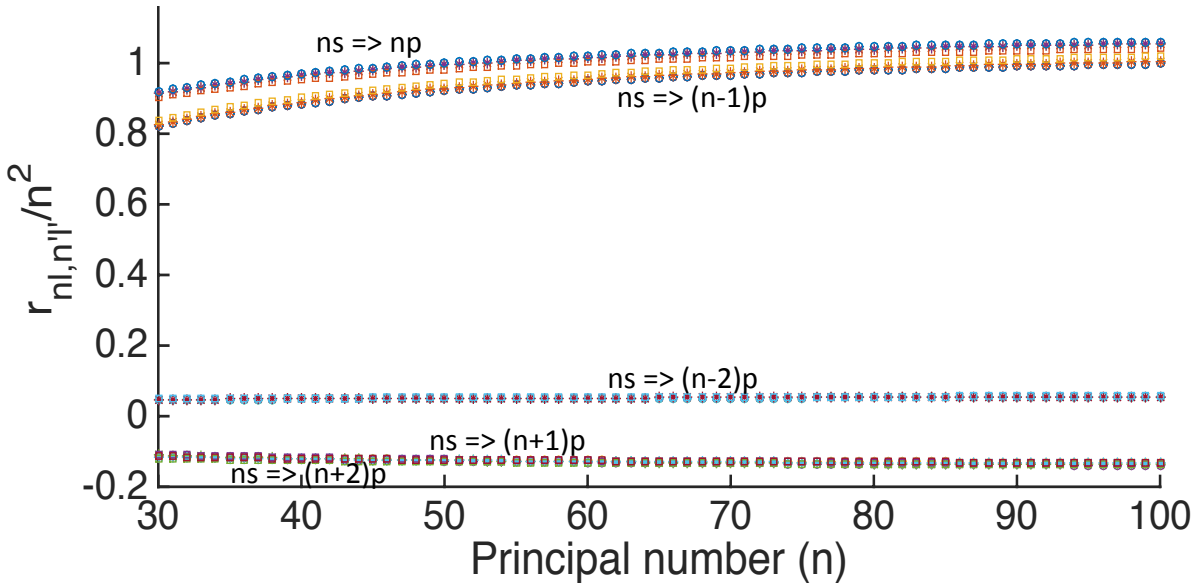

Figure 5.3: Radial matrix elements divided by n^2 in Strontium atom for the transitions of $n\,^1S_0 \rightarrow n'\,^3P_{[0,1,2]}$. This figure shows that for principal numbers larger than n=30 dipole moments almost scale with n^2. Note that in Alkaline earth Rydberg atoms with principal numbers below $n = 30$, effects of the second valance electron should be considered, and the dipole moments can be calculated via multichannel quantum defect theory [145].

5.7 Lifetime

Natural lifetime of Rydberg state $|i\rangle$ is given by the sum of spontaneous transition rates to the lower states ($|f\rangle$) using Einstein A coefficients [146, 147, 148]

$$\tau^{-1} = \sum_f A_{if} = \frac{2e^2}{3\epsilon_0 c^3 h} \sum_{E_f<E_i} \omega_{if}^3 \, |\langle i|\vec{r}|f\rangle|^2, \tag{5.11}$$

where $\omega_{if} = \frac{E_f - E_i}{\hbar}$ is the transition frequency and $\langle i|\vec{r}|f\rangle$ is the dipole matrix element between initial and final states. For Rydberg states with small angular momentum (l) the dominant terms in the sum of Eq. 5.11 are determined by the transition frequency ω_{if} and therefore the dominant destination will be the dipole allowed ground states. Considering the scaling, the transition frequency of the Rydberg levels to the ground state is almost independent of the principal number, which leaves the transition dipole term that scales as $n^{-3/2}$ for transitions to small principal number states. Therefore the natural lifetime of

Rydberg states with low l scales with n^3. For Rydberg states with large orbital angular momentum ($l \approx n-1$) the transition to the ground state occurs through many intermediate decays to neighboring Rydberg levels with lower l to fulfill dipole selection rules. In this case the transition frequency scales with $\omega_{if} \propto n^{-3}$ and the radial matrix element scales with $\mu_{if} \propto n^2$ which results to the overall scaling of $\tau \propto n^5$. Therefore, high orbital angular momentum Rydberg states have longer lifetimes. However these states are experimentally hard to reach.

In the presence of black body radiation the natural line width of the state depends on the coupling to the thermal fields in addition to the vacuum, which results to [146, 147, 148]

$$\tau^{-1} = \sum_f (1 + \frac{1}{e^{\frac{\hbar\omega_{if}}{k_B T}} - 1}) A_{if} + \sum_{f'} \frac{A_{if'}}{e^{\frac{\hbar\omega_{if'}}{k_B T}} - 1} \tag{5.12}$$

where f and f' are the states with lower and higher energies respectively comparing to the initial states, $(e^{\frac{\hbar\omega_{if}}{k_B T}} - 1)^{-1}$ is the average number of thermal photons with energy of ω_{if} at the environment temperature of T, and k_B is the Boltzmann constant.

5.8 Rydberg-Rydberg Interaction

Considering two Rydberg atoms with nuclei positions of $\vec{R_1}$, $\vec{R_2}$ and separation of $\vec{R} = \vec{R_2} - \vec{R_1}$, and a corresponding Rydberg electron-nucleus separation of $\vec{r_i}$, the Hamiltonian of the system is

$$H = H_0^1 + H_0^2 + V_{int}(\vec{r_1}, \vec{r_2}, \vec{R}). \tag{5.13}$$

The individual atoms' Hamiltonians are given by

$$H_0^i = -\frac{1}{2}\nabla_i^2 + V_c(\vec{r_i}), \tag{5.14}$$

where V_c is defined in equation 5.3. The interaction between the two atoms is given by

$$V_{int}(\vec{r_1}, \vec{r_2}, \vec{R}) = e^2[\frac{1}{|\vec{R}|} - \frac{1}{|\vec{R} - \vec{r_1}|} - \frac{1}{|\vec{R} + \vec{r_2}|} + \frac{1}{|\vec{R} - (\vec{r_1} - \vec{r_2})|}]. \tag{5.15}$$

When the inter-atomic distance between the two Rydberg atoms R is much larger than their individual Bohr radius ($R \gg n^2 a_0$), one can Taylor expand each term of Eq. 5.15

$$f(x) = \frac{1}{|\vec{R} - \vec{x}|} \tag{5.16}$$

to the second order to find

$$\begin{aligned} f(x) &= f(0) + \sum_{i=1}^{3} x_i \partial_i f(0) + \frac{1}{2} \sum_{i,j=1}^{3} x_i x_j \partial_{ij} f(0) + O(3) \\ &\approx \frac{1}{R} + \frac{\vec{x}.\vec{R}}{R^3} + \frac{3}{2R^5}(\vec{x}.\vec{R})^2 - \frac{x^2}{2R^3}. \end{aligned} \tag{5.17}$$

Substituting these terms into Eq. 5.15 results in the dipole-dipole approximation of the interaction

$$\begin{aligned} V_{int}(\vec{r_1}, \vec{r_2}, \vec{R}) &= e^2[f(0) - f(\vec{r_1}) - f(-\vec{r_2}) + f(\vec{r_1} - \vec{r_2})] \\ &\approx e^2 \frac{1}{R^3}[\vec{r_1}.\vec{r_2} - 3(\vec{r_1}.\hat{R})\,(\vec{r_2}.\hat{R})] = V_{dd} \end{aligned} \tag{5.18}$$

Considering a pair of Rydberg atoms $|n_1 l_1 j_1, n_2 l_2 j_2\rangle$, the dipole-dipole interaction couples the neighboring Rydberg pair states $|n_1' l_1' j_1', n_2' l_2' j_2'\rangle$ that fulfill the dipole selection rules (explained in Sec. 5.6) with the coupling strength of

$$\begin{aligned} &\langle n_1 l_1 j_1, n_2 l_2 j_2 | \hat{V}_{dd} | n_1' l_1' j_1', n_2' l_2' j_2' \rangle \\ &= \frac{r_{n_1 l_1, n_1' l_1'} r_{n_2 l_2, n_2' l_2'}}{R^3}[\vec{C}_{1,1'}.\vec{C}_{2,2'} - 3(\vec{C}_{1,1'}.\hat{R})(\vec{C}_{2,2'}.\hat{R})] \end{aligned} \tag{5.19}$$

where $r_{nl,n'l'}$ is the radial matrix element (see Eq. 5.10), and

$$\vec{C}_{1,1'} = \vec{C}_{l_1 j_1 m_1, l_1' j_1' m_1'} = \int d\phi\, d(\cos\theta) Y^*_{l_1 j_1 m_1}(\theta, \phi) \begin{pmatrix} \sin\theta\cos\phi \\ \sin\theta\sin\phi \\ \cos\theta \end{pmatrix} Y_{l_1' j_1' m_1'}(\theta, \phi) \tag{5.20}$$

is the Clebsch-Gordan coefficient [142] containing the angular contribution to the matrix element. Splitting the radial and angular terms, the dipole-dipole coupling can be written as

$$V_{dd} = \frac{C_3 D_\phi}{R^3} \tag{5.21}$$

were $C_3 = r_{n_1,n_1'} r_{n_2,n_2'}$ contains the radial terms and therefore scales with $C_3 \propto n^4$ and D_ϕ contains the angular parts. There are infinite number of final pairs, however only those with small energy defects $\delta = E(n_1', l_1', j_1') + E(n_2', l_2', j_2') - E(n_1, l_1, j_1) - E(n_2, l_2, j_2)$ predominantly determine the interaction strength due to their large dipoles and small energy gaps.

Considering the closest pair and representing the initial and final pair with $|\psi_i\rangle$ and $|\psi_f\rangle$, the time independent Schrödinger equation describing the dipole coupling is

$$\begin{pmatrix} \delta & \hat{V}_{dd} \\ \hat{V}_{dd}^\dagger & 0 \end{pmatrix} \begin{pmatrix} |\psi_f\rangle \\ |\psi_i\rangle \end{pmatrix} = E \begin{pmatrix} |\psi_f\rangle \\ |\psi_i\rangle \end{pmatrix} \tag{5.22}$$

Isolating ψ_f in the first row

$$|\psi_f\rangle = \frac{V_{dd}}{\delta - E} |\psi_i\rangle \tag{5.23}$$

and substituting it in the second row

$$\frac{V_{dd} V_{dd}^\dagger}{E - \delta} |\psi_i\rangle = E |\psi_i\rangle \tag{5.24}$$

the Förster energy eigenvalues can be found as [44]

$$E = \delta\left(\frac{1}{2} - \sqrt{\frac{1}{4} + \frac{C_3^2}{R^6 \delta^2} D_\phi^2}\right) \tag{5.25}$$

This interaction has different spatial dependence at short and large distances with a crossing point of $R_c = (\frac{\delta}{C_3 D_\phi})^{1/3}$.

Van-der Waals interaction ($R >> R_c$)**:** At large distances the dipole coupling is only perturbative and the energy of pair states is given by

$$E = \frac{C_3^2 D_\phi^2}{\delta R^6} = \frac{C_6 D_\phi^2}{R^6}. \tag{5.26}$$

In this range the interaction is van-der Waals type and C_6 scales like n^{11}. Considering the spatial dependence (R^{-6}), the interaction is predominantly determined by the closest Rydberg atoms and sharp drop of the interaction (see Fig. 5.1) allows one to consider a cut off for the radius.

Resonant dipole-dipole interaction ($R << R_c$): At short distances or when the energy defect δ is tuned to zero (Förster resonance) using external fields, the dipole interaction term dominates and the energy of the coupled pair is

$$E = -sgn(\delta)\frac{C_3 D_\phi}{R^3}. \tag{5.27}$$

This gives the largest energy between two non-overlapping Rydberg atoms and C_3 scales with n^4. The R^{-3} spatial dependence results in a longer range of interaction compared to van-der Waals interaction.

In both cases the attractive or repulsive nature of the interaction is determined by the sign of the energy defect δ.

5.9 Rydberg Blockade

An important consequence of Rydberg interaction is a position dependent level shift, which prevents multiple Rydberg excitations within a sphere of radius R_b [149] by making the atoms out of resonance with the exciting field. The blockade radius R_b is defined as an inter atomic distance where power broadening $\sqrt{\Omega^2 + \Delta^2}$ equals the Rydberg interaction, where Ω is the Rabi frequency and Δ is detuning [150]. The blockade radius is usually on the order of microns, for example in an ensemble of Rubidium atoms that are excited in resonance to $60S_{1/2}$ state with $\Omega/2\pi = 1$ MHz, in the regime of van-der Waals interaction, the blockade radius is $Rb = (\frac{C_6}{\Omega})^{1/6} = 7\mu m$.

Due to the Rydberg blockade all $N_b = N(4/3)\pi R_b^3$ atoms within blockade radius share one Rydberg excitation forming a collective state

$$\frac{1}{\sqrt{N}}\sum_{i=1}^{N} |g_1, g_2, ..., r_i, ..., g_N\rangle. \tag{5.28}$$

This system, which is sometimes called a super-atom [151], is coupled by the laser field to the ground state with a collectively enhanced Rabi frequency $\sqrt{N_b}\Omega$ [152].

5.10 Rydberg Dressing

This section studies the interaction between Rydberg dressed atom. Most of the content is a modified version of a discussion in the monograph of [144]. In this scheme, an off resonant laser weakly couples Rydberg levels to the ground state atoms. This dressing would results to a Plateau type interaction.

Considering N atoms in an optical lattice, for each pair of atoms excited to a Rydberg level $|e\rangle$ and separated by $\mathbf{r}_{ij} = \mathbf{r}_i - \mathbf{r}_j$, where $\mathbf{r}_i$ is the position of ith atom, the binary interaction is $W_{ij} = E(r_{ij})$ where E is defined in Eq. 5.25. The electronic Hamiltonian of the many-body dressed system is

$$\hat{H}_{el} = \sum_{i<j} W_{ij}\hat{\sigma}^i_{ee}\hat{\sigma}^j_{ee} + \sum_{i=1}^{N}[\frac{\Omega}{2}(\hat{\sigma}^i_{ge} + \hat{\sigma}^i_{eg}) + \Delta\hat{\sigma}^i_{ge}], \tag{5.29}$$

where the individual atom dressing Hamiltonian is derived in Sec. 2.2. Note that in spite of the large size of Rydberg atoms which could be in the order of laser wavelength, Dipole approximation is still valid. This is due to the fact that dipole transition is between a ground state to the Rydberg level and external field is constant over the range that two wave-functions has a significant overlap.

We are interested in the potential $U(\mathbf{r}_1..\mathbf{r}_N)$ of the ground dressed state of the many-body system $|G(\mathbf{r}_1..\mathbf{r}_N)\rangle$, which is obtained under adiabatic dressing of the ground state

$$\hat{H}_{el}|G(\mathbf{r}_1..\mathbf{r}_N)\rangle = U(\mathbf{r}_1..\mathbf{r}_N)|G(\mathbf{r}_1..\mathbf{r}_N)\rangle. \tag{5.30}$$

In the weak dressing regime $(\frac{\Omega}{2\Delta})^2 \ll 1$ and for the atoms within the blockade radius $W_{ij} > \Delta$, the dressing energy can be found by applying the perturbation theory [144]

$$\frac{U}{\Delta}|G\rangle = [\underbrace{\sum_{i=1}^{N}\hat{\sigma}^i_{ee} + \frac{1}{\Delta}\sum_{i<j} Wij\hat{\sigma}^i_{ee}\hat{\sigma}^j_{ee}}_{\hat{h}_0} + \underbrace{\frac{\Omega}{2\Delta}}_{\lambda}\underbrace{\sum_{i=1}^{N}(\hat{\sigma}^i_{ge} + \hat{\sigma}^i_{eg})}_{\hat{v}}]\,|G\rangle, \tag{5.31}$$

where

$$\hat{h}_0 = \sum_{i=1}^{N}\hat{\sigma}^i_{ee} + \frac{1}{\Delta}\sum_{i<j} Wij\hat{\sigma}^i_{ee}\hat{\sigma}^j_{ee} \tag{5.32}$$

is the unperturbed Hamiltonian,

$$\hat{v} = \sum_{i=1}^{N} (\hat{\sigma}_{ge}^{i} + \hat{\sigma}_{eg}^{i}) \tag{5.33}$$

is the perturbing term and $\lambda = \frac{\Omega}{2\Delta}$. There are 2^N eigenstates of $\hat{h}_0$ that can be labeled as $|a\rangle$ and numbered as follows

$$\begin{aligned} |0\rangle &= |g, g, ..., g\rangle \\ |1\rangle &= |e, g, ..., g\rangle \\ &\vdots \\ |N+1\rangle &= |e, e, ..., g\rangle \\ &\vdots \\ |2^N\rangle &= |e, e, ..., e\rangle, \end{aligned} \tag{5.34}$$

with eigenenergies of $\epsilon_a = \langle a|\hat{h}_0|a\rangle$ and the energy separation of $\epsilon_{ab} = \epsilon_a - \epsilon_b$. Important examples in this discussion are the energy of ground state $\epsilon_0 = \langle 0|\hat{h}_0|0\rangle = 0$, energy of N single excited states $\epsilon_a = \langle a|\hat{h}_0|a\rangle = 1$ for $a\epsilon[1...N]$ and double excited states with the energy of $2 + W_{ij}/\Delta$. The coupling between these eigenstates is given by $v_{ab} = \langle a|\hat{v}|b\rangle$ which could be 0 or 1.

The effective energy of the ground dressed state $|G\rangle$ is given by perturbation theory

$$U = \Delta \sum_{l=1}^{\infty} \lambda^l u^{(l)}, \tag{5.35}$$

where the energy contribution of lth order ($u^{(l)}$) contains l excitation or de-excitation operators ($\hat{v}$) that start from and return back to $|0\rangle$. This condition is fulfilled only by even orders of perturbation while the odd orders return zero e.g. $u^{(1)} = \langle 0|\hat{v}|0\rangle = 0$. The first even order is

$$u^{(2)} = \sum_{a} \frac{|v_{0a}|^2}{\epsilon_{0a}} = N, \tag{5.36}$$

where only the states with one atom excitation get coupled. The total contribution from the second order perturbation is

$$\Delta\lambda^2 u^{(2)} = \frac{\Omega^2}{4\Delta}N, \tag{5.37}$$

which equals to the first order light shift of N non-interacting atoms.

The next non-vanishing perturbation is of interest since it contains the interaction of two excited Rydberg atoms. The fourth order can be calculated as

$$\begin{aligned} u^{(4)} &= \sum_{abc} \frac{v_{0a}v_{ab}v_{bc}v_{c0}}{\epsilon_{0a}\epsilon_{0b}\epsilon_{0c}} - N\sum_{a}\frac{|v_{0a}|^2}{\epsilon_{0a}^2} \\ &= \sum_{i<j}\frac{4}{(1)(2+W_{ij}/\Delta)(1)} - N^2 \end{aligned} \tag{5.38}$$

with the energy contribution of

$$\begin{aligned} \Delta\lambda^4 u^{(4)} &= \frac{\Omega^4}{4\Delta^2}\sum_{i<j}\frac{1}{(2\Delta+W_{ij})} - (\frac{\Omega}{2\Delta})^4\Delta N^2 \\ &\approx \frac{\Omega^4}{8\Delta^3}\sum_{i<j}[\frac{1}{(1+\frac{W_{ij}}{2\Delta})} - 1] \end{aligned} \tag{5.39}$$

Considering van-der Waals interaction between atoms $W_{ij} = \frac{C_6}{r_{ij}^6}$ and including the contribution from the second order of the perturbation from Eq. 5.37 one can find the effective potential of the ground dressed state as

$$U(\mathbf{r}_1..\mathbf{r}_N) = \frac{\Omega^2}{4\Delta}N + \sum_{i<j}^{N}\frac{\chi_0 R_b^6}{R_b^6 + r_{ij}^6} \tag{5.40}$$

where $\chi_0 = \frac{\Omega^4}{8\Delta^3}$ and blockade radius in the weak dressing regime equals to $R_b = (\frac{C_6}{2\Delta})^{1/6}$. This energy corresponds to the effective many-body dressing Hamiltonian of

$$\hat{H}(\mathbf{r}_1..\mathbf{r}_N) = \frac{\Omega^2}{4\Delta}\hat{N} + \sum_{i<j}^{N}\frac{\chi_0 R_b^6}{R_b^6 + r_{ij}^6}\hat{\sigma}_{ee}^i\hat{\sigma}_{ee}^j \tag{5.41}$$

Equation 5.41 shows that the many-body dressing interaction is the sum of binary dressing interactions in the weak dressing regime. This binary dressing interaction is of a diluted van-der-Waals form at distances larger than the blockade radius with reduced coefficient

$$C_6' = \chi_0 R_b^6 = (\frac{\Omega}{2\Delta})^4 C_6 \tag{5.42}$$

where $(\frac{\Omega}{2\Delta})^4$ is the probability of exciting two atoms. within the blockade radius, dressing interaction approaches a constant value

$$\chi(r_{ij}) = \chi_0. \tag{5.43}$$

5.11 Conclusion

This section reviewed the important concepts about Rydberg atoms and their interaction. Exaggerated properties of Rydberg atoms are discussed and the corresponding scaling laws are derived. The interaction between Rydberg atoms is analyzed and the steps in calculating them are advised. The consequent important phenomena namely Rydberg blockade and Rydberg dressing are explained. These results will be used widely in the following chapters.

Chapter 6

Photon-Photon Gate Via the Interaction Between Two Collective Rydberg Excitations

This chapter explains a scheme for a deterministic controlled-phase gate between two photons that is based on the strong interaction between two stationary collective Rydberg excitations in an atomic ensemble outside the regime of Rydberg blockade. The distance-dependent character of the interaction causes both a momentum displacement of the collective excitations and unwanted entanglement between them. I show that these effects can be overcome by swapping the collective excitations in space and by optimizing the geometry, resulting in a photon-photon gate with high fidelity and efficiency.

The content of this chapter is entirely the result of my research and has been published in [57]. I also wrote the manuscript with guidance from Prof. Simon.

6.1 Introduction

Two-qubit photonic gates is the challenging part of universal photonic gates, because photons interact extremely weakly with each other in free space. These gates could specifically improve the performance of quantum repeater [153]. Two-qubit photonic gates are categorized into deterministic and non-deterministic gates. In non-deterministic group, KLM protocol [154] introduced an effective interaction between photons based on linear optics and post-selection. Later on, one-way quantum computation was introduced [155, 156], which is non-deterministic in the initialization of photonic cluster states [157]. In deterministic gates mutual interaction of photons is obtained from their interaction with atomic media. Source of interaction between two photons could be local AC-stark shift between two photons inter-

acting with the same atom [158, 159, 160], a non-local Rydberg interaction between highly excited atoms[119], the collision of atoms in BEC [161] or using cavity-QED to make two successive photons interacting with a single atom in cavity [162, 163].

Here we are interested in an attractive approach that involves converting the photons into atomic excitations in highly excited Rydberg states, which exhibit strong interactions. Rydberg state based quantum gates between individual atoms and between atomic ensembles have been proposed [164, 165, 166, 167, 168] and implemented [169, 170, 171]. There are two categories of gates, those relying on the interaction between two excited atoms [164, 165], and those based on Rydberg blockade [165, 166, 167, 168, 169, 170, 171], where only one atom is excited at any given time. There is a significant body of work studying the effects of mapping photons onto collective atomic Rydberg excitations [172, 173, 174, 175, 176, 177, 178]. Most proposals for photon-photon gates involve propagating Rydberg excitations (polaritons), either using blockade [179, 180] or two excitations [181, 182, 183, 184].

Separating the interaction process and propagation makes it easier to achieve high fidelities for these photonic gates [185]. Such separation can be achieved by photon storage, i.e. by converting the photons into stationary rather than moving atomic excitations. The only storage-based photonic gate that has been proposed so far is based on the blockade effect [185]. Achieving blockade conditions can be challenging since both photons have to be localized within the blockade volume.

Following [164, 165, 181, 182, 183, 184], we here propose a storage-based scheme that instead relies on the interaction between two stationary Rydberg excitations. The interaction is strongly distance-dependent and thus not uniform over the profiles of the two stored photons. We show that this leads to a displacement of the collective excitations in momentum space and to entanglement between their quantum states. These effects a priori reduce the photon-photon gate fidelity. However, it is possible to completely compensate the first effect by swapping the collective excitations in the middle of the interaction time, and to greatly

alleviate the second effect by optimizing the shape and separation of the excitations, resulting in a photon-photon gate that achieves both high fidelity and high efficiency.

6.2 Scheme

Now we describe our scheme in detail. As shown in Fig. 6.1a, information is encoded in dual-rail qubits [186], where the computational basis ($|0\rangle, |1\rangle$) is defined by two spatially separated paths. To implement a conditional phase gate between control (C) and target (T) qubits, we store all four rails in a cold alkaline atomic gas. All four rails are stored and retrieved through non-Rydberg EIT in a lambda configuration (see Fig. 6.1b - Circle 1), which completely decouples the Rydberg interaction from the propagation. In comparison, the scheme of Ref. [185] relies on Rydberg EIT (i.e. a ladder system involving a Rydberg state), such that the propagating polaritons are still interacting, albeit less strongly than the stored excitations.

The truth table for a controlled phase gate (with a controlled phase of π) is

$$|a_C\rangle |a_T\rangle \rightarrow e^{i\pi a_C a_T} |a_C\rangle |a_T\rangle , \tag{6.1}$$

where $a \,\epsilon\, \{0, 1\}$ and the phase is created under the condition that both photons are in the interacting rails ($|1\rangle_C, |1\rangle_T$). Therefore, we only excite the interacting rails to Rydberg levels through optical π pulses (see Fig. 6.1a, 1b-Circle 2), where the Rydberg interaction changes the energy of the interacting pair's state ($|1_C 1_T\rangle$) and lets it accumulate a phase over time compared to the non-interacting pairs ($|1_C 0_T\rangle, |0_C 1_T\rangle, |0_C 0_T\rangle$). After the mentioned preparation steps, the wave function of the interacting pair ($|1_C 1_T\rangle$) is given by

$$|\Psi_{t_0}\rangle = \sum_{i1,i2} f_{i1} e^{-i\boldsymbol{k}_{10}.\boldsymbol{x}_{i1}} \hat{\sigma}^{i1}_{r_1 g} f_{i2} e^{-i\boldsymbol{k}_{20}.\boldsymbol{x}_{i2}} \hat{\sigma}^{i2}_{r_2 g} |G\rangle, \tag{6.2}$$

where $|G\rangle = \otimes_{i=1}^{N} |g\rangle^i$ is the collective ground state and $\boldsymbol{k_{10}}$ and $\boldsymbol{k_{20}}$ are the central wave vectors of the collective excitations. The summation in Eq. 6.2 is over all atoms inside the

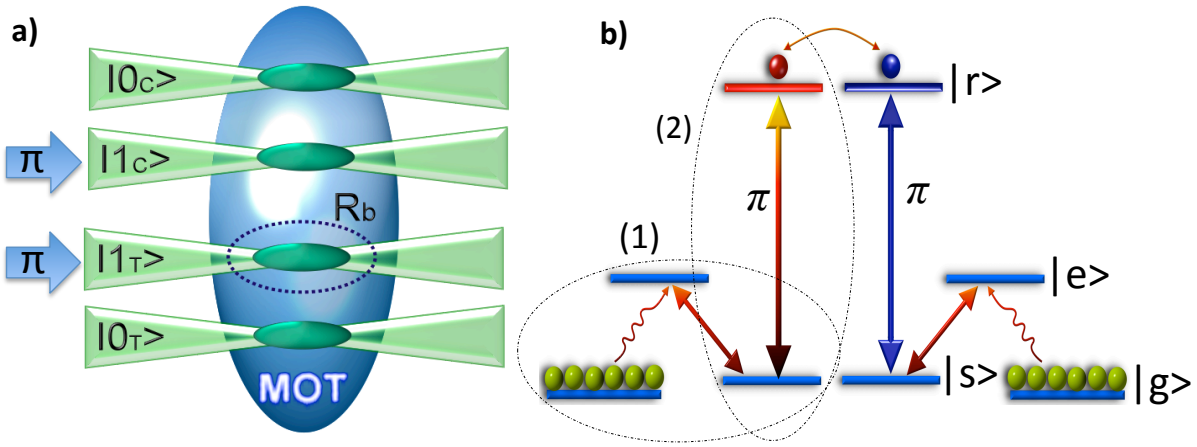

Figure 6.1: (Color online) Proposed photon-photon gate scheme. (a) Setup. The scheme is based on dual rail qubits [186]. All four rails are stored as collective spin excitations in an atomic ensemble in a magneto-optical trap (MOT). Only the interacting rails ($|1\rangle_C$ and $|1\rangle_T$) are excited to Rydberg levels. The separation between the interacting rails is set to be larger than the blockade radius R_b to ensure that both collective excitations can be promoted to the Rydberg level. (b) Level scheme. The photons are stored and retrieved through non-Rydberg EIT (dashed circle #1), which completely separates the Rydberg interaction from the storage and retrieval process. Subsequently optical π pulses promote the collective excitations in the interacting rails to Rydberg states (dashed circle #2), where the van der Waals interaction creates a cumulative conditional phase. After the interaction time, the photons are retrieved by another pair of π pulses followed by non-Rydberg EIT readout.

medium. The raising operator $\hat{\sigma}^i_{r_j g} = |r_j\rangle^i\langle g|$ excites the i-th atom to the Rydberg state $|r_j\rangle$ ($j = 1, 2$). The spatial profile of the collective excitations is considered in f_i. Their shape is determined through the storage process and the shape of the input pulses. We assume a Gaussian profile for the rest of this chapter.

The interaction energy between two Rydberg atoms has the form $\triangle(\boldsymbol{x}) = \frac{c_n}{|\boldsymbol{x}|^n}$, where $\boldsymbol{x}$ is the separation between the atoms. It changes from dipole-dipole ($n = 3$) in the short range to van der Waals ($n = 6$) in the long range, see Sec. 5.8. The spatial separation of the collective excitations in our protocol is in the range of the van der Waals interaction. The many-body interaction Hamiltonian is

$$\hat{H}_{int} = \sum_{l1,l2} \hat{\sigma}^{(l1)}_{r_1 r_1} \triangle(\boldsymbol{x}_{l1} - \boldsymbol{x}_{l2}) \hat{\sigma}^{(l2)}_{r_2 r_2}, \tag{6.3}$$

where $\hat{\sigma}_{rr}$ is the projection operator. Different combinations of excited atoms in Eq. 6.2 gain different phases, because their interaction strength is distance-dependent. This leads to a non-uniform distribution of conditional phase over each collective excitation, which affects the gate fidelity.

6.3 Effects of Non-Uniform Interaction

In order to gain some insight into the dynamics of our system, we begin by deriving approximate analytic expressions for the effects of the non-uniform interaction. The modulus squared of the two-excitation wave function (of interacting rails) in momentum space, $|\Psi_{k_1,k_2}(t)|^2$, is given by

$$\left| \sum_{i1,i2} f_{i1} e^{-i\boldsymbol{K}_1.\boldsymbol{x}_{i1}} f_{i2} e^{-i\boldsymbol{K}_2.\boldsymbol{x}_{i2}} e^{\frac{-ic_6 t}{|\boldsymbol{x}_{i1} - \boldsymbol{x}_{i2}|^6}} \right|^2, \tag{6.4}$$

where $\boldsymbol{K}_j = \boldsymbol{k}_j - \boldsymbol{k}_{j0}$ for $j = 1$ ($j = 2$) is the wave vector of the first (second) collective excitation relative to its central mode. When the collective excitations are far separated compared to their width, the interaction can be expanded to the second order in the relative

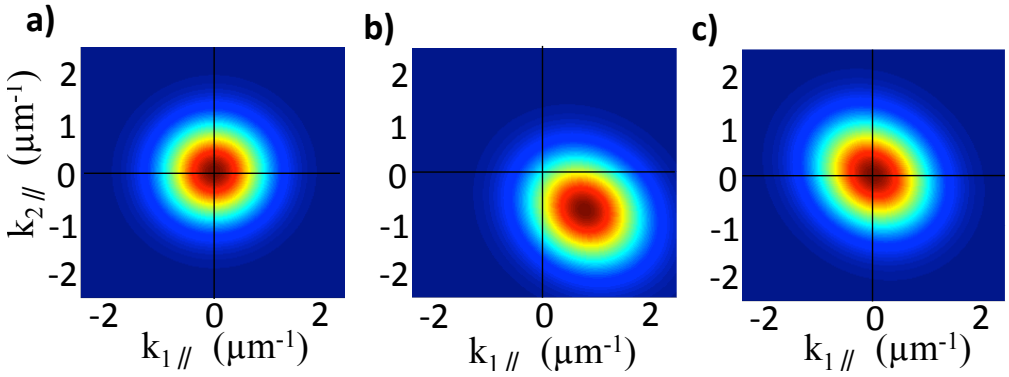

Figure 6.2: (Color online) Two-excitation wave function in momentum space. Numerical evaluation of $|\psi_{k_{1_{||}},k_{2_{||}}}|^2$, for the momentum components $k_{1_{||}}$ and $k_{2_{||}}$ which are parallel to the separation between the collective excitations. (a) Before the interaction the two-excitation wave function is a product of two individual Gaussian distributions. (b) After the interaction the center of the distribution is displaced and its cross section becomes elliptic. The momentum displacement is created by the linear term of the interaction when expanded in terms of relative distance, see Eq. (6.5). The elliptic shape is caused by the quadratic term in Eq. (6.5) and represents unwanted entanglement between the two excitations. (c) The displacement in momentum space can be compensated by a swapping protocol, see Fig. 6.3 and below.

distance,

$$\frac{1}{|\boldsymbol{x}_{i1}-\boldsymbol{x}_{i2}|^6}=\frac{1}{|\Delta\boldsymbol{x}_0|^6}-\frac{6(\boldsymbol{X}_{i1}-\boldsymbol{X}_{i2}).\Delta\boldsymbol{x}_0}{|\Delta\boldsymbol{x}_0|^8} \\ -\frac{3\,|\boldsymbol{X}_{i1}-\boldsymbol{X}_{i2}|^2}{|\Delta\boldsymbol{x}_0|^8}+\frac{24(\Delta\boldsymbol{x}_0.(\boldsymbol{X}_{i1}-\boldsymbol{X}_{i2}))^2}{|\Delta\boldsymbol{x}_0|^{10}}+O(3), \tag{6.5}$$

where $\Delta\boldsymbol{x}_0=\boldsymbol{x}_{10}-\boldsymbol{x}_{20}$ is the distance between the center of the two Gaussian collective excitations and $\boldsymbol{X}_{i1}=\boldsymbol{x}_{i1}-\boldsymbol{x}_{10}$ indicates the relative position of an excited atom with respect to the center of its distribution. The first (zeroth-order) term in the expansion is uniform, i.e. it only depends on the distance between the centers of the two collective excitations, whereas the higher-order terms will give non-uniform contributions to the phase, i.e. contributions that depend on the distance between individual points.

The interaction can be separated into terms that are parallel and perpendicular with respect to the separation between the collective excitations $\Delta\boldsymbol{x}_0$, corresponding to the coordinates $(\hat{x}_{||},\hat{x}_{\perp})$ etc. One can correspondingly rewrite Eq. (6.4) in parallel and perpendicular

dimensions, resulting in

$$|\psi_{k_{1\shortparallel},k_{2\shortparallel}}|^2 \propto e^{\frac{-w_{\shortparallel}^2}{2(1+4S_{\shortparallel}^2)}\left[(K_{1\shortparallel}-k_D)^2+(K_{2\shortparallel}+k_D)^2+2S_{\shortparallel}^2(K_{1\shortparallel}+K_{2\shortparallel})^2\right]}$$
$$|\psi_{k_{1\perp},k_{2\perp}}|^2 \propto e^{\frac{-w_{\perp}^2}{2(1+4S_{\perp}^2)}\left[K_{1\perp}^2+K_{2\perp}^2+2S_{\perp}^2(K_{1\perp}+K_{2\perp})^2\right]}, \tag{6.6}$$

where $2w_{\shortparallel}$ ($2w_{\perp}$) is the spatial width of the collective excitation in the parallel (perpendicular) dimension. The momentum displacement $\boldsymbol{k_D} = \frac{6c_6t}{|\Delta \boldsymbol{x}_0|^8}\Delta \boldsymbol{x}_0$ is derived from the first order of the interaction expansion. The second order terms in the parallel and perpendicular dimensions give the coefficients $S_{\shortparallel} = \frac{21w_{\shortparallel}^2 c_6 t}{|\Delta \boldsymbol{x}_0|^8}$ and $S_{\perp} = \frac{3w_{\perp}^2 c_6 t}{|\Delta \boldsymbol{x}_0|^8}$ respectively.

We numerically evaluate Eq. (6.4) and show the results in Fig. 6.2(a,b) for the parallel dimension (see Fig. 6.5 for the perpendicular dimension). These calculations are for the case where two co-propagating photons in the interacting rails are stored with a separation of $21\mu m$ in an ensemble of ^{87}Rb atoms in a MOT with a density of $\rho = 4 \times 10^{12}$ cm^{-3}. Both collective excitations have the same spatial width $2w_{\shortparallel}(2w_{\perp}) = 3$ μm (8 μm), but they are excited to different Rydberg levels $|103\,S_{1/2}\rangle$ and $|102\,S_{1/2}\rangle$ using local control fields [187]. Different principal numbers are considered for the two excitations in order to create a stronger interaction [188, 189]. The interaction time is 0.2 μs.

6.3.1 Momentum Displacement

The numerical results correspond well to the expectations based on the approximate analytic treatment above. Fig. 6.2(b) clearly shows the expected displacement in momentum space, where the momentum shift $\boldsymbol{k}_D$ gained by the two collective excitations (in opposite direction and parallel to the separation) can be understood as being due to the action of the Rydberg force $\boldsymbol{F}_{Ryd} = -\nabla U_{int}$ over the interaction time. In practice, this will result in retrieval of the photons in directions that deviate from the naively expected phase matching direction, see also Sec. 6.8. This "frozen collision" is a remarkable effect in the sense that the change of momentum due to the interaction only becomes apparent once the photons are read out. Based on the geometry of the valence orbital of excited atoms (which determines the sign of

c_6), the collision can be either attractive or repulsive [190, 191].

6.3.2 Unwanted Entanglement

Fig. 6.2(b) also shows the effect of the second-order term. which creates unwanted entanglement between $|1\rangle_C$ and $|1\rangle_T$ (as well as spreading in momentum space). The cross terms in the exponents in Eq. (4) create correlations between the two collective excitations. Correspondingly the circular cross section of the profile of the probability distribution in momentum space becomes a 45^o rotated ellipse, see also Fig. 6.5(b). These cross terms are proportional to

$$\begin{aligned} e_{\shortparallel}^2 &= \frac{4S_{\shortparallel}^2}{1+4S_{\shortparallel}^2} \\ e_{\perp}^2 &= \frac{4S_{\perp}^2}{1+4S_{\perp}^2}, \end{aligned} \tag{6.7}$$

where $e_{\shortparallel}$ and $e_{\perp}$ are the eccentricities of the elliptic cross sections in the parallel and perpendicular dimension respectively.

6.4 Gate Performance

We analyze the expected gate performance using the concepts of (conditional) fidelity and efficiency. Analogous concepts are commonly used in the context of quantum storage [192]. The conditional fidelity quantifies the performance of the gate, conditioned on successful retrieval of both photons. The effects of photon loss are discussed in terms of efficiency below. Following the treatment in [185], the conditional fidelity of a gate operating on the initial state

$$|\phi\rangle = \frac{1}{2}\left(|0_C\rangle + |1_C\rangle\right)\left(|0_T\rangle + |1_T\rangle\right) \tag{6.8}$$

can be quantified as

$$F = \sqrt{\langle\phi'|\,\rho\,|\phi'\rangle}. \tag{6.9}$$

This definition characterizes the gate's outcome ρ, relative to the ideal output

$$|\phi'\rangle = (|00\rangle + |01\rangle + |10\rangle - |11\rangle)/2. \tag{6.10}$$

Since the many-body interaction only affects the interacting pair, the fidelity can be rewritten as

$$F = \sqrt{(9 - 3(\zeta + \zeta^*) + |\zeta|^2)/16} \tag{6.11}$$

where

$$\zeta = \langle \Psi_{t_0} | \, e^{-i\hat{H}_{int}t} \, |\Psi_{t_0}\rangle \tag{6.12}$$

with $|\Psi_{t_0}\rangle$ as given in Eq. (6.2) and $\hat{H}_{int}$ as defined above. It is clear from Fig. 6.2(b) that the momentum displacement and the entanglement-related profile deformation will affect the value of ζ and hence of F. Controlling these effects is essential for achieving high gate fidelity.

6.4.1 Swapping Protocol (Compensating the Momentum Displacement)

We propose a swapping protocol to compensate the destructive effects of the momentum displacement, see Fig. 6.3. The distance-dependent nature of the interaction, and in particular the first-order term in Eq. (6.5), creates a spatial phase gradient along the dimension parallel to $\Delta\mathbf{x_0}$. Swapping the relative position of the collective excitations after half the interaction time corresponds to switching the sign of $\Delta\mathbf{x_0}$, which leads to a cancellation of this unwanted gradient after the total interaction time. More details about the swapping protocol can be found in Figure 6.3 and 6.8. The compensation of the momentum displacement after swapping can be seen in Fig. 6.2(c), which is based on an exact numerical calculation, and its beneficial effect on the gate fidelity in Fig. 6.3(d). The swapping protocol is relatively robust to positioning errors. In an example where the collective excitations are separated by 21 μm, an averaged Gaussian error of 1 μm in the parallel dimension reduces the average fidelity by 1%, as illustrated in figure 6.6. Errors in the perpendicular dimension are much less critical (see figure 6.6).

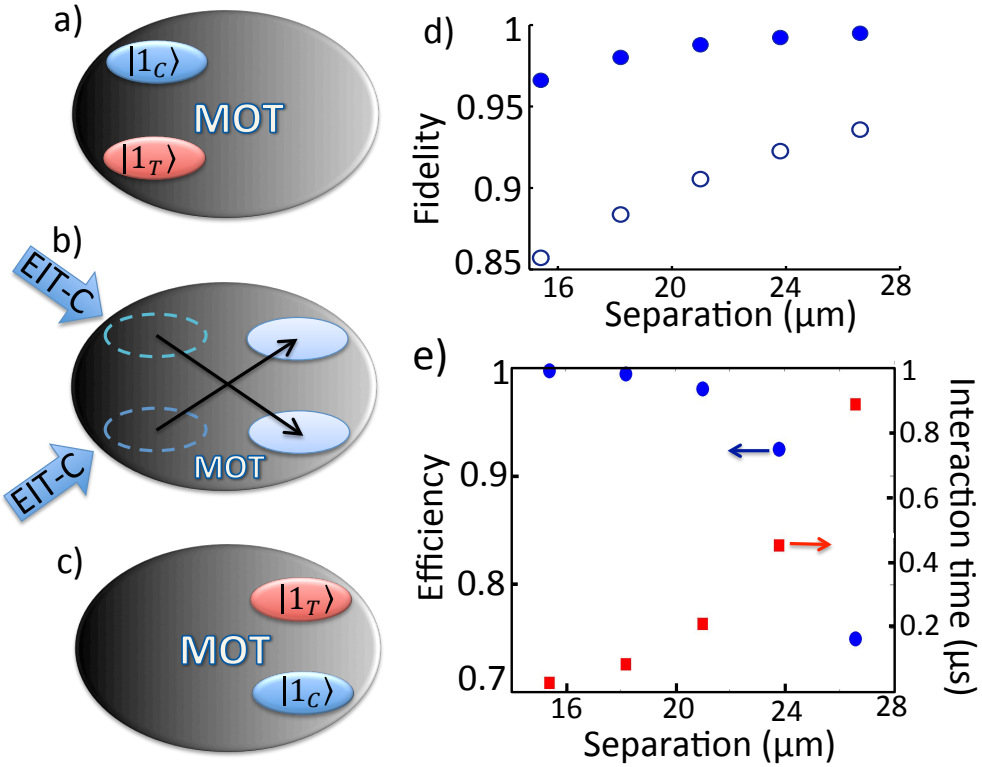

Figure 6.3: (Color online) Swapping protocol to compensate the momentum displacement shown in Fig. SiKy(b) and resulting gate performance. (a) Photons in the interacting rails (1_C, 1_T) are stored as collective excitations and excited to the Rydberg levels $|r\rangle$ as described in Fig. 6.1. They are brought back to the spin state $|s\rangle$ after half of the interaction time ($\frac{t}{2}$). (b) Tilted control fields swap the relative positions of the two collective excitations using non-Rydberg EIT (See circle #1-Fig. 6.1). Note that during the swapping the collective excitations propagate along the direction of the tilted control fields, see Sec. 6.9. (c) The collective excitations are re-excited to the Rydberg levels, interact for $\frac{t}{2}$, and are de-excited again. The photons are retrieved using non Rydberg EIT. A more detailed description of the swapping protocol including a timing diagram is illustrated in figure 6.8. (d) Gate fidelity as a function of the separation between the collective excitations. Solid and hollow circles are with and without the swapping protocol respectively. The spatial shape of the collective excitations is the same as in Fig. 6.2. (e) Gate efficiency (circles) and interaction time required for creating a π phase shift (squares) as a function of the separation. The efficiency does not include photon storage and retrieval, see text. One sees that increasing the separation yields higher fidelity, but lower efficiency, because the weaker interaction for greater separations requires longer interaction times and hence more loss due to thermal motion and the finite lifetime of the Rydberg states. Using the swapping protocol, both high fidelity and high efficiency can be achieved.

6.4.2 Sources of Decoherence

It is important to also consider photon loss. Photon loss that is uniform over the four rails has no effect on the conditional fidelity as defined above. It can therefore be discussed independently in terms of the efficiency η, which is the probability of retrieving each photon after the gate operation. Non-uniform loss terms in our scheme can be made uniform by adding external sources of loss to certain rails, see section 6.10.3. Three important sources of loss are atomic thermal motion (see Sec. 6.10.1), the finite lifetime of the Rydberg levels (200 μs [194]), and the loss due to decay from the intermediate state during the two-photon excitation to the Rydberg states, see Sec. 6.10.2. Their effects on the efficiency are shown in Fig. 6.3(e) for different interaction times in an ensemble cooled to T=150 μK. The efficiency can be improved by additional cooling using optical molasses. Considering the separation of interacting rails, there is a trade-off between fidelity and efficiency. A small separation improves the efficiency by reducing the interaction time (see Fig. 6.3(e)), but the resulting stronger interaction causes more entanglement and momentum displacement, which reduces the fidelity (see Fig. 6.3(d)). The swapping protocol makes it possible to achieve high fidelity and high efficiency simultaneously. Taking both efficiency and fidelity into account, the optimum separation for our example can be seen to be around 21 μm.

6.4.3 Storage inefficiency

Another significant source of inefficiency comes from the process of storage and retrieval of single photons. A conservative estimate of the associated efficiency for the whole protocol (including the swapping) can be obtained by applying the photon's storage and retrieval efficiency twice [195]. This corresponds to the use of two separate MOTs for storing photons before and after swapping. Based on this estimate the overall efficiency for a density of $\rho = 4 \times 10^{12}$ cm^{-3} (corresponding to an optical depth $d \approx 100$) is about 70%. In practice using a single MOT is likely to both be more practical and lead to higher efficiency than

these estimates because in this case the stationary excitations only have to be converted into moving excitations (but not all the way into photons) at the intermediate stage. Increasing the density to $\rho = 3.8 \times 10^{13}$ cm^{-3} ($d \approx 750$) (which is achievable in a BEC) improves the efficiency of repeated storage and retrieval to 95%.

6.4.4 Controling the Unwanted Entanglement

We have shown how to compensate the effect of momentum displacement on the fidelity. The other destructive effect of the interaction that reduces the fidelity is the creation of unwanted entanglement between the collective excitations. Entanglement reduces the fidelity by deforming the two-excitation wave function in momentum space, see Fig. 6.2(b) (see also figure 6.5(b)). Comparing the eccentricities of the ellipses in parallel and perpendicular direction obtained from Eq. (6.6),

$$\frac{e_{\shortparallel}^2}{e_{\perp}^2} \backsim \frac{49 w_{\shortparallel}^4}{w_{\perp}^4}, \tag{6.13}$$

one sees that the deformation is much stronger for the parallel dimension. Therefore, compression of the collective excitations parallel to their separation can reduce the unwanted entanglement while leaving room for extra atoms in the perpendicular dimensions in order to preserve the directionality of the collective emission [196, 197]. The highly non-isotropic effects of profile compression on the fidelity are shown in Fig. 6.4(a). The achievable width compression is mainly limited by diffraction. In order to show the relation between fidelity and entanglement even more clearly we calculate the Von Neumann entropy of the output state. Fig. 6.4(b) shows that after compensating the momentum displacement, entanglement remains as the only significant source of infidelity [198].

6.5 Conclusion and Outlook

In conclusion, we have proposed a photon-photon gate protocol that uses stationary collective Rydberg excitations, but does not rely on photon blockade. We have shown that unwanted

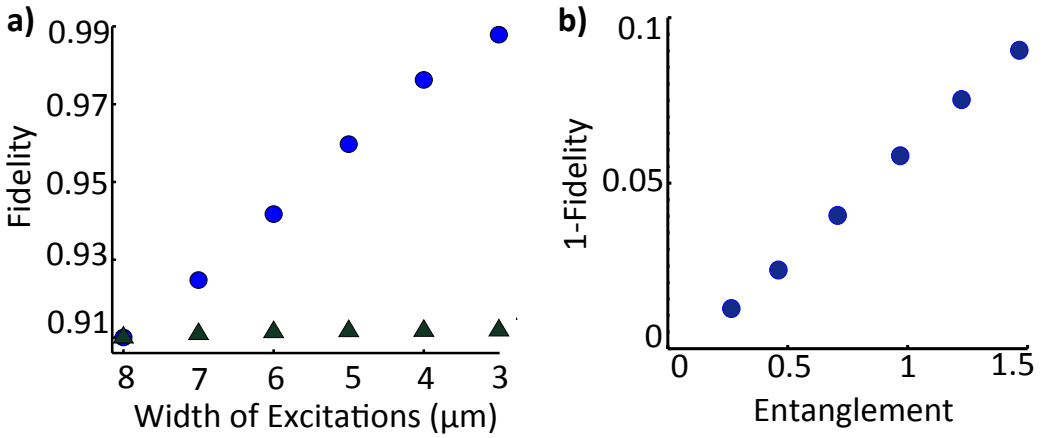

Figure 6.4: (Color online) Effects of unwanted entanglement on gate fidelity. (a) The fidelity has a non-isotropic dependence on the width of the collective excitations. Here the collective excitations are separated by 21 μm and their spatial profile has the same initial width of 8 μm in all directions. Compressing the width parallel to the separation ($w_{\shortparallel}$) has a significant impact on the fidelity (circles). In contrast, compressing the width perpendicular to the separation ($w_{\perp}$) has a negligible effect (triangles). (b) The fidelity reduction $1 - F$ is proportional to the entanglement, quantified by the Von Neumann entropy. Here the momentum displacement is compensated by the swapping protocol of Fig. 6.3, leaving the unwanted entanglement as the main source of infidelity.

effects due to the distance-dependence of the interaction are important but can be overcome, making it realistic to achieve a gate operation with high fidelity and efficiency. These effects may also be useful for the implementation of photonic transistors using Rydberg states [199].

6.6 Appendix A1: Effects of Interaction on the wave function in the perpendicular dimensions

Fig. 6.5 shows the numerical evaluation of $|\psi_{k_{1\perp},k_{2\perp}}|^2$, the modulus squared of the two-excitation wave function in the dimensions perpendicular to the separation. While the second order of the interaction changes the Gaussian cross section from circular to elliptical by entangling the two excitations, the first order does not have any effect in this dimension.

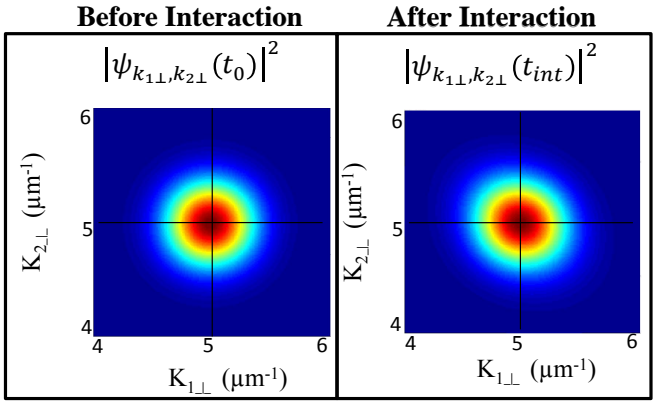

Figure 6.5: Numerical results for $|\psi_{k_{1\perp},k_{2\perp}}|^2$. There is no momentum displacement in this dimension. The parameters are the same as in the main text.

6.7 Appendix A2: Sensitivity of Fidelity to positioning errors in Swapping

Fig. 6.6 shows that the swapping protocol is more sensitive to positioning errors for the collective excitations in the parallel dimension than in the perpendicular dimension.

6.8 Appendix A3:"Frozen Collision"

Fig. 6.7 shows the redistribution of the momentum vectors of the collective excitations due to the interaction. One sees that collective excitations that are created by the storage of co-propagating photons will yield diverging photons upon retrieval.

6.9 Appendix A4: Swapping protocol

The detailed steps of the swapping protocol are shown in Fig. 6.8. The spatial propagation of the collective excitations is done using non-Rydberg EIT, for which the level structure is explained in Fig. 6.1b-Circle 1. The interaction is turned on and off using π pulses (Fig. 6.1b-Circle 2). The timing diagram in Fig. 6.8f represents the order of pulses required for the gate operation. During the swapping, phase matching ensures that the collective excitations propagate along the direction of the tilted control fields. (The wave vector of the stored collective excitations, which is given by the difference between the wave vector of the single

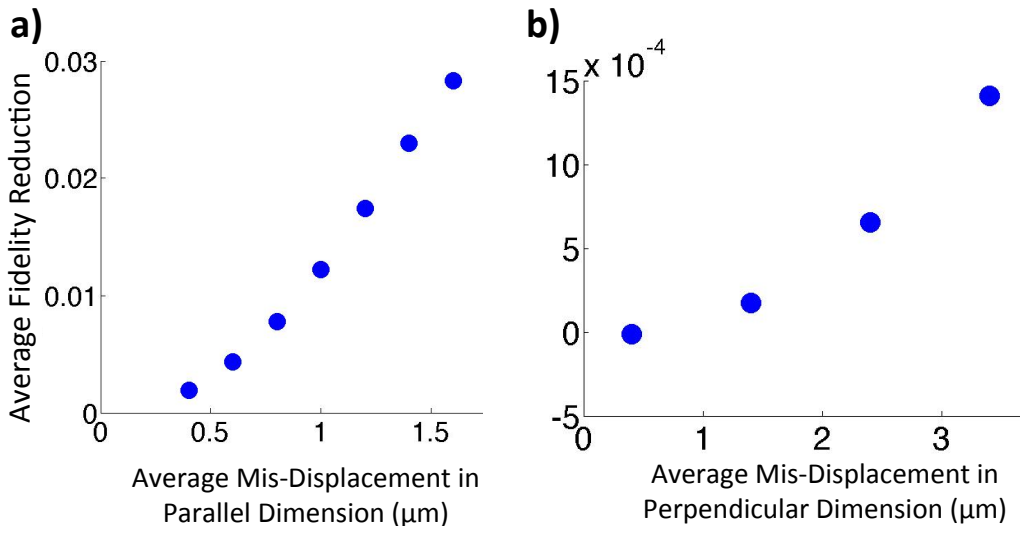

Figure 6.6: Average fidelity reduction as a function of positioning error for the swapping protocol in (a) parallel and (b) perpendicular dimension. The parameters are the same as for Fig. 6.2.

photon and that of the control field used for storage, is much smaller than that of the tilted control field.)

6.10 Appendix A5: Gate Efficiency

6.10.1 Thermal motion

The efficiency factor due to the thermal motion of the atoms (in the absence of all trapping fields) is given by [200]

$$\eta_{th} = \frac{1}{(1+(\frac{t}{\xi})^2)^2} exp[\frac{-t^2/\tau^2}{(1+(t/\xi)^2)}], \tag{6.14}$$

where $\tau = \frac{\Lambda}{2\pi v}$ is the dephasing time scale, which is determined by the wave length Λ of the collective excitations and the thermal speed v, and $\xi = \frac{w}{v}$ is the time scale on which an atom traverses the width w of a collective excitation.

For a two-photon excitation by counter-propagating laser beams at 780 and 480 nm, the recoil speed is 0.35cm/s. This velocity is comparable to the atomic thermal velocity at BEC temperature, but has negligible effect in a MOT. For completeness we have included this effect in our calculation of the gate efficiency.

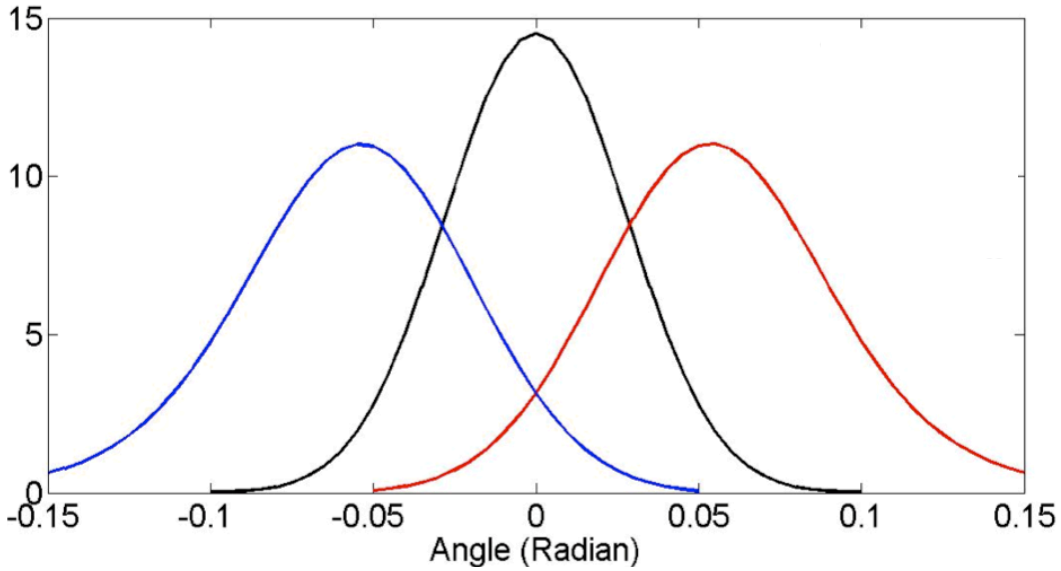

Figure 6.7: Angular distribution of the momenta of two photons in the interacting rails before (black for both) and after (red and blue) the gate operation. The parameters are the same as for Fig. 6.2.

6.10.2 Loss Via the Intermediate State

The coherent excitation of the collective spin excitations to Rydberg states requires a two-photon excitation using red ($\Omega_1 : 5S \rightarrow 5P$) and blue ($\Omega_2 : 5P \rightarrow 102S$) control fields. To avoid populating the short-lived intermediate $5P$ state (which has a lifetime τ=26 ns), the control fields have to be detuned from that state by Δ. Using equal Rabi frequencies for both transitions ($\Omega_1 = \Omega_2$) one can minimize both the excitation time and the loss from the intermediate state [201]. The transition dipole moment in Ω_2 is 1500 times weaker than in Ω_1, requiring a relatively strong blue laser. For a detuning Δ=5.5 GHz, and $\Omega_1 = \Omega_2 = 1$ GHz, an excitation time of t_{exc}=3 ns can be achieved, which results in a loss of only 0.29%. For a control field waist of 11 μm, this value of Ω_2 corresponds to a pulse energy of 1.2 μJ. In Ref. [202] the authors used a dye amplifier laser with significantly higher energy per pulse (55 μJ at 480 nm).

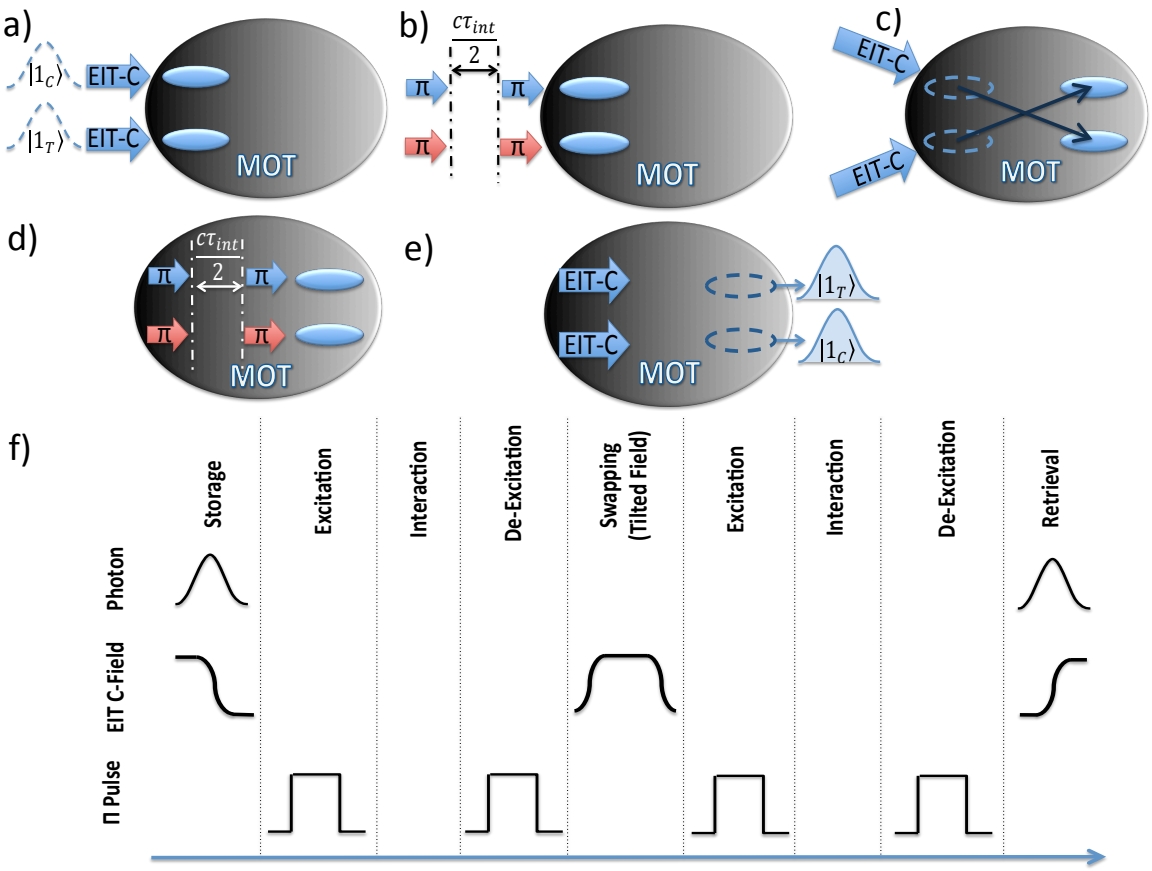

Figure 6.8: Detailed steps of the swapping protocol and timing diagram. Photons in the interacting rails (1C, 1T) are stored in (a) and retrieved from (e) collective spin excitations through non-Rydberg EIT. c) Tilted control fields swap the collective excitations after half the interaction time across the direction of their separation using non-Rydberg EIT. (b,d) Two consecutive π pulses excite and de-excite collective spin excitations to and from the Rydberg level and let them interact for half of the interaction time before (b) and after (d) swapping. (f) Timing diagram of all the pulses and operation steps for each of the interacting rails.

6.10.3 Uniform Loss

Photon loss that is uniform over the four rails has no effect on the conditional fidelity and can be quantified independently in terms of the efficiency. Since only the interacting rails ($|1_C\rangle, |1_T\rangle$) are excited to Rydberg levels, they experience an extra loss due to the life time of the Rydberg level. Furthermore, the shorter wavelength of the Rydberg excitations in the interacting rails creates a stronger loss due to the atomic thermal motion compared to the non-interacting rails. Finally, the extra process of storage and retrieval during the

swapping of the interacting rails causes an extra loss of efficiency in these rails. The loss can be made uniform by adding a controlled external source of loss on the non-interacting rails ($|0_C\rangle, |0_T\rangle$), e.g. using crossed polarizers with an adjustable relative angle.

Chapter 7

Large Energy Superpositions via Rydberg Dressing

7.1 Preface

This Chapter proposes a scheme to create superposition states of over 100 Strontium atoms being in a ground state or metastable optical clock state, using the Kerr-type interaction due to Rydberg state dressing in an optical lattice. The two components of the superposition can differ by of order 300 eV in energy, allowing tests of energy decoherence models with greatly improved sensitivity. We take into account the effects of higher-order nonlinearities, spatial inhomogeneity of the interaction, decay from the Rydberg state, and diminishing Rydberg level separation for increasing principal number.

This work has been published in collaboration with other co-authors. Other than the effects of higher order non-linearities calculated by H. W. Lau the entire paper is the outcome of my research. I also wrote the manuscript with guidance from Prof. Simon. In addition I co-supervised an undergraduate student A. Humeniuk, who was helping at the early stage of the project in understanding of Rydberg dressing.

7.2 Introduction

There are currently many efforts towards demonstrating fundamental quantum effects such as superposition and entanglement in macroscopic systems [203, 204, 205, 206, 207, 208, 209, 210, 211, 212, 213, 214, 215, 216, 217, 218]. One relevant class of quantum states are so-called cat states, i.e. superposition states involving two components that are very different in some physical observable, such as position, phase or spin. Here we propose a method for creating such large superpositions in energy. This is relevant in the context of testing

proposed quantum-gravity related energy decoherence [219, 220, 221].

Our method relies on the uniform Kerr-type interaction that can be generated between atoms by weak dressing with a Rydberg state [222, 144, 223]. This can be used to generate cat states similarly to the optical proposal of Ref. [224]. Using an optical clock state in Strontium as one of the two atomic basis states makes it possible to create large and long-lived energy superposition states. The superposition can be verified by observing a characteristic revival. We analyze the effects of relevant imperfections including higher-order nonlinearities, spatial inhomogeneity of the interaction, decay from the Rydberg state, atomic motion in the optical lattice, collective many-body decoherence triggered by black-body induced transitions, molecular formation, and diminishing Rydberg level separation for increasing principal number. Our scheme significantly improves the precision of energy decoherence detection.

Previous related, but distinct, work includes Ref. [225] who briefly discussed the creation of energy superposition states in Strontium Bose-Einstein condensates based on collisional interactions. Ref. [226] proposed the creation of energy superposition states of light, and ref. [227] reported the realization of 14-ion GHZ state, with 24 eV energy separation, but without mentioning the energy superposition aspect. The present proposal promises much greater sensitivity to energy decoherence thanks to a much longer lifetime (compared to Ref. [226]) and to both increased size and longer lifetime (compared to Ref. [227]). Related work involving Rydberg states includes Refs. [228, 229], who performed detailed studies of the creation of moderate-size cat states using Rydberg blockade. The number of atoms is limited to of order ten in these schemes due to competing requirements for the presence and absence of blockade between different Rydberg transitions in the same ensemble. They also don't use metastable optical clock states, resulting in only small differences in energy between the two components. Ref. [230] briefly discussed the creation of moderate-size (15 atoms) GHZ type states in Strontium atom chains, without mentioning the energy superposition aspect. Ref.

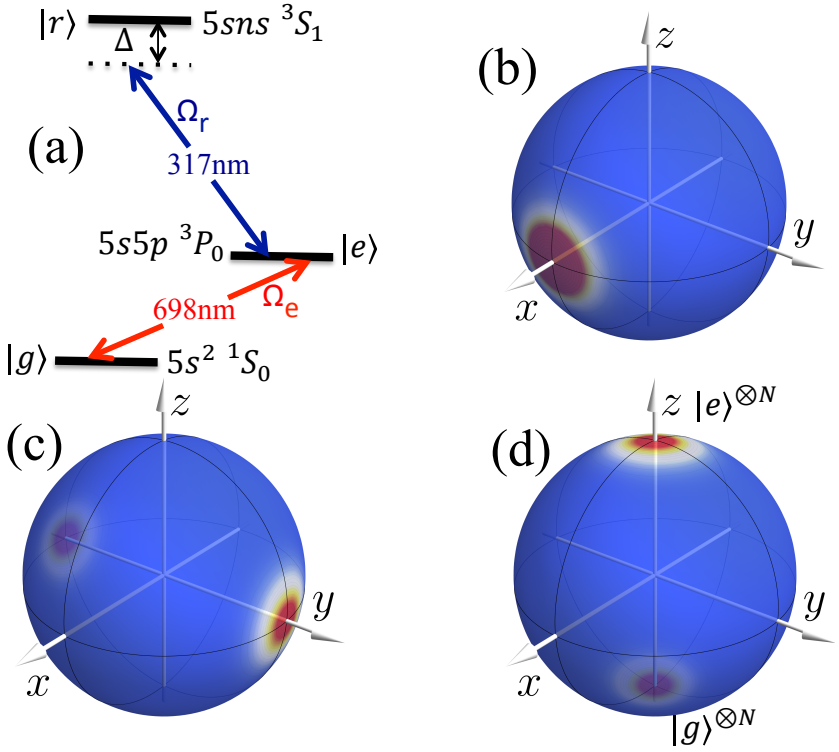

Figure 7.1: (Color online) Proposed scheme for creation of large energy superposition. (a) Level scheme in Strontium. The pseudo-spin states are the singlet ground state $|g\rangle$ and a long lived excited triplet state $|e\rangle$. An off-resonant laser field (Ω_r) dresses the excited state with the Rydberg level $|r\rangle$. This creates a Kerr-type interaction between the atoms in the excited state. The resonant laser field (Ω_e) is applied for population rotation. (b-d) The evolution of the Husimi distribution of the collective spin state on the Bloch sphere. Application of the Kerr-type interaction splits the initial coherent spin state (CSS) (b) into a superposition of two CSS at opposite poles of the Bloch sphere (c). Applying a $\pi/2$ rotation along the x axis following the cat creation process results in a superposition of all atoms being in the ground or excited state.

[230] uses attractive Rydberg interactions, but not the uniform Kerr-type interaction used in the present work. The number of atoms in Ref. [230] is limited by unwanted transitions to other nearby many-body states [231].

The paper is organized as follows. We begin with a description of our scheme in Sec. 7.3. In Sec. 7.4 and 7.5 we quantify the effects of the main imperfections and decoherence sources on the fidelity of final cat state. In Sec. 7.6 we find an estimate for size of cat states that can be realized with high fidelity. We then show that our scheme is experimentally realizable in Sec. 7.7, followed by a detailed discussion in Sec. 7.8, demonstrating that the effects of atomic motion, molecular formation, collective many-body decoherence, level mixing and BBR radiation induced decoherence can be suppressed. We conclude the paper in Sec. 7.9 with a discussion of the application of energy superposition states for the detection of energy decoherence.

7.3 Scheme

We now describe our proposal in more detail. In an ensemble of N ultra-cold Strontium atoms trapped in a 3D optical lattice [232], one can consider a two-level system consisting of the singlet ground state $|g\rangle$ and a long-lived excited triplet state $|e\rangle$, which are separated in energy by 1.8 eV. An interaction between the atoms can be induced by dressing the clock state with a strongly interacting Rydberg level [222, 144, 223] as shown in the level scheme of Fig. 7.1. This induces a light shift (LS) on the atoms which depends on the Rydberg blockade.

7.3.1 Kerr-type Rydberg Dressed Interaction

When the entire ensemble is inside the blockade radius, the dressing laser couples the state with no Rydberg excitation $|\psi_1\rangle = \otimes_i |\phi_i\rangle$ (where $\phi \in \{e, g\}$) to a state where only one of the atoms in the $|e\rangle$ level gets excited to the Rydberg level $|\psi_2\rangle = \sum_i |\phi_1 ... r_i ... \phi_N\rangle$ with an

enhanced Rabi frequency $\sqrt{N_e}\Omega_r$ [233](see Sec. 5.9), where N_e is the number of atoms in the excited state. Over the Rydberg dressing process, the Hamiltonian can be diagonalized instantaneously

$$D \equiv UHU^{\dagger} = \begin{pmatrix} E_- & 0 \\ 0 & E_+ \end{pmatrix}, \tag{7.1}$$

where $E_{\pm} = \frac{\Delta}{2}(1 \pm \sqrt{1 + \frac{N_e\Omega_r^2}{\Delta^2}})$ and

$$U = \begin{pmatrix} \cos(\theta/2) & -\sin(\theta/2) \\ \sin(\theta/2) & \cos(\theta/2) \end{pmatrix} \tag{7.2}$$

with $\theta = \tan^{-1}(\frac{\sqrt{N_e}\Omega_r}{\Delta})$. The Schrödinger equation expressed in the dressed state basis $|\varphi> = U|\psi>$ is

$$i\frac{\partial}{\partial t}\begin{pmatrix} |\varphi_-\rangle \\ |\varphi_+\rangle \end{pmatrix} = \begin{pmatrix} E_- & -i\dot{\theta}/2 \\ i\dot{\theta}/2 & E_+ \end{pmatrix}\begin{pmatrix} |\varphi_-\rangle \\ |\varphi_+\rangle \end{pmatrix}. \tag{7.3}$$

To avoid the scattering of population from the ground dressed state to the excited dressed state, the coupling term $\dot{\theta} = \frac{\sqrt{N_e}\Omega_r\dot{\Delta} - \sqrt{N_e}\Delta\dot{\Omega}_r}{N_e\Omega_r^2 + \Delta^2}$ should be smaller than E_+ (see realization section 7.7 for examples).

Focusing on the ground dressed state, the effective light shift of the system is

$$E_- = \frac{\Delta}{2}(1 - \sqrt{1 + \frac{N_e\Omega_r^2}{\Delta^2}}). \tag{7.4}$$

Within the weak dressing regime ($\frac{\sqrt{N_e}\Omega_r}{\Delta} \ll 1$) one can Taylor expand the light shift to

$$E_- = \frac{\Delta}{2}[1 - (1 + \frac{1}{2}\frac{N_e\Omega_r^2}{\Delta^2} - \frac{1}{8}\frac{N_e^2\Omega_r^4}{\Delta^4} + O(\frac{N_e\Omega_r^2}{\Delta^2})^3)], \tag{7.5}$$

which can be simplified to $E_- \approx (N_e^2 - \frac{N_e}{w^2})\frac{\chi_0}{2}$, with $w = \frac{\Omega_r}{2\Delta}$ and $\chi_0 = 2w^4\Delta$. Therefore adiabatic weak dressing of atoms to the Rydberg level imposes an effective Kerr-type Hamiltonian

$$H = (\hat{N_e}^2 - \frac{\hat{N_e}}{w^2})\frac{\chi_0}{2} \tag{7.6}$$

on the atoms within the blockade radius. The effects of higher order terms in the Taylor expansion are discussed in Sec. 7.4.1 and Fig. 7.2.

7.3.2 Generation of Cat State on the Equator of the Bloch Sphere

The two levels $|g_i\rangle$ and $|e_i\rangle$ for each atom are equivalent to a spin 1/2 system with Pauli matrices $\sigma_x^{(i)} = (|g_i\rangle\langle e_i| + |e_i\rangle\langle g_i|)/2$, $\sigma_y^{(i)} = i(|g_i\rangle\langle e_i| - |e_i\rangle\langle g_i|)/2$ and $\sigma_z^{(i)} = (|e_i\rangle\langle e_i| - |g_i\rangle\langle g_i|)/2$ acting on the atom at site i. We define collective spin operators $S_l = \sum_{i=1}^{N} \sigma_l^{(i)}$. A coherent spin state (CSS) is defined as a direct product of single spin states [234]

$$|\theta, \phi\rangle = \otimes_{i=1}^{N} [\cos\theta |g\rangle_i + \sin\theta e^{i\phi} |e\rangle_i], \tag{7.7}$$

where all the spins are pointing in the same direction, and ϕ and θ are the angles on the (collective) Bloch sphere. The CSS can also be represented as [234]

$$|\eta\rangle = |\theta, \phi\rangle = (1 + |\eta|^2)^{-N/2} \sum_{N_e=0}^{N} \eta^{N_e} \sqrt{C(N, N_e)} |N; N_e\rangle, \tag{7.8}$$

where $\eta = \tan(\theta/2) e^{-i\phi}$, $C(N, N_e) \equiv \begin{pmatrix} N \\ N_e \end{pmatrix}$ and $|N; N_e\rangle = \frac{1}{\sqrt{C(N,N_e)}} \sum_{i1<i2<\ldots<iN_e}^{N} |g_1 \ldots e_{i1} \ldots e_{iN_e} \ldots g_N\rangle$ is the Dicke state of N_e excited atoms, where $|N; N_e\rangle$ is an alternative representation of the $|J\, M\rangle$ basis with $N = 2J$ and $N_e = J + M$.

Let us now discuss the time evolution of an initial CSS $|\eta\rangle$ under the Kerr-type interaction of Eq. (7.6). The state evolves as

$$|\psi(t)\rangle = (1 + |\eta|^2)^{-N/2} \sum_{N_e=0}^{N} \eta^{N_e} e^{-iHt} \sqrt{C(N, N_e)} |N; N_e\rangle. \tag{7.9}$$

At the "cat creation" time $\tau_c = \frac{\pi}{\chi_0}$ the linear term of Eq. 7.6 creates a phase rotation, which changes the state to $|\eta'\rangle = |e^{-i\frac{N_e \chi_0}{2w^2}\tau_c} \eta\rangle$. The quadratic term produces coefficients of (1) and $(-i)$ for even and odd N_e's respectively. The state can then be rewritten as a superposition of two CSS, namely

$$|\psi(\tau_c)\rangle = \frac{1}{\sqrt{2}} (e^{i\frac{\pi}{4}} |\eta'\rangle + e^{-i\frac{\pi}{4}} |-\eta'\rangle) \tag{7.10}$$

in analogy with Ref. [224]. Continuing the interaction for another τ_c, one can observe the revival of the initial CSS. This revival can be used as proof for the successful creation of a quantum superposition at τ_c, since a statistical mixture of CSS at τ_c would evolve into another mixture of separate peaks [218, 235].

7.3.3 Creating the Energy Cat

To create an energy superposition state we thus have to apply the following steps. Starting from the collective ground state $|g\rangle^{\otimes N}$, we apply a $\pi/2$ pulse on the $|e\rangle - |g\rangle$ transition that results in the maximum eigenstate of the S_x operator $|\eta = 1\rangle = (\frac{|e\rangle+|g\rangle}{\sqrt{2}})^{\otimes N}$, as shown in Fig. 7.1(b). Since the atoms are confined to the ground states of optical lattice traps, the position-dependent phase factors associated with laser excitation of the clock state are constant over the course of the experiment and can be absorbed into the definition of the atomic basis states (detailed discussion can be found in Sec. 7.8.1). We now apply the Kerr-type interaction. The large coefficient of the linear term in the Hamiltonian leads to a rotation of the created cat state on the equator of Bloch sphere. Applying accurate interaction timing, the state can be chosen to be a superposition of two CSS pointing to opposite directions along the y axis on the Bloch sphere $|\psi(\tau_c)\rangle = \frac{1}{\sqrt{2}}(e^{i\frac{\pi}{4}}|\eta = i\rangle + e^{-i\frac{\pi}{4}}|\eta = -i\rangle)$, see Fig. 7.1(c) and inset (a) of Fig. 7.2. For example, a timing precision of $\delta\tau_c = \frac{2w^2}{5\pi\sqrt{N}}\tau_c$ results in an adequate phase uncertainty of $\delta\phi = \frac{1}{5\sqrt{N}}$ (examples can be found in the realization Sec. 7.7). Applying another $\frac{\pi}{2}$ pulse on the created cat state results in $\frac{|e\rangle^{\otimes N}+|g\rangle^{\otimes N}}{\sqrt{2}}$, which is a superposition of all the atoms being in the ground and excited states, as shown in Fig. 7.1(d). The created state is a superposition of two components with very different energies. To verify the creation of the energy cat state one needs to rotate the state back to the equator and detect the revival of the initial CSS under the Kerr-type interaction, see also the inset of Fig. 7.2(b).

7.4 Imperfections

In this section we quantify the effects of the most important imperfections with direct impact on the achievable cat size. Other sources of imperfections, which can be made to have relatively benign effects on our scheme, are discussed in Sec. 7.8.

7.4.1 Higher Order Non-linearities

First, we only considered the linear and quadratic terms in N_e in our Hamiltonian, which is accurate for very weak dressing. Applying stronger dressing fields yields a stronger interaction, but also increases the importance of higher order terms in Eq. (7.5). To quantify the effects of these higher orders, we calculate the fidelity of the cat state ($|\psi'(\tau_c)\rangle$) generated based on Eq. (7.4) with respect to the closest ideal cat state,

$$F_{nl} = \max_{\theta,\phi,\alpha,\tau_c} |\langle \psi'(\tau_c)| \frac{1}{\sqrt{2}} (|\theta,\phi\rangle + e^{i\alpha}|\pi-\theta,\phi+\pi\rangle)|^2. \tag{7.11}$$

Fig. 7.2 shows that the weak dressing parameter $w = \frac{\Omega_r}{2\Delta}$ has to be reduced for larger atom numbers in order to achieve a desired fidelity.

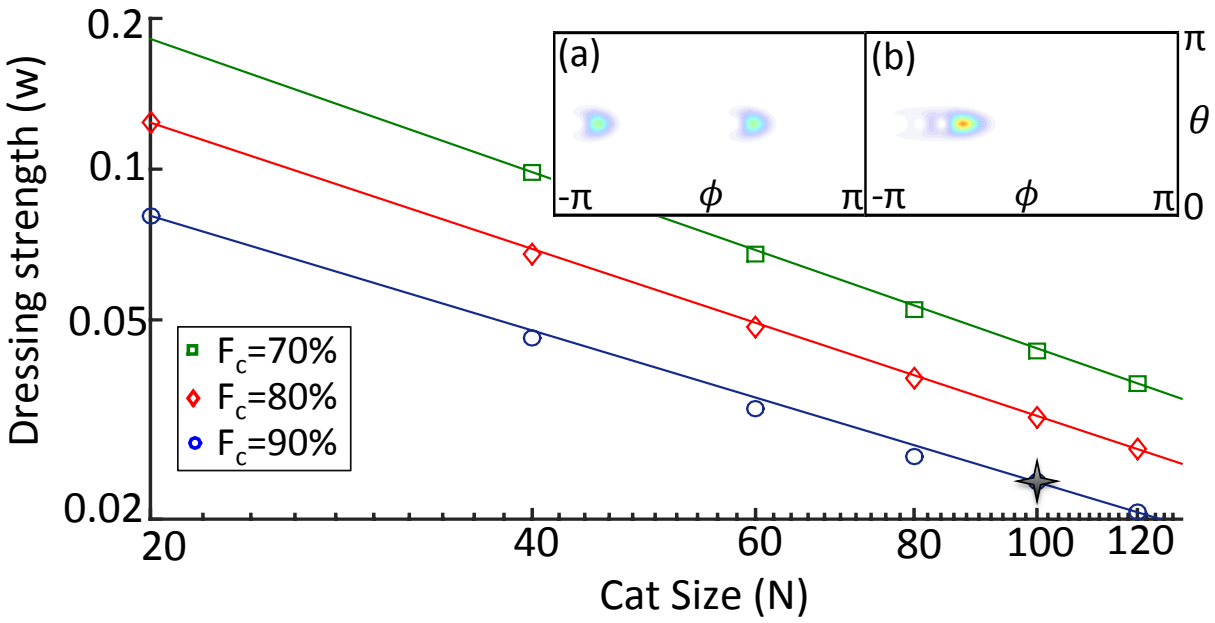

Figure 7.2: (Color online) Effect of higher than second order nonlinearities (from the higher orders of Eq. 7.5) on the fidelity of the cat state. The weak dressing parameter ($w = \frac{\Omega_r}{2\Delta}$) has to be reduced for larger atom numbers N in order to keep a fixed fidelity F_{nl} ($F_{nl} = 0.7$ (green), 0.8 (red), 0.9 (blue) from top to bottom). The inset shows the Husimi Q function for an $N = 100$ cat state (a) with $F_{nl} = 0.9$ (corresponding to the black cross in the main figure), as well as the corresponding revival (b). The approximate revival of the initial CSS at the time $t = 2\tau_c$ proves the existence of a quantum superposition at $t = \tau_c$.

7.4.2 Effects of Interaction Inhomogeneities

We also considered a uniform blockade over the entire medium, leading to a homogeneous interaction. In practice the interaction is not perfectly homogeneous. As explained in section 5.10, the interaction of the entire weakly dressed system can be found by applying the fourth order perturbation theory as [236, 237]

$$\hat{H} = \sum_{i<j} \chi(r_{ij}) \hat{\sigma}^i_{ee} \hat{\sigma}^j_{ee} - \frac{\Omega^2}{4\Delta} \hat{N}_e. \tag{7.12}$$

The many-body interaction is the sum of binary interactions

$$\chi(r_{ij}) = \chi_0 \frac{R_b^6}{r_{ij}^6 + R_b^6}, \tag{7.13}$$

where $R_b = |\frac{C_6}{2\Delta}|^{1/6}$ is the blockade radius in the weak dressing regime. This binary interaction has a plateau type nature, see Fig. 7.3(a). The inhomogeneity of the interaction introduces a coupling to non-symmetric states, since the Hamiltonian no longer commutes with the total spin operator ($[S^2, H] \neq 0$). We evaluate the fidelity of a cat state created by the realistic non-uniform interaction with respect to the ideal cat state. Writing the pair interactions $\chi(r_{ij})$ in terms of small fluctuations ϵ_{ij} around a mean value χ_m, we decompose the Hamiltonian into a sum of two commuting terms,

$$\hat{V}_H = \sum_{i<j} \chi_m \hat{\sigma}^i_{ee} \hat{\sigma}^j_{ee} - \frac{\Omega^2}{4\Delta} \hat{N}_e = \chi_m (\frac{\hat{N}_e^2 - \hat{N}_e}{2}) - \frac{\chi_0}{2w^2} \hat{N}_e \approx \frac{\chi_m}{2} \hat{N}_e^2 - \frac{\chi_0}{2w^2} \hat{N}_e \tag{7.14}$$

and

$$\hat{V}_{IH} = \sum_{i<j} \epsilon_{ij} \hat{\sigma}^i_{ee} \hat{\sigma}^j_{ee}, \tag{7.15}$$

corresponding to the homogeneous and inhomogeneous parts respectively. While the homogeneous part leads to an ideal cat state, the inhomogeneous part reduces the fidelity by a factor

$$F_{IH} = |\langle \eta = 1 | e^{-i\hat{V}_{IH}\tau_c} | \eta = 1 \rangle|^2, \tag{7.16}$$

where $|\eta = 1\rangle = (\frac{|e\rangle + |g\rangle}{\sqrt{2}})^N$ is the initial CSS. Taylor expanding the inhomogeneous part of the evolution operator one obtains an estimate for the fidelity as explained in Appendix

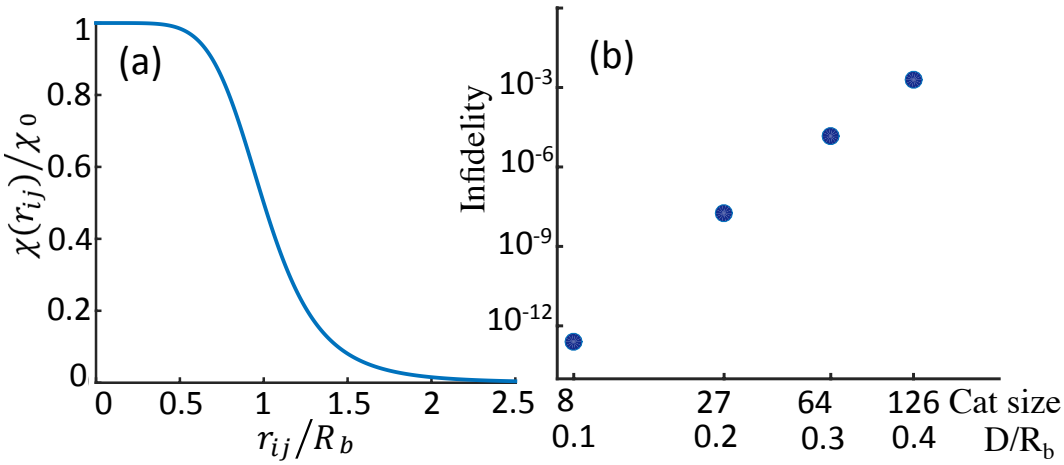

Figure 7.3: (Color online) Effect of interaction inhomogeneity. (a) Plateau-type interaction between each pair of atoms dressed to the Rydberg state. The interaction is uniform for separations up to of order the blockade radius. (b) Infidelity caused by interaction inhomogeneity as a function of cat size (N), for a constant blockade radius. Non-linear fidelity is set to $F_{nl} = 0.9$, the blockade radius $R_b = 3.6\mu$m is created by Rydberg dressing to $n = 80$, and the atoms are considered to be in a cubic trap with space diagonal D and lattice spacing of 200nm.

7.11. Fig. 7.3(b) shows the resulting infidelity as a function of cat size for constant blockade radius.

7.5 Decoherence

The main source of decoherence in our system is depopulation of the Rydberg level which also determines the lifetime of the dressed state ($\tau_{\tilde{e}} \approx \tau_r w^{-2}$). In this section we identify different Rydberg decay channels and discuss their effects on the fidelity of the cat state. Loss due to collisions is reduced by the use of an optical lattice trap with a single atom per site. Ref. [238] implemented a Strontium optical clock using a blue-detuned lattice (trap laser wavelength 390 nm) with a collision-limited lifetime of 100s, demonstrating that loss due to the trap laser can be made negligible. Other sources of decoherence including blackbody radiation induced transitions, collective many-body decoherence and molecular formation will be discussed in Sec. 7.8.

7.5.1 Rydberg Decay Channels

The main source of decoherence in our system is depopulation of the Rydberg level which also determines the lifetime of the dressed state ($\tau_{\tilde{e}} \approx \tau_r w^{-2}$). The Rydberg state depopulation rate can be calculated as the sum of spontaneous transition probabilities to the lower states (given by Einstein A-coefficients) [146, 147, 148]

$$\tau_r^{-1} = \sum_f A_{if} = \frac{2e^2}{3\epsilon_0 c^3 h} \sum_{E_f<E_i} \omega_{if}^3 \left|\langle i|\vec{r}|f\rangle\right|^2, \tag{7.17}$$

where $\omega_{if} = \frac{E_f - E_i}{\hbar}$ is the transition frequency and $\langle i|\vec{r}|f\rangle$ is the dipole matrix element between initial and final states (see Appendix 7.12). The summation is only over the states $|f\rangle$ with lower energies compared to the initial state. Using a cryogenic environment [239], black-body radiation induced transitions are negligible, see Sec. 7.8.3 for detailed discussion.

Considering the dressing to $5sns\,^3S_1$ in our proposal, the possible destinations of dipole transitions are limited to $^3P_{0,1,2}$, due to the selection rules. Around 55% of the transferred population will be trapped within the long-lived $^3P_2$ states, which we refer to as qubit loss. Around 35% of the population is transferred to $^3P_1$ states, which mainly decay to the ground state $|g\rangle = 5s^2\,^1S_0$ within a short time (e.g. $\tau_{5s5p\,^3P_1} = 23\mu s$ [240]), which we refer to as de-excitation. The remaining 10% of the population is transferred to $^3P_0$ states. Half of this population (5% of the total) contributes to qubit loss, bringing the total loss to 60 %, while the other half (also 5% of the total) is transferred to the excited state, which effectively causes dephasing of $|\tilde{e}\rangle$ because the photon that is emitted in the process contains which-path information about the qubit state.

7.5.2 Effects of Rydberg Decoherence on the Cat State

The three decoherence types discussed in the previous sub-section have different effects on the cat state. Loss and de-excitation completely destroy the cat state if they occur, while dephasing is both unlikely and relatively benign. We now explain these statements in more detail.

The majority (60%) of the dressed state's decay goes to non-qubit states

$$|\tilde{e}\rangle \Rightarrow \delta|\tilde{e}\rangle|0\rangle_p + \sqrt{1-\delta^2}|l\rangle|1\rangle_p, \tag{7.18}$$

where $\delta^2 = e^{-0.6\gamma_{\tilde{e}}\tau_c}$ and $|1\rangle_p$ represents the emitted photon. In addition to loss, 35% of the dressed state's decay is de-excitation

$$|\tilde{e}\rangle \Rightarrow \delta|\tilde{e}\rangle|0\rangle_p + \sqrt{1-\delta^2}|g\rangle|1\rangle_p, \tag{7.19}$$

where $\delta^2 = e^{-0.35\gamma_{\tilde{e}}\tau_c}$.

Decay of a single dressed state atom transforms an atomic symmetric Dicke state $|N; N_e\rangle$ into a combination of the original state $|N; N_e\rangle$, a symmetric Dicke state $|N; N_e - 1\rangle$ with one fewer excitation, and N different other Dicke states ($|N-1; N_e-1\rangle_{\tilde{i}}|l\rangle_i$) in which the i-th atom is transferred to a non-qubit state (the qubit is lost), but which are still symmetric Dicke states for the remaining atoms. The resulting state is

$$\sqrt{P_0}|N; N_e\rangle|0\rangle_P + \sqrt{P_{de}N_e}|N; N_e-1\rangle|1\rangle_P + \sqrt{\frac{P_l N_e}{N}}\sum_{i=1}^{N}|N-1; N_e-1\rangle_{\tilde{i}}|l\rangle_i|1\rangle_P \tag{7.20}$$

where $P_k = \lambda_k e^{-\lambda_k}$ is the probability of losing/de-exciting ($k = l/de$) an atom over the cat creation time, with $\lambda_k = \gamma_{(k)}\frac{N}{2}\tau_c$ (note that $N_e \sim \frac{N}{2}$ since the cat creation happens on the equator of Bloch sphere) and $P_0 = 1 - P_l - P_{de}$. Here we focus on the regime where the probability of a single atom decaying is sufficiently small that the probability of two atoms decaying can be ignored.

Tracing over the lost qubit and the photonic state one obtains the density matrix of

$$\rho_c = P_0\rho_0 + \frac{P_l}{N}\sum_{i=1}^{N}\rho_l^i + P_{de}\rho_{de}, \tag{7.21}$$

where ρ_0 and ρ_{de} are in the symmetric subspace with total spin ($J = \frac{N}{2}$), while the ρ_l^i are in N different symmetric subspaces with total spin ($J = \frac{N-1}{2}$). The ρ_0 component corresponds to the ideal cat state. All the other components have very small fidelity with ideal cat states, primarily because the decay happens at a random point in time, which leads to dephasing.

For example, de-excitation of an atom at ($t_{de} \in [0, \tau_c]$), leads to

$$|\psi_c^{de}(t_{de})\rangle = 2^{-N/2} \sum_{N_e=1}^{N} \sqrt{C(N, N_e)} e^{-iE_{(N_e-1)}(\tau_c - t_{de})} \sqrt{N_e} e^{-iE_{(N_e)} t_{de}} |N; N_e - 1\rangle, \quad (7.22)$$

where $E_{(N_e-1)}$ represents the dressed state energy of $(N_e - 1)$ excited atoms, see Eq. (7.6). Inserting the expressions for E_{N_e} and E_{N_e-1}, one sees that de-excitation adds a linear term $(iN_e\chi_0 t_{de})$ to the phase. This creates a rotation around the z axis on the Bloch sphere. The uncertainty in the time of decay t_{de} therefore dephases the cat state, resulting in the formation of a ring on the equator of the Bloch sphere, which has a small overlap with the ideal cat state. The fidelity of the resulting density matrix compared to an ideal cat state in the same subspace (which corresponds to the case where de-excitation happens at $t_{de} = 0$) can be written as

$$F_{de} = \frac{1}{\tau_c} \int_0^{\tau_c} |\langle \psi_c^{de}(t_{de}) | \psi_c^{de}(t_{de} = 0) \rangle|^2 dt_{de}. \quad (7.23)$$

When the size of the cat state is increased from $N = 10$ to $N = 160$, the fidelity of the generated cat in the de-excited subspace is reduced from $F_{de} = 0.2$ to $F_{de} = 0.045$, see Fig. 7.4. The fidelity in each of the N subspaces where one atom was lost can be calculated in a similar way, yielding equivalent results. The total fidelity in the presence of Rydberg decoherence is then

$$F_{dc} = P_0 + P_l F_l + P_{de} F_{de} \approx P_0. \quad (7.24)$$

About 5% of Rydberg decoherence will transfer back to the excited state, which acts as dephasing (modeled by a Lindblad operator $|\tilde{e}\rangle\langle\tilde{e}|$). The dephasing operator commutes with the Hamiltonian for cat state creation. Its effect can therefore be studied by having it act on the final cat state. For example, it can cause a sign flip of $|e\rangle$ for the first atom, resulting in a state

$$\left(\frac{|e\rangle + i|g\rangle}{\sqrt{2}}\right)\left(\frac{|e\rangle - i|g\rangle}{\sqrt{2}}\right)^{\otimes(N-1)} + \left(\frac{|e\rangle - i|g\rangle}{\sqrt{2}}\right)\left(\frac{|e\rangle + i|g\rangle}{\sqrt{2}}\right)^{\otimes(N-1)}. \quad (7.25)$$

Applying the $\pi/2$ rotation results in a new energy cat

$$\frac{|g\rangle|e\rangle^{N-1} + |e\rangle|g\rangle^{N-1}}{\sqrt{2}}, \quad (7.26)$$

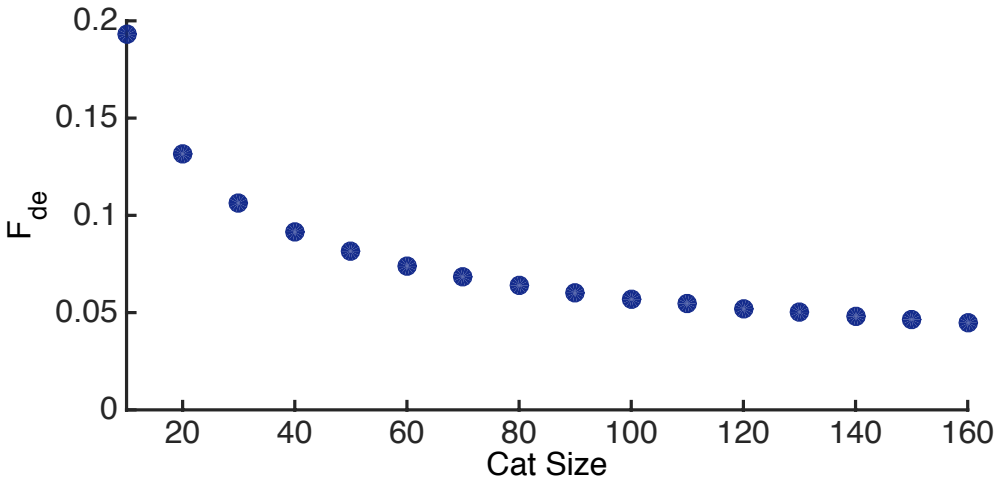

Figure 7.4: Fidelity of the generated cat state in the de-excited subspace of density matrix as a function of cat size, see Eq. 7.23. Uncertainty in the time of decoherence dephases the cat state and results in the formation of a ring with small overlap with an ideal cat in the same subspace.

which is clearly still a large superposition in energy. So the effect of dephasing errors is relatively benign. Moreover, given the small relative rate of dephasing compared to loss and de-excitation, the probability of having a sign flip over the cat creation time for the case with decoherence fidelity of $F_{dc} = 0.8$ (considered in Fig. 7.5) will only be 1%.

In conclusion, the fidelity of the cat state is, to a good approximation, equal to the probability of not losing or de-exciting any qubits over the cat creation time, $F_{dc} = P_0 = e^{-0.95\frac{N}{2}\gamma_{\bar{e}}\tau_c}$.

7.6 Estimate of Realizable Cat Size

Taking into account the mentioned imperfections, Fig. 7.5 shows the achievable cat size as a function of the principal number n. Up to $n \sim 80$, the size increases with n. Higher n leads to a stronger interaction, hence allowing weaker dressing, and to smaller loss, favoring the creation of larger cats. However, for $n \sim 80$ the diminishing spacing between neighboring Rydberg levels (which scales like n^{-3}) limits the detuning and hence the interaction strength, since $\chi_0 = 2w^4\Delta$ and w has to be kept small, see Fig. 7.2. As a consequence, larger cat

states cannot be achieved at higher principal numbers.

Here we justify the behavior of Fig. 7.5 in a more detailed scaling argument. For a constant fidelity the maximum achievable cat size N at each principal number n is limited by Rydberg decay, $F_{dc} = e^{-\lambda}$ where $\lambda = 0.95\frac{N}{2}\tau_c\gamma_{\tilde{e}}$. Let us analyze how λ scales with N and n. The Rydberg decay rate scales as $\gamma_{|\tilde{e}\rangle} \propto w^2 n^{-3}$. In order to have a constant non-linearity fidelity of $F_{nl} = 0.8$, the dressing strength w has to scale like $N^{-0.84}$, see Fig. 7.2. The cat creation time $\tau_c = \frac{\pi}{\chi_0} \propto w^{-4}\Delta^{-1}$ scales differently before and after the transition point $n \sim 80$. Before the transition point the scaling of Δ can be obtained by noting that the trap size is a fraction of the blockade radius, $\Delta = \frac{C_6}{2R_b^6} \propto \frac{n^{11}}{N^2}$, where the exact value of the fraction coefficient is determined by F_{IH}, see Fig. 7.3. Therefore we conclude that $\lambda \propto \frac{N^{4.7}}{n^{14}}$, which states that before the transition point larger cat states are realizable by dressing to higher principal numbers, $N \propto n^3$ for constant fidelity. However, after the transition point the small level spacing imposes a limit on the detuning, $\Delta \propto n^{-3}$. Therefore after the transition point $\lambda \propto N^{2.7}$, which is independent of n. This prevents the realization of larger cat states at higher principal numbers.

One sees that superposition states of over 100 atoms are achievable with good fidelity. In Fig. 4 the interaction inhomogeneity is tuned to create less than 1% infidelity. Dressing to an S orbital is desired due to its isotropic interaction in the presence of trap fields. In Fig. 7.5, after the transition point in n the detuning is chosen such that 90% of the Rydberg component of the dressed state is $5sns\,^3S_1$. Note that without a cryogenic environment the maximum achievable cat size in Fig. 7.5 would be reduced from 165 to 120 atoms, see Sec. 7.8.3.

7.7 Experimental Realization

Experimental implementation of our scheme seems feasible. Rydberg excitations in Strontium have been realized over a wide range up to $n = 500$ [241, 242, 243, 244]. Rydberg

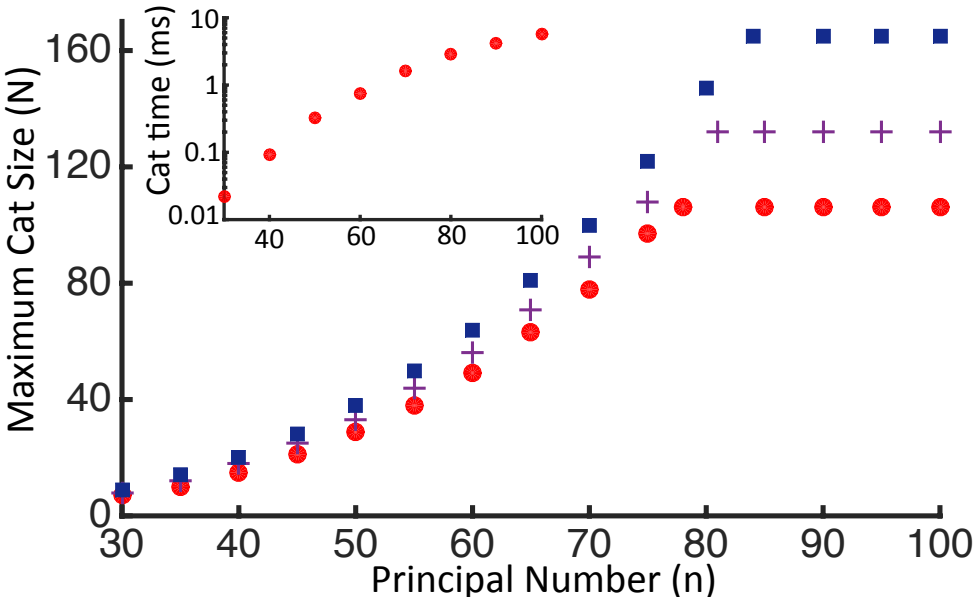

Figure 7.5: (Color online) Maximum achievable cat size as a function of the principal number n of the Rydberg state. Rydberg state decay is adjusted to cause 20% infidelity. The interaction inhomogeneity is set to create less than 1% infidelity, see Fig. 3, and the higher-order nonlinearities are set to create 10% (red circle), 20% (purple plus) and 30% (blue square) infidelity, see Fig. 2. The inset shows the required cat creation time as a function of n for the case where the higher-order nonlinearities cause 10% infidelity.

dressing of two atoms has been used to create Bell-state entangled atoms [245]. Recently Rydberg dressing of up to 200 atoms in an optical-lattice has been reported [246], where the collective interaction was probed using interferometric techniques. Ref. [246] also identified a collective many-body decay process, which is however not a limiting factor for our scheme, as discussed in Sec. 7.8.4.

The Rydberg state $5sns\,^3S_1$ is accessible from the $5s5p\,^3P_0$ level with a 317nm laser field. The required Rydberg transition Rabi frequency $\Omega_r/2\pi$ (up to 15 MHz) can be obtained with a tunable single-frequency solid state laser of Ref. [247]. The relatively large detuning values (4MHz$< \Delta/2\pi <$ 340MHz in Fig. 4) make the interaction stable against Doppler shifts.

Fulfilling the adiabaticity condition discussed in Sec. 7.3.1 is not difficult. In a highly adiabatic example, $\frac{\dot{\theta}}{E_+} = 0.01$, the dressing laser can be switched from zero to $\frac{\Omega_r}{2\pi} = 15$ MHz over 18 ns (for $\frac{\Delta}{2\pi} = 270$ MHz and 165 atoms). For this example, 99.991% of the population

returns to the ground state at the end of dressing, so adiabaticity is almost perfect. This adiabatic switching time of 18 ns is many orders of magnitude shorter than the related cat creation time of 1.4 ms. Adequate interaction timing precision is also required to align the created cat on the equator of Bloch sphere as explained in Sec. 7.3.3. For the 165-atom cat state mentioned above, a timing precision of order $\delta\tau_c = \frac{2w^2\,\delta\phi}{\chi_0} = \frac{4\Delta}{5\sqrt{N}\Omega_r^2} \approx 7.5$ ns is required for a phase precision of order $\delta\phi = \frac{1}{5\sqrt{N}} = \pi/150$.

The Husimi Q function can be reconstructed based on tomography, i.e. counting atomic populations after appropriate rotations on the Bloch sphere. Modern fluorescence methods can count atom numbers in the required range with single-atom accuracy [246, 248].

7.8 Other Sources of Imperfection

7.8.1 Effects of Atomic Motion in the Optical Lattice

Laser manipulation of the atomic state leads to phases that depend on the atomic position. Atomic motion could therefore lead to decoherence. To suppress this effect, in the present proposal the atoms are confined to the ground states of the optical lattice traps. As a consequence, all position-dependent phase factors are constant over the course of the experiment and can be absorbed into the definition of the excited states. We now explain these points in more detail. Let us consider the j^{th} atom, and let us assume that it is initially in the ground state (zero-phonon state) of its optical lattice site. We will denote the corresponding state $|g\rangle_j|0\rangle_j$. Applying the part of the Hamiltonian that is due to the laser to this state gives

$$(\Omega_e(t)\; e^{ik\hat{x}_j}|e\rangle_j\langle g|)\,|g\rangle_j|0\rangle = \Omega_e(t)|e\rangle_j e^{ik\hat{x}_j}|0\rangle_j. \tag{7.27}$$

We can rewrite the position operator $\hat{x}_j$ as the sum of the constant position of the j^{th} site of the trap (x_{0j}) plus a relative position operator $\hat{\xi}_j = s(\hat{a}_j^\dagger + \hat{a}_j)$, where $s = \sqrt{\frac{\hbar}{2m\omega_{tr}}}$ is the spread of the ground state wave function, ω_{tr} is the trap frequency and $(\hat{a}_j, \hat{a}_j^\dagger)$ are the phononic annihilation-creation operators of the jth atom. In the Lamb-Dicke regime ($\eta = \frac{ks}{\sqrt{2}} \ll 1$)

one can expand the exponential to get

$$e^{ik\hat{x}_j} = e^{ikx_{0j}} e^{ik\hat{\xi}_j} = e^{ikx_{0j}}(l + i\eta(\hat{a}_j + \hat{a}_j^\dagger) + O(\eta^2)). \tag{7.28}$$

The phase factor $e^{ikx_{0j}}$ is constant over the course of the experiment and can be absorbed into the definition of the atomic basis states by defining $|e'\rangle_j \equiv e^{ikx_{0j}}|e\rangle_j$. The Hamiltonian describing the laser excitation can now be written in the new basis $|g,0\rangle_j$, $|e',0\rangle_j$, $|e',1\rangle_j$ as:

$$\begin{pmatrix} 0 & \Omega_e & \eta\Omega_e \\ \Omega_e & 0 & 0 \\ \eta\Omega_e & 0 & \omega_{tr} \end{pmatrix} \begin{pmatrix} |g,0\rangle_j \\ |e',0\rangle_j \\ |e',1\rangle_j \end{pmatrix} \tag{7.29}$$

Starting from the spin and motional ground state $|g,0\rangle_j$, the probability of populating the state $|e',1\rangle_j$, corresponding to the creation of a phonon, will be negligible if $\Omega_e\eta \ll \omega_{tr}$. With the parameters that we considered in our proposal ($\Omega_e \sim 1$ kHz, $\eta = 0.1$, $\frac{\omega_{tr}}{2\pi} \sim 400$ kHz) [232] the population of $|e',1\rangle_j$ will be eight orders of magnitude smaller than the population in the motional ground state.

7.8.2 Effects of High Density

The relatively small lattice spacing of order 200nm might raise concerns about molecule formation and level mixing. At high atomic densities there is another potential loss channel, Rydberg molecule formation [249]. Molecule formation only occurs when the attractive potential due to Rydberg electron-neutral atom scattering moves the two binding atoms to a very small separation (of order 2nm), where the binding energy of the molecules can ionize the Rydberg electron and form a Sr_+^2 molecule [250]. Without the mass transport, stepwise decay or ionization of the Rydberg atom is ruled out by the quantization of Rydberg state, as has been discussed and experimentally tested in [249], because even at high densities the small molecular binding energy of nearby atoms is orders of magnitude smaller than the closest Rydberg levels for all the principal numbers. The occurrence of ion pair formation is

also highly unlikely in this system [250]. We propose that confining the atoms by an optical lattice can prevent the described mass transport and completely close the molecule formation loss channel. High atomic density can also lead to strong level mixing at short distances [251, 252]. However, the experiment of Ref. [253] shows that the plateau-type interaction can persist in the presence of strong level mixing because most molecular resonances are only weakly coupled to the Rydberg excitation laser.

7.8.3 Effects of Blackbody Radiation

Blackbody radiation (BBR) could reduce the lifetime by transferring the Rydberg state population to neighboring Rydberg levels (with both higher and lower principal numbers n) as illustrated in Fig. 7.6a. The BBR-induced transition probability is given by the Einstein B-coefficient [146, 147, 148]

$$\Gamma_{BBR} = \sum_f B_{if} = \sum_f \frac{A_{if}}{e^{\frac{\hbar\omega_{if}}{k_B T}} - 1}, \tag{7.30}$$

where T is the environment temperature, k_B is the Boltzmann constant and both ω_{if} and A_{if} are defined in Sec. 7.5.1.

At the environment temperatures of 300K, 95K [254] and 3K [255], including the BBR-induced transitions increases the total decoherence rate $\Gamma_{\tilde{e}}$ by 120%, 40% and 1% (see Fig. 7.6b) for $n \approx 80$, which results in maximum achievable cat sizes of 120, 150 and 165 atoms respectively (considering $F_{nl} = 0.7$, $F_{dc} = 0.8$). Note that cryogenic environments with 95K and 1K were used in a Strontium lattice clock experiment [254] and in a cavity QED experiment with Rydberg atoms [255] respectively.

BBR could also disturb the Ramsey-type interferometry used for detecting energy decoherence by producing an AC stark shift; this effect is quantified in section 7.9. Furthermore, BBR-induced decoherence could be inhomogeneous due to temperature inhomogeneities in the environment. This would introduce unwanted coupling to non-symmetric Dicke states in the cat creation process. The use of a cryogenic environment significantly suppresses these

effects as well.

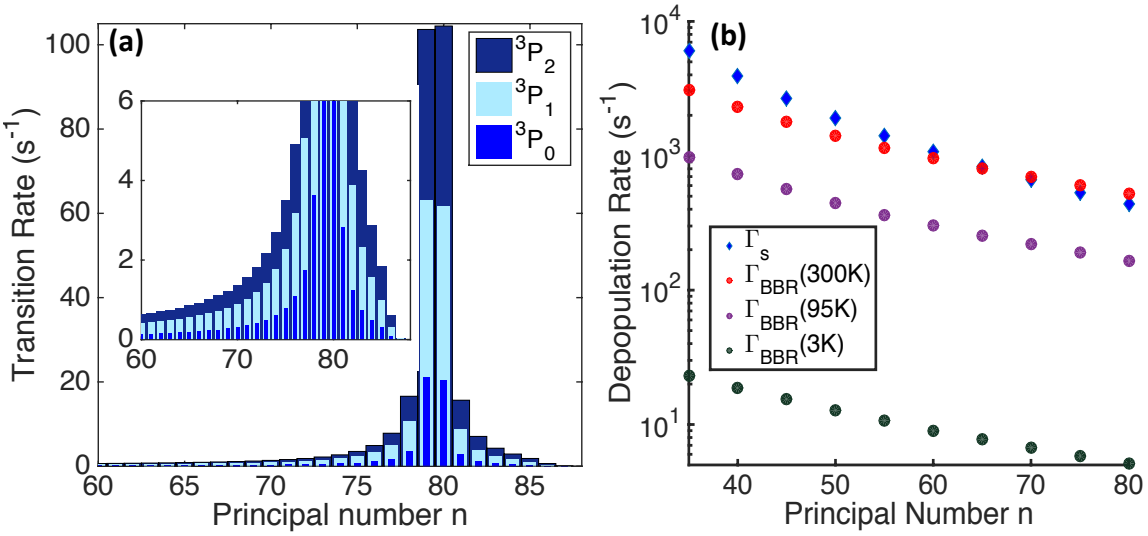

Figure 7.6: (Color online) Depopulation of Strontium Rydberg levels due to blackbody radiation (BBR) induced transitions. a) BBR-induced transition rates (Einstein-B coefficients) from $5s80s\,^3S_1$ to the neighboring $5snp\,^3P_2$ (dark blue), $5snp\,^3P_1$ (light blue), $5snp\,^3P_0$ (blue) levels. The sum of these transition rates gives the total BBR-induced depopulation rate Γ_{BBR}. The inset is a 20 times enlarged view. b) Rydberg depopulation rates due to spontaneous decay (Γ_s shown in blue diamond) and BBR-induced transitions (Γ_{BBR}) at environment temperatures of 300K (red circle), 95K [254] (purple circle), and 3K [255] (green circle) as a function of the principal number. The use of a cryogenic environment significantly suppresses the unwanted effects of BBR.

7.8.4 Effects of Collective Many-body Decoherence

BBR-induced transitions to neighboring Rydberg levels (see Fig. 7.6a) can also lead to collective many-body decoherence [256, 246]. The interaction between the target nS Rydberg level and some of the populated neighboring $n'P$ levels is of a strong long-range dipole-dipole type due to the formation of Förster resonances. This strong interaction causes an anomalous broadening [256]. The mentioned decoherence process only starts after the first BBR-induced transition occurs. However, the weak dressing strength and small ensemble size ($N < 200$) in our scheme make the probability of populating the target Rydberg state and consequently neighboring Rydberg levels very small. For example at the environment

temperatures of 300K, 95K and 3K and for dressing to $n \approx 80$, the probabilities of not populating the strongly interacting neighboring Rydberg levels over the cat creation time for cat sizes of 120, 150 and 165 atoms respectively are $P_{BBR}(0) = exp(-\frac{N}{2}w^2\Gamma_{BBR}\tau_c)$ =98.63%, 99.26% and 99.96% respectively. It has been observed in the realization of many particle Rydberg dressing [246] that when the transition probability is low enough (of the order of $P_{BBR}(0) \geq 82\%$, as can be calculated from the information provided in Ref. [246]) the many-body decoherence effects are negligible and decoherence rate is dominated by the Rydberg depopulation rate (see Sec. 7.5).

7.9 Testing Energy Decoherence

In the context of modifications of quantum physics, decoherence in the energy basis is quite a natural possibility to consider [219, 220, 221]. It is usually introduced as an additional term in the time evolution for the density matrix that is quadratic in the Hamiltonian

$$\frac{d\rho}{dt} = \frac{i}{\hbar}[H, \rho] - \frac{\sigma}{\hbar^2}[H, [H, \rho]], \tag{7.31}$$

which leads to a decay of the off-diagonal terms of the density matrix in the energy basis according to [220]

$$\rho_{nm}(t) = \rho_{nm}(0)e^{-i\omega_{nm}t}e^{-\gamma_E t}, \tag{7.32}$$

where $\gamma_E = \sigma\omega_{nm}^2$. Here ω_{nm} is related to the energy difference of the two componants and σ can be interpreted as a timescale on which time is effectively discretized, e.g. related to quantum gravity effects. It is of interest to establish experimental bounds on the size of σ, which could in principle be as small as the Planck time (10^{-43} s).

The corresponding decoherence rate for the energy cat in this proposal would be

$$\gamma_E = \sigma(\frac{N\Delta E}{\hbar})^2, \tag{7.33}$$

where ΔE is the energy difference between the ground and excited state of each qubit, and N is the cat size. To detect the energy decoherence one prepares the energy cat state, followed

by a waiting period. To observe the decoherence effect, one detects the Ramsey fringes for the revival. The visibility of the Ramsey interference is also sensitive to other decoherence sources, where in the absence of dressing laser the dominant ones are the trap loss rate Γ, which reduces the visibility by a factor $\exp(-N\Gamma t)$, and phase diffusion that is explained below.

The large energy difference of the cat state increases the sensitivity of the Ramsey interferometry that we are using for the detection of energy decoherence. Therefore, it is important to consider the effect of fluctuations in the detuning between the laser and the atomic transition. Let us first note that the cat state is more sensitive to multi-particle (correlated) than to single-particle (uncorrelated) noise, which results in a phase diffusion affecting the visibility of Ramsey fringes by $e^{-N^2\delta_c^2 t^2}$ and $e^{-N\delta_{uc}^2 t^2}$ respectively [257]. Comparing the two cases, correlated fluctuations should be $\sqrt{N}$ times more stabilized than uncorrelated fluctuations. The most important source of noise in our system is the fluctuation of the laser frequency. A probe laser linewidth as narrow as 26 mHz [258] has been achieved in optical atomic clock experiments, and there are proposals for much smaller linewidths [259, 260] with recent experimental progress [261], justifying our example of a 10mHz linewidth, see below.

Other sources of multi-particle and single-particle noise have been well studied in the context of Strontium atomic clocks [262, 263] and are comparatively negligible. Here we address a few of them in our scheme. One of the noise sources is the trap fields intensity fluctuation; however, using the magic wavelength makes the atomic transition frequency independent of the trap laser intensity. Considering the variation of the Stark shifts due to the trap laser as a function of frequency at the magic wavelength [264], the relative scalar light shifts could be kept within 0.1mHz uncertainty by applying a trap laser with a 1MHz linewidth. In addition to the scalar light shift, the inhomogeneous polarization of trap fields in 3D optical lattices can result in an inhomogeneous tensor light shift [265]; however, the

use of the bosonic isotope ^{88}Sr with zero magnetic moment cancels the tensor light shift [266] in our scheme. Environmental temperature fluctuations (δT) also lead to atomic frequency fluctuations that are proportional to $T^3\delta T$ due to the BBR-induced light shift [262]. This is another reason why a cryogenic environment is advantageous. For example controlling the environment temperature of 95K [254] to within a range of $\delta T = 1K$ keeps the BBR-induced noise shift below 1 mHz.

A conservative estimate of the experimentally measurable energy decoherence rate can be obtained by considering the case where the energy decoherence dominates all other decoherence sources during the waiting period. Increasing the cat size N is helpful because it allows one to enhance the relative size of the energy decoherence contribution. For example, choosing $t \propto N^{-1}$ keeps the loss and phase diffusion contributions fixed, while the energy decoherence still increases proportionally to N. Using a cat state with $N = 165$ atoms (see Fig. 4), which corresponds to $N\Delta E = 300$ eV, assuming a laser linewidth of 10 mHz (see above), and considering a trap loss rate of $\Gamma = 10$ mHz [249], the minimum detectable discretization time scale σ is of order 10^{-34} s. This would improve the measurement precision by 4 and 11 orders of magnitude compared to what is possible based on Ref. [227] and Ref. [226] respectively.

7.10 Conclusion

This chapter was a step towards the generation of macroscopic quantum states. The presented scheme results in the superposition states of over 100 Strontium atoms in the optical lattice being in a ground state or metastable optical clock state. This large GHZ state is created under the Kerr type interaction that can be realized via the adiabatic weak Rydberg dressing of atoms. The process under which the Kerr-type interaction splits the initial coherent spin state to form a cat state is analyzed and the effects of imperfections are studied. These imperfections include the inhomogeneity of the Kerr type interaction, higher

order nonlinearities and the level of atomic confinement to the trap. In addition different decoherence sources include de-excitation, dephasing and loss of spins, blackbody radiation induced Rydberg depopulation, molecular formation and also collective many-body decoherences were studied. Considering all the imperfections we showed that cat states of the order of 100 atoms are realizable with current technologies. The two components of the superposition can differ by of order 300 eV in energy, allowing tests of energy decoherence models. The large energy difference of the two components makes the interferometry sensitive to the correlated as well as uncorrelated noises. The corresponding phase diffusion terms were taken into account to find the precision of the energy decoherence measurement. The presented scheme improves the precision by several orders comparing to previous proposals.

7.11 Appendix 1. Effects of Interaction Inhomogeneity

Here we explain the steps in calculating the effects of inhomogeneous interaction on the cat state's fidelity

$$F_{IH} = |\langle \eta = 1 | e^{-i\hat{V}_{IH}\tau_c} | \eta = 1 \rangle|^2 \tag{7.34}$$

(see Sec. 7.4.2). Taylor expanding $e^{-i\hat{V}_{IH}\tau_c}$ and considering the expectation values

$$\begin{aligned} &\langle \eta = 1 | \hat{\sigma}^i_{ee} | \eta = 1 \rangle = 1/2 \\ &\langle \eta = 1 | \hat{\sigma}^i_{ee} \hat{\sigma}^j_{ee} | \eta = 1 \rangle = \frac{1}{4} + \frac{\delta_{ij}}{4}, \end{aligned} \tag{7.35}$$

one obtains an estimate for the fidelity. The first order of the expansion is zero because we defined ϵ_{ij} as fluctuations around a mean value. The second order can be calculated using

$$\langle \eta = 1 | \hat{V}^2_{IH} | \eta = 1 \rangle = \frac{1}{2} \sum_{i \neq j} \frac{1}{2} \sum_{l \neq m} C_{ijlm} \epsilon_{ij} \epsilon_{lm}, \tag{7.36}$$

where $C_{ijlm} = 1/16$ if all the indices are unequal, $C_{ijlm} = 1/8$ if there is a pair of equal indices, and $C_{ijlm} = 1/4$ when there are two pairs of equal indices. The convergence of the expansion for the fidelity can be tested numerically. In Fig. 3b of the paper the ratio of the third order

to the second order of the expansion for F_{IH} is $\frac{O(3)}{O(2)} = 10^{-6}, 5\times10^{-5}, 8\times10^{-4}, 8\times10^{-3}$ for $\frac{D}{R_b} = 0.1, 0.2, 0.3, 0.4$ respectively, suggesting good convergence in this regime.

7.12 Appendix 2. Dipole Matrix Elements

In Strontium one needs to consider both valence electrons ($|i\rangle = |n_{1i}n_{2i}l_{1i}l_{2i}L_iS_iJ_iM_i\rangle$) in the calculation of the dipole matrix elements [148]

$$|\langle i|\vec{r}|f\rangle|^2 = \max(l_{2i}, l_{2f})\,(2L_f+1)(2J_f+1)(2L_i+1) \begin{Bmatrix} J_f & 1 & J_i \\ L_i & S & L_f \end{Bmatrix}^2 \begin{Bmatrix} L_f & 1 & L_i \\ l_{2i} & l_{1i} & l_{2f} \end{Bmatrix}^2 |\langle n_{2i}l_{2i}|r|n_{2f}l_{2f}\rangle|^2, \tag{7.37}$$

where L and S are the total orbital angular momentum and spin, l and s refer to individual electrons, and J and M refer to total angular momentum. The active electron in the transition is labeled by 2, and $\langle n_{2i}l_{2i}|r|n_{2f}l_{2f}\rangle$ is the radial dipole matrix element between initial and final state, and the curly bracket is a Wigner-6j symbol.

Chapter 8

Conclusion and Outlook

8.1 Conclusion

Advances in the field of atomic physics have paved the way towards the implementation of quantum information and also provided an ideal platform for fundamental tests of quantum physics. The present thesis contributes to the field of photonic quantum information by proposing schemes for the realization of two essential elements, namely quantum memory and photon-photon gates. In addition a proposal for the production of large energy superpositions with application to the test of energy decoherence models is presented.

In summary, chapter 4 proposed and analyzed a quantum memory protocol based on sweeping the resonance frequency of two-level atoms. The provided polaritonic model explained the propagation dynamics and coherent storage of the pulse in the medium. Also the requirements for efficient storage of light with high fidelity were discussed. We explained the criteria for resonant excitation of only one of the polaritons, closing the scattering channels between polaritons, and the requirement to preserve the shape of the polariton. While the two level polariton model presented here has similarities with the polaritons in electromagnetically induced transparency (EIT), the atomic frequency sweep (AFS) memory replicates the results of gradient echo memories (GEM) for short pulses in the excitation's moving frame. Therefore AFS could be seen as a bridge between coherent control and echo memories.

In the followed two projects the required interaction for making gates and creating many-body entangled states was obtained from exciting atoms to high principal numbers, i. e. Rydberg states. Rydberg atoms have remarkable properties such as strong long range interaction and long radiative lifetime as discussed in chapter 5.

Chapter 6 was a proposal for two-qubit photonic gate based on Rydberg interaction (instead of Rydberg Blockade) in an atomic ensemble. Several decoherence sources was recognized as summarized below. The first destructive effect is the fact that Rydberg interaction during EIT propagation causes loss and profile distortion. The proposed solution is based on separating interaction from propagation by storing single photons into excited atoms through non-Rydberg EIT and subsequently exciting non-Rydberg atoms to the Rydberg level using pi pulses. The second destructive effect comes from the inhomogeneity of interaction over the profiles of the two stored photons. This leads to a displacement of the collective excitations in momentum space and to entanglement between their quantum states. These effects a priori reduce the photon-photon gate fidelity. However, it is possible to completely compensate the first effect by swapping the collective excitations in the middle of the interaction time, and to greatly alleviate the second effect by optimizing the shape and separation of the excitations. Finally different sources of decoherence namely storage efficiency, atomic thermal motion and spontaneous emission from the Rydberg level and also the intermediate level during two photon excitations were discussed. Chapter 6 concluded that the mentioned imperfection sources are destructive but can be overcome with the provided solutions, making it realistic to achieve a gate operation with both high fidelity and efficiency.

Finally, chapter 7 was a step towards the generation of macroscopic quantum states. The presented scheme results in the superposition states of over 100 Strontium atoms in the optical lattice being in a ground state or metastable optical clock state. This large GHZ state is created under the Kerr type interaction that can be realized via the adiabatic weak Rydberg dressing of atoms. The process under which the Kerr-type interaction splits the initial coherent spin state to form a cat state is analyzed and the effects of imperfections are studied. These imperfections include the inhomogeneity of the Kerr type interaction, higher order nonlinearities and the level of atomic confinement to the trap. Due to the fragility

of the cat states a detailed study of different decoherence sources are provided. These decoherence sources include de-excitation, dephasing and loss of spins due to the Rydberg spontaneous emission, blackbody radiation induced Rydberg depopulation, molecular formation and also collective many-body decoherences. Considering all the imperfections we showed that cat states of the order of 100 atoms are realizable with current technologies. The two components of the superposition can differ by of order 300 eV in energy, allowing tests of energy decoherence models. The large energy difference of the two components makes the interferometry sensitive to the correlated as well as uncorrelated noises. The corresponding phase diffusion terms were taken into account to find the precision of the energy decoherence measurement. The presented scheme improves the precision by several orders comparing to previous proposals.

8.2 Future Perspectives

The discussed results have generated new questions and ideas that call for further investigation. Below, a few specific ideas are outlined, which might lead to promising avenues of research.

Spatial polariton model for GEM: Following the presented polariton model in chapter 4, it is interesting to explain the storage process of the gradient echo memory (GEM) through the presented spatial polariton model, where previous work has introduced gradient echo memory polaritons in momentum space [113].

Rydberg physics in high-density ensembles: High atomic density is desired for the Rydberg physics projects since this improves the atom photon coupling and also the interaction strength. However there are certain concerns that should be studied in more detail, namely level mixing, molecular formation and collective many-body decoherence. While we have taken some initial steps in chapter 7, a detailed comprehensive study and proven solutions to overcome these problems are required.

Hot vapor Rydberg quantum non-demolition measurement: Detecting the presence of single photons without disturbing their encoded information is very desirable for quantum information processing applications. Strong Rydberg interaction seems like a promising candidate for a fast non-demolition detection in hot atomic vapors, either through Rydberg interaction or blockade. The use of hot vapors rather than laser-cooled atoms would be advantageous from the perspective of practical implementation.

Photonic switch: Single photon switches have been realized based on Rydberg Blockade [267]. However the dissipative nature of those schemes makes them inappropriate for quantum applications. The studies of chapter 6 suggest non-dissipative interaction based schemes for a single photon switch with applications in entanglement generation.

Mechanical cat states: Following the results of chapter 7 it is interesting to map the created cat state to the mechanical oscillator. This transfer can be envisioned through dipole-dipole coupling between Rydberg atoms and a charged mechanical resonator.

Generating quantum phases: The Rydberg dressing potential has been applied for entangling qubits [245] and has been suggested for the realization of three dimensional solitons [268] and of squeezing[126], as well as for making quantum phases like spin ice [269], super solid [124, 270], super glass [271] and Luttinger liquid [272]. It is interesting to look for other quantum phases that can be generated under this interaction.

In general considering the previous successes of ultracold Rydberg physics in the field of quantum information, the next step is to learn from ultracold experiments and apply them in simpler and more compact Rydberg systems that are experimentally less demanding. These systems could be hot vapor atoms or semiconductors. The recent successes and the great interest in research on Rydberg states suggest a promising future for this field.

Bibliography

[1] D. Deutsch, Proc. R. Soc. Lond. A **400**, 97 (1985)

[2] P. W. Shor, SIAM J. Comput. **26**, 1484 (1997).

[3] L. K. Grover, Phys. Rev. Lett. **79**, 325 (1997).

[4] R. P. Feynman., Int. J. Theor. Phys. **21**, 467 (1982).

[5] S. Lloyd., Science **273**, 1073 (1996).

[6] K. L. Brown, W. J. Munro, and V. M. Kendon., Entropy 2010 **12**, 2268 (2010).

[7] C. H. Bennett and G. Brassard. In Proceedings of IEEE International Conference on Computers, Systems and Signal Processing, Bangalore, India, pp. 175179. IEEE, New York (1984).

[8] N. Gisin, G. Ribordy, W. Tittel, and H. Zbinden., Rev. Mod. Phys. 74, 145 (2002).

[9] N. Gisin and R. Thew., Nature Photon. 1, 165 (2007).

[10] V. Giovannetti, S. Lloyd, and L. Maccone, Nature Photonics **5**, 222229 (2011).

[11] M. F. Riedel et al., Nature **464**, 1170 (2010).

[12] C. Gross, T. Zibold, E. Nicklas, J. Esteve, and M. K. Oberthaler, Nature **464**, 1165 (2010).

[13] N. Bohr, Nature **136**, 65 (1935).

[14] A. Einstein, B. Podolsky, and N. Rosen, Phys. Rev. **47**, 777 (1935).

[15] E. Schrödinger, Naturwissenschaften, **23**, 812 (1935).

[16] E. Joos, et al. "Decoherence and the Appearance of a Classical World in Quantum Theory", Springer (2003).

[17] W. H. Zurek, Rev. Mod. Phys. **75**, 715 (2003).

[18] M. Arndt, and K. Hornberger, Nature Physics **10**, 271 (2014).

[19] A. Bassi, K. Lochan, S. Satin, T. P. Singh, and H. Ulbricht, Rev. Mod. Phys. **85**, 471 (2013).

[20] A.I Lvovsky, B.C. Sanders and W. Tittel, Nature Photonics **3**, 706 (2009).

[21] K. Hammerer, A.S. Srensen, E.S. Polzik, Rev. Mod. Phys **82**, 1041 (2010).

[22] C. Simon et al., Eur. Phys. J. D **58**, 1 (2010).

[23] H. Mabuchi and A. C. Doherty, Science 298, 1372 (2002).

[24] J. M. Raimond, M. Brune, and S. Haroche, Rev. Mod. Phys., **73** 565 (2001).

[25] A. Kuhn, M. Hennrich, and G. Rempe., Phys. Rev. Lett. **89** 067901 (2002).

[26] AD Boozer, A. Boca, R. Miller, TE Northup, and HJ Kimble., Physical Review Letters, **98** 193601 (2007).

[27] J. Bochmann, M. Muecke, G. Langfahl-Klabes, C. Erbel, B. Weber, H. P. Specht, D. L. Moehring, and G. Rempe, Phys. Rev. Lett., **67**1727 (2008).

[28] K. Hammerer, A. S. Sørensen, and E. S. Polzik, Rev. Mod. Phys. **8**2, 1041 (2010).

[29] N. Sangouard, C. Simon, H. de Riedmatten, and N. Gisin, Rev. Mod. Phys. **83**, 33 (2011).

[30] Fleischhauer M and Lukin M D, Phys. Rev. A **65** 022314 (2002)

[31] Nunn J, Walmsley I A, Raymer M G, Surmacz K, Waldermann F C, Wang Z and Jaksch D, Phys. Rev. A **75** 011401 (2007)

[32] Gorshkov A V, Andre A, Fleischhauer M, Sørensen A S and Lukin M D, Phys. Rev. Lett. **98** 123601 (2007).

[33] Reim K F, Nunn J, Lorenz V O, Sussman B J, Lee K C, Langford N K, Jaksch D and Walmsley I A, Nature Photon. **4** 218 (2010)

[34] Kurnit N A, Abella I D and Hartmann S R, Phys. Rev. Lett. **13** 567 (1964)

[35] Afzelius M, Simon C, de Riedmatten H and Gisin N, Phys. Rev. A **79** 052329 (2009)

[36] Sangouard N, Simon C, Afzelius M and Gisin N Phys. Rev. A **75** 032327 (2007)

[37] Longdell J J, Hetet G, Lam P K and Sellars M J, Phys. Rev. A **78** 032337 (2008)

[38] H. Schmidt, A. Imamoglu, Optics Letters **21**, 23 (1996).

[39] M.D. Lukin, A. Imamoglu, PRL **84**, 7 (1999).

[40] V Venkataraman, K Saha, AL Gaeta, Nature Photonics **7**, 138(2013).

[41] A. Rispe, B. He, and C. Simon , Phys. Rev. Lett. **107**, 043601 (2011).

[42] Q. A. Turchette, C. J. Hood, W. Lange, H. Mabuchi, H. J. Kimble, Phys. Rev. Lett. **75**, 4710 (1995).

[43] L.-M. Duan, H. J. Kimble, Phys. Rev. Lett. **92**, 127902 (2004).

[44] M. Saffman, T. G. Walker, and K. Mølmer, Rev. Mod. Phys. **82**, 2313 (2010).

[45] D. Tiarks, S. Schmidt, G. Rempe, S. Dürr, arXiv:1512.05740 (2016).

[46] M. Kitagawa and M. Ueda, Phys. Rev. A **47**, 5138 (1993).

[47] D. J. Wineland, W. M. Itano, F. L. Moore, and D. J. Heinzen, Phys. Rev. A **46**, 6797(R) (1992).

[48] D. J. Wineland, J. J. Bollinger, W. M. Itano, and D. J. Heinzen, Phys. Rev. A **50**, 67 (1994).

[49] V. Meyer, M. A. Rowe, D. Kielpinski, C. A. Sackett, W. M. Itano, C. Monroe, and D. J. Wineland, Phys. Rev. Lett. **86**, 5870 (2001).

[50] A. Kuzmich and T. A. B. Kennedy, Phys. Rev. Lett. **92**, 030407 (2004).

[51] A. Sørensen, L.M. Duan, J. I. Cirac, and P. Zoller, Nature **409**, 63 (2001).

[52] S. D. Jenkins and T. A. B. Kennedy, Phys. Rev. A **66**, 043621 (2002).

[53] J. Estéve, C. Gross, A. Weller, S. Giovanazzi, and M. K. Oberthaler, Nature **455**, 1216 (2008).

[54] M. F. Riedel, P. Böhi, Y. Li, T. W. Hänsch, A. Sinatra, and P. Treutlein, Nature **464**, 1170 (2010).

[55] H. W. Lau, Z. Dutton, T. Wang, and C. Simon, Phys. Rev. Lett. **113**, 090401 (2014).

[56] J. D. Pritchard, K. J. Weatherill, C. S. Adams, Non-linear optics using cold Rydberg atoms, Annual Review of Cold Atoms and Molecules 1, **301** (2013).

[57] M Khazali, K Heshami, C Simon, Phys. Rev. A (R) **91**, 030301 (2015).

[58] D. Paredes-Barato and C. S. Adams Phys. Rev. Lett. **112**, 040501 (2014).

[59] S. Das, A. Grankin, I. Iakoupov, E. Brion, J. Borregaard, R. Boddeda, I. Usmani, A. Ourjoumtsev, P. Grangier, and A. S. Srensen, Phys. Rev. A **93**, 040303(R) (2016).

[60] M. Saffman, and K. Mølmer, Phys. Rev. Lett. **102**, 240502 (2009).

[61] T. Opatrný, and K. Mølmer, Phys. Rev. A **86**, 023845 (2012).

[62] R. Mukherjee, J. Millen, R. Nath, M.P.A Jones, and T. Pohl, J. Phys. B: At. Mol. Opt. Phys. **44** 184010 (2011).

[63] H Kaviani, M Khazali, R Ghobadi, E Zahedinejad, K Heshami and C Simon, New J. Phys. **15** 085029 (2013).

[64] M. Khazali, H. W. Lau, A. Humeniuk, C. Simon, arXiv:1509.01303v2 (2015).

[65] M. O. Scully, M. S. Zubairy, "Quantum Optics", Cambridge University Press (1997).

[66] H. J. Kimble, Nature **453**, 1023 (2008).

[67] M. Jakobi, C. Simon, N. Gisin, J. Bancal, C. Branciard, N. Walenta, and H. Zbinden, Phys. Rev. A **83**, 022301 (2011).

[68] A. Broadbent, J. Fitzsimons, E. Kashefi FOCS (2009).

[69] P. Komar et. al. Nat. Phys. **10**, 582 (2014).

[70] D. Gottesman, T.Jennewein, and S. Croke Phys. Rev. Lett. **109**, 070503 (2012).

[71] M. A. Nielsen, I. L. Chuang, Quantum Computation and Quantum Information. Cambridge University Press (2010).

[72] W.K. Wootters and W.H. Zurek, Nature **299**, 802 (1982).

[73] H.J. Briegel, W. Dür, J. I. Cirac, and P. Zoller. Phys. Rev. Lett. **81**, 5932 (1998).

[74] N. Sangouard, C. Simon, H. d. Riedmatten, and N. Gisin, Rev. Mod. Phys. **83**, 33 (2011).

[75] R. Ursin, et. al., Nature Physics **3**, 481 (2007),

[76] B. Korzh, et. al. Nature Photonics **9**, 163 (2015).

[77] H. L. Yin, et. al., arXiv:1606.06821 (2016).

[78] A. K. Ekert. Phys. Rev. Lett. **67**, 661 (1991).

[79] C. H. Bennett, G. Brassard, C. Cré peau, R. Jozsa, A. Peres, W. K. Wootters, Phys. Rev. Lett. **70**, 1895 (1993).

[80] D. Bouwmeester, et al. Nature **390**, 575 (1997).

[81] L.M. Duan, M. D. Lukin, J. I. Cirac and P. Zoller, Nature **414**, 413 (2001)

[82] A.I Lvovsky, B.C. Sanders and W. Tittel, Nature Photonics **3**, 706 (2009)

[83] K. Hammerer, A.S. Sørensen, E.S. Polzik, Rev. Mod. Phys **82**, 1041 (2010)

[84] C. Simon et al., Eur. Phys. J. D **58**, 1 (2010)

[85] I. Rabi, J. R. Zacharias, S. Millman, and P. Kusch. A new method of measuring nuclear magnetic moment. Phys. Rev., **53** 318, (1938).

[86] M.Fleischhauer, M.D. Lukin, Phys. Rev. A **65**, 022314 (2002).

[87] J. Nunn, I. A. Walmsley, M.G. Raymer, K. Surmacz, F.C. Waldermann, Z. Wang, D. Jaksch, Phys. Rev. A **75**, 011401 (2007).

[88] A.V. Gorshkov, A. André, M. Fleischhauer, A.S. Sørensen, M.D. Lukin, Phys. Rev. Lett **98**, 123601 (2007).

[89] K.F. Reim, J. Nunn, V.O. Lorenz, B.J. Sussman, K.C. Lee, N.K Langford, D. Jaksch, I.A. Walmsley, Nature Photonics **4**, 218 (2010).

[90] N. Sangouard, C. Simon, M. Afzelius, N. Gisin, Phys. Rev. A **75**, 032327 (2007).

[91] M. Afzelius, C. Simon, H. de Riedmatten, N. Gisin, Phys. Rev. A **79**, 052329 (2009).

[92] M. Fleischhauer, A. Imamoglu, and J. P. Marangos, Reviews of Modern Physics, **77** 633 (2005).

[93] J. H. Eberly, M. L. Pons, and H. R. Haq, Phys. Rev. Lett., **72**, 56 (1994).

[94] S. H. Autler and C. H. Townes. Phys. Rev., **100** 703 (1955).

[95] M. Fleischhauer and M. D. Lukin. Phys. Rev. Lett., **84** 5094, (2000).

[96] C. Liu, Zachary Dutton, Cyrus H. Behroozi, and Lene Vestergaard Hau, Nature, **409** 490 (2001).

[97] K. S. Choi, H. Deng, J. Laurat, and H. J. Kimble. Nature, **452**, 67 (2008).

[98] J. Laurat, C. Chou, H. Deng, K. S. Choi, D. Felinto, H. Riedmatten, and H J Kimble, New Journal of Physics, **9** (2007).

[99] T. Chaneliere, D. N. Matsukevich, S. D. Jenkins, S.-Y. Lan, R. Zhao, T. A. B. Kennedy, and A. Kuzmich, Phys. Rev. Lett., **98** 113602 (2007).

[100] I. Novikova, et, al, Phys. Rev. A **78**, 021802(R) (2008).

[101] J. J. Longdell, G. Hétet, P.K. Lam, M.J. Sellars, Phys. Rev. A **78**, 032337 (2008)

[102] A.I Lvovsky, B.C. Sanders and W. Tittel, Nature Photonics **3**, 706 (2009)

[103] K. Hammerer, A.S. Sørensen, E.S. Polzik, Rev. Mod. Phys **82**, 1041 (2010)

[104] C. Simon et al., Eur. Phys. J. D **58**, 1 (2010)

[105] U.G. Kopvil'em and V.R. Nagibarov, Fiz. Metall.Metalloved **2**, 313 (1963)

[106] N.A. Kurnit, I. D. Abella, S. R. Hartmann, Phys. Rev. Lett **13**, 567 1964

[107] K. Heshami, A. Green, Y. Han, A. Rispe, E. Saglamyurek, N. Sinclair, W. Tittel, C. Simon, Phys. Rev. A **86**, 013813 (2012)

[108] J. Clark, K. Heshami, C. Simon, Phys. Rev. A **86**, 013833 (2012)

[109] M. Fleischhauer, M.D. Lukin, Phys. Rev. Lett **84**, 5094 (2000)

[110] M.R.Sprague, D. G. England, A. Abdolvand, J. Nunn, X. Jin, W. S. Kolthammer, M. Barbieri, B. Rigal, P. S. Michelberger, T. F. M. Champion, P. S. J. Russell, I. A. Walmsley, New J. Phys., **15** 055013 (2013).

[111] M. Bajcsy, S. Hofferberth, V. Balic, T. Peyronel, M. Hafezi, A. S. Zibrov, V. Vuletic, M. D. Lukin, Phys. Rev. Lett. **102**, 203902 (2009).

[112] M. Bajcsy, S. Hofferberth, T. Peyronel, V. Balic, Q. Liang, A. S. Zibrov, V. Vuletic, M. D. Lukin, Phys. Rev. A **83**, 063830 (2011).

[113] G. Hétet, J.J. Longdell, M.J. Sellars, P.K. Lam, B.C. Buchler, Phys. Rev. Lett. **101**, 203601 (2008)

[114] G. Hétet, D. Wilkowski, T. Chanelire, New J. Phys. **15** 045015 (2013).

[115] M.F. Yanik, S.Fan, Phys. Review. Lett **92**, 083901 (2004)

[116] J. Balmer, Annalen der Physik und Chemie **25**, 80 (1885).

[117] N. Bohr, Philosophical Magazine Series 6 **26**, 1 (1913).

[118] R. Löw, H. Weimer, J. Nipper, J. B. Balewski, B. Butscher, H. P. Büchler, T. Pfau, Journal of Physics B: Atomic, Molecular and Optical Physics **45**, 113001 (2012).

[119] M. Saffman, T. G. Walker, K. Mølmer, Quantum information with Rydberg atoms, Rev. Mod. Phys. **82**, 2313 (2010).

[120] T. Killian, T. Pattard, T. Pohl, J. Rost, Physics Reports **449**, 130 (2007).

[121] S. L. Rolston, Physics **1**, 2 (2008).

[122] V. Bendkowsky, B. Butscher, J. Nipper, J. P. Shaffer, R. Löw, T. Pfau, Nature **458**, 1005 (2009).

[123] G. Pupillo, A. Micheli, M. Boninsegni, I. Lesanovsky, P. Zoller, Phys. Rev. Lett. **104**, 223002 (2010).

[124] N. Henkel, R. Nath, T. Pohl, Phys. Rev. Lett. **104**, 195302 (2010).

[125] M Khazali, HW Lau, A Humeniuk, C Simon, arXiv:1509.01303 (2016).

[126] L. I. R. Gil, R. Mukherjee, E. M. Bridge, M. P. A. Jones, and T. Pohl, Phys. Rev. Lett. **112**, 103601 (2014).

[127] B. Huber, T. Baluktsian, M. Schlagmller, A. Kölle, H. Kübler, R. Löw, and T. Pfau Phys. Rev. Lett. **107**, 243001 (2011).

[128] T. Kazimierczuk, D. Fröhlich, S. Scheel, H. Stolz, and M. Bayer, Nature **514**, 343 (2014).

[129] A. Chernikov, T. C. Berkelbach, H. M. Hill, A. Rigosi, Y. Li, O. B. Aslan, D. R. Reichman, M. S. Hybertsen, and T. F. Heinz, Phys. Rev. Lett. **113**, 076802 (2014).

[130] B. Bransden and C. Joachain. Physics of Atoms and Molecules. Addison Wesley Longman, 2 edition, (2003).

[131] J. Han, Y. Jamil, D. V. L. Norum, P. J. Tanner, and T. F. Gallagher. Phys. Rev. A **74**, 054502, (2006).

[132] W. Li, I. Mourachko, M. W. Noel, and T. F. Gallagher. Phys. Rev. A **67**, 052502, (2003).

[133] J. E. Mayer and M. G. Mayer, Phys. Rev. **43**, 605 (1933).

[134] M. Marinescu, H. R. Sadeghpour, and A. Dalgarno, Phys. Rev. A **49**, 982 (1994).

[135] R. W. Molof, H. L. Schwartz, T. M. Miller, and B. Bederson, Phys. Rev. A **10**, 1131 (1974).

[136] J. Han, Y. Jamil, D. V. L. Norum, P. J. Tanner, and T. F. Gallagher, Phys. Rev. A 74, 054502 (2006).

[137] W. E. Cooke, T. F. Gallagher, R. M. Hill, and S. A. Edelstein, Phys. Rev. A **16**, 1141 (1977).

[138] J. Lahiri and A. Mukherji, Phys. Rev. **153**, 386 (1967).

[139] S. A. Bhatti, C. L. Cromer, and W. E. Cooke, Phys. Rev. A **24**, 161 (1981).

[140] J. M. Blatt, **1**, 382 (1967)

[141] T. G. Walker and M. Saffman Phys. Rev. A **77**, 032723 (2008).

[142] H. Friedrich. Theoretical Atomic Physics. Springer, Berlin, 1994.

[143] G. Racah. Theory of Complex Spectra. II. Phys. Rev. **62**, 438 (1942).

[144] N. Henkel, PhD thesis, Technische Universität Dresden (2013).

[145] C L Vaillant, M P A Jones and R M Potvliege, Journal of Physics B: Atomic, Molecular and Optical Physics, **47**, 15 (2014).

[146] I. I. Beterov, I. I. Ryabtsev, D. B. Tretyakov, and V. M. Entin, Phys. Rev. A **79**, 052504 (2009).

[147] R. Low *et al.*, J. Phys. B: Atom. Mole. Opt. **45** (2012).

[148] C. Vaillant, PhD thesis, Durham University (2014).

[149] E. Urban, T. A. Johnson, T. Henage, L. Isenhower, D. D. Yavuz, T. G. Walker and M. Saffman, Nature Physics **5**, 110 (2009).

[150] J B Balewski, A T Krupp, A Gaj, S Hofferberth, R Löw and T Pfau, New Journal of Physics, **16**, (2014).

[151] V. Vuletic, Nature Phys. **2**, 801 (2006).

[152] A. Gaëtan, et. al., Nature Physics **5**, 115 (2009).

[153] B. Zhao, M. Müller, K. Hammerer, and P. Zoller Phys. Rev. A **81**, 052329 (2010).

[154] E. Knill, R. Laflamme, G. J. Milburn, Nature **409**, 46 (2001).

[155] R. Raussendorf and, H.J. Briegel, Phys. Rev. Lett. **86**, 5188 (2001).

[156] MA Nielsen , Rep. Math. Phys. **57**, 147 (2006).

[157] D.E. Browne, T. Rudolph, Phys. Rev. Lett. **95**, 010501 (2005).

[158] H. Schmidt, A. Imamoglu, Optics Letters **21**, 23 (1996).

[159] M.D. Lukin, A. Imamoglu, PRL **84**, 7 (1999).

[160] V Venkataraman, K Saha, AL Gaeta, Nature Photonics **7**, 138(2013).

[161] A. Rispe, B. He, and C. Simon , Phys. Rev. Lett. **107**, 043601 (2011).

[162] Q. A. Turchette, C. J. Hood, W. Lange, H. Mabuchi, and H. J. Kimble, Phys. Rev. Lett. **75**, 4710 (1995).

[163] L.-M. Duan and H. J. Kimble, Phys. Rev. Lett. **92**, 127902 (2004).

[164] M. Saffman and T. G. Walker, Phys. Rev. A **72**, 022347 (2005)

[165] D. Jaksch, J.I. Cirac, P. Zoller, S.L. Rolston, R. Cote, and M. D. Lukin, Phys. Rev. Lett. **85**, 2208 (2000)

[166] M. D. Lukin, M. Fleischhauer, R. Cote, L. M. Duan, D. Jaksch, J. I. Cirac, and P. Zoller, Phys. Rev. Lett. **87**, 037901 (2001)

[167] M. Müller, I. Lesanovsky, H. Weimer, H. P. Büchler, and P. Zoller, Phys. Rev. Lett. **102**, 170502 (2009)

[168] L. Isenhower, M. Saffman, and K. K. Mølmer, Quant. Info. Pro. **10**, 755 (2011)

[169] M. Saffman, T. G. Walker, and K. Mølmer, Rev. Mod. Phys. **82**, 2313 (2010).

[170] L. Isenhower, E. Urban, X. L. Zhang, A. T. Gill, T. Henage, T. A. Johnson, T. G. Walker, and M. Saffman, Phys. Rev. Lett. **104**, 010503 (2010)

[171] T. Wilk, A. Gaëtan, C. Evellin, J. Wolters, Y. Miroshnychenko, P. Grangier, and A. Browaeys, Phys. Rev. Lett. **104**, 010502 (2010)

[172] Y. O. Dudin and A. Kuzmich, Science **336**, 887 (2012),

[173] T. Peyronel, O. Firstenberg, Q. Y. Liang, S. Hofferberth, A. V. Gorshkov, T. Pohl, M. D. Lukin, and V. Vuletić, Nature **488**, 57 (2012)

[174] D. Maxwell, D. J. Szwer, D. Paredes-Barato, H. Busche, J. D. Pritchard, A. Gauguet, K. J. Weatherill, M. P. A. Jones, and C. S. Adams, Phys. Rev. Lett. **110**, 103001 (2013).

[175] S. Sevinçli, C. Ates, T. Pohl, H. Schempp, C. S. Hofmann, G. Günter, T. Amthor, M. Weidemüller, J. D. Pritchard, D. Maxwell, A. Gauguet, K. J. Weatherill, M. P. A. Jones, and C. S. Adams, At. Mol. Opt. Phys. **44**, 184018 (2011)

[176] V. Parigi, E. Bimbard, J. Stanojevic, A.J. Hilliard, F. Nogrette, R. Tualle-Brouri, A. Ourjoumtsev, and P. Grangier, Phys. Rev. Lett. **109**, 233602 (2012)

[177] C. S. Hofmann, G. Günter, H. Schempp, M. Robert-de-Saint-Vincent, M. Gärttner, J. Evers, S. Whitlock, and M. Weidemüller, Phys. Rev. Lett. **110**, 203601 (2013).

[178] Y. O. Dudin, L. Li, F. Bariani, and A. Kuzmich, Nature Physics **8**, 790 (2012)

[179] A. V. Gorshkov, J. Otterbach, M. Fleischhauer, T. Pohl, and M. D. Lukin, Phys. Rev. Lett. **107**, 133602 (2011).

[180] O. Firstenberg, T. Peyronel, Q. Y. Liang, A. V. Gorshkov, M. D. Lukin, and V.Vuletić, Nature **502**, 71 (2013)

[181] I. Friedler, D. Petrosyan, M. Fleischhauer and G. Kurizki, Phys. Rev. A **72**, 043803 (2005)

[182] E. Shahmoon, G. Kurizki, M. Fleischhauer and D. Petrosyan, Phys. Rev. A **83**, 033806 (2011)

[183] B. He, A. MacRae, Y. Han, A. I. Lvovsky, and C. Simon, Phys. Rev. A **83**, 022312 (2011)

[184] B. He, A. V. Sharypov, J. Sheng, C. Simon, and M. Xiao, Phys. Rev. Lett. **112**, 133606 (2014)

[185] D. Paredes-Barato and C. S. Adams, Phys. Rev. Lett. **112**, 040501 (2014)

[186] I. L. Chuang and Y. Yamamoto, Phys. Rev. A **52**, 3489 (1995)

[187] C.S.E. van Ditzhuijzen, A.F. Koenderink, J.V. Hernández, F. Robicheaux, L.D. Noordam, and H.B. van Linden van den Heuvell, Phys. Rev. Lett. **100**, 243201 (2008).

[188] J. Han and T. F. Gallagher, Phys. Rev. A **79**, 053409 (2009).

[189] T. G. Walker and M. Saffman, Phys. Rev. A **77**, 032723 (2008)

[190] A. Reinhard, T. C. Liebisch, B. Knuffman, and G. Raithel, Phys. Rev. A **75** 032712 (2007)

[191] F. Maucher, N. Henkel, M. Saffman, W. Krolikowski, S. Skupin, and T. Pohl, Phys. Rev. Lett. **106** 170401(2011)

[192] C. Simon *et al.*, Eur. Phys. J. D **58**, 1 (2010).

[193] S. D. Jenkins, T. Zhang, and T. A. B. Kennedy, J. Phys. B **45**, 124005 (2012)

[194] J. B. Balewski, A. T. Krupp, A. Gaj, D. Peter, H.P. Büchler, R. Löw, S. Hofferberth, and T. Pfau, Nature **502**, 664 (2013).

[195] A.V. Gorshkov, A. André, M.D. Lukin, and A. S. Sørensen, Phys. Rev. A **76**, 033805 (2007).

[196] M. Saffman and T. G. Walker, Phys. Rev. A **66**, 065403 (2002)

[197] Y. Han, B. He, K. Heshami, C. Li, and C. Simon, Phys. Rev. A **81**, 052311 (2010)

[198] Note that for EIT storage the collective excitations are compressed in the direction of propagation compared to the input and output photon wave packets. However, given that both the initial wave packets and the effective interaction in Eq. (3) are separable with respect to the parallel and perpendicular dimensions, this compression has no effect on the photon-photon gate fidelity.

[199] D. Tiarks, S. Baur, K. Schneider, S. Dürr, and G. Rempe, Phys. Rev. Lett. **113**, 053602 (2014); H. Gorniaczyk, C. Tresp, J. Schmidt, H. Fedder, and S. Hofferberth, Phys. Rev. Lett. **113**, 053601 (2014).

[200] S. D. Jenkins, T. Zhang, T. A. B. Kennedy, J. Phys. B **45**, 124005 (2012)

[201] M. Saffman, T. G. Walker, and K. Mølmer, Rev. Mod. Phys. **82**, 2313 (2010)

[202] B. Huber, T. Baluktsian, M. Schlagmüller, A. Kölle, H. Kübler, R. Löw, and T. Pfau, Phys. Rev. Lett. **110**, 123001 (2013).

[203] C. Monroe, D. M. Meekhof, B. E. King, and D. J. Wineland, Science **272**, 1131 (1996).

[204] M. Brune, E. Hagley, J. Dreyer, X. Matre, A. Maali, C. Wunderlich, J. M. Raimond, and S. Haroche, Phys. Rev. Lett. **77**, 4887 (1996).

[205] G. S. Agarwal, R. R. Puri, and R. P. Singh, Phys. Rev. A **56**, 2249 (1997).

[206] M. Arndt, O. Nairz, J. Vos-Andreae, C. Keller, G. van der Zouw, and A. Zeilinger, Nature **401**, 680 (1999).

[207] A. Sørensen, and K. Mølmer, Phys. Rev. Lett. **82**, 1971 (1999).

[208] J. R. Friedman, V. Patel, W. Chen, S. K. Tolpygo, and J. E. Lukens, Nature **406**, 43 (2000).

[209] B. Julsgaard, A. Kozhekin, and E. S. Polzik, Nature **413**, 400 (2001).

[210] J. Estève, C. Gross, A. Weller, S. Giovanazzi, and M. K. Oberthaler, Nature **455**, 1216 (2008).

[211] M. F. Riedel, P. Böhi, Y. Li, T. W. Hänsch, A. Sinatra, and P. Treutlein, Nature **464**, 1170 (2010).

[212] A. D. O'Connell, M. Hofheinz, M. Ansmann, R. C. Bialczak, M. Lenander, E. Lucero, M. Neeley, D. Sank, H. Wang, M. Weides, et al., Nature **464**, 697 (2010).

[213] A. I. Lvovsky, R. Ghobadi, A. Chandra, A. S. Prasad, and C. Simon, Nature Physics **9**, 541 (2013).

[214] N. Bruno, A. Martin, P. Sekatski, N. Sangouard, R. T. Thew, and N. Gisin, Nature Physics **9**, 545 (2013).

[215] T. A. Palomaki, J. D. Teufel, R. W. Simmonds, and K. W. Lehnert, Science **342**, 710 (2013).

[216] B. Vlastakis, G. Kirchmair, Z. Leghtas, S. E. Nigg, L. Frunzio, S. M. Girvin, M. Mirrahimi, M. H. Devoret, and R. J. Schoelkopf, Science **342**, 607 (2013).

[217] M. Arndt and K. Hornberger, Nature Physics **10**, 271, (2014).

[218] H. W. Lau, Z. Dutton, T. Wang, and C. Simon, Phys. Rev. Lett. **113**, 090401 (2014).

[219] G.J. Milburn, Phys. Rev. A **44**, 5401 (1991).

[220] R. Gambini, R.A. Porto, and J. Pullin, Classical Quantum Gravity **21**, L51 (2004).

[221] M.P. Blencowe, Phys. Rev. Lett. **111**, 021302 (2013).

[222] J.E. Johnson and S.L. Rolston, Phys. Rev. A **82**, 033412 (2010).

[223] J.B. Balewski, A.T. Krupp, A. Gaj, S. Hofferberth, R. Löw, and T. Pfau, New J. Phys. **16** 063012 (2014).

[224] B. Yurke and D. Stoler, Phys. Rev. Lett. **57**, 13 (1986).

[225] C. Simon, D. Jaksch, Phys. Rev. A **70**, 052104 (2004).

[226] R. Ghobadi, A. Lvovsky, and C. Simon, Phys. Rev. Lett. **110**, 170406 (2013).

[227] T. Monz et al., Phys. Rev. Lett. **106**, 130506 (2011).

[228] M. Saffman, and K. Mølmer, Phys. Rev. Lett. **102**, 240502 (2009).

[229] T. Opatrný, and K. Mølmer, Phys. Rev. A **86**, 023845 (2012).

[230] R. Mukherjee, J. Millen, R. Nath, M.P.A Jones, and T. Pohl, J. Phys. B: At. Mol. Opt. Phys. **44** 184010 (2011).

[231] R. Mukherjee, PhD thesis, Technische Universität Dresden (2013).

[232] T. Akatsuka, M. Takamoto, and H. Katori, Nature Physics **4**, 954 (2008).

[233] Y. O. Dudin, L. Li, F. Bariani, and A. Kuzmich, Nature Phys. **8**, 790 (2012).

[234] J. Ma, X. Wang, C. P. Sun, and F. Nori, Physics Reports, **509**, 89 (2011).

[235] D.A.R. Dalvit, J. Dziarmaga, and W.H. Zurek, Phys. Rev. A **62**, 013607 (2000).

[236] L.I.R. Gil, R. Mukherjee, E.M. Bridge, M.P.A. Jones, and T. Pohl, Phys. Rev. Lett. **112**, 103601 (2014).

[237] N. Henkel, R. Nath, and T. Pohl, Phys. Rev. Lett. **104**, 195302 (2010).

[238] M. Takamoto, H. Katori, S. I. Marmo, V. D. Ovsiannikov, and V. G. Pal'chikov, Phys. Rev. Lett. **102**, 063002 (2009).

[239] I. Ushijima, M. Takamoto, M. Das, T. Ohkubo, and H. Katori, Nature Photonics **9**, 185 (2015); J. M. Raimond, M. Brune, and S. Haroche, Rev. Mod. Phys. **73**, 565 (2001).

[240] Y. N. Martinez, Masters Thesis, Rice University (2005).

[241] S. Ye, X. Zhang, T. C. Killian, F. B. Dunning, M. Hiller, S. Yoshida, S. Nagele, and J. Burgdörfer, Phys. Rev. A **88**, 043430 (2013).

[242] J. Millen, G. Lochead and M. P. A. Jones, Phys. Rev. Lett **105**, 213004 (2010).

[243] P. McQuillen, X. Zhang, T. Strickler, F. B. Dunning, and T. C. Killian, Phys. Rev. A **87**, 013407 (2013).

[244] G. Lochead, D. Boddy, D. P. Sadler, C. S. Adams, and M. P. A. Jones, Phys. Rev. A **87**, 053409 (2013).

[245] Y.Y. Jau, A. M. Hankin, T. Keating, I. H. Deutsch, and G. W. Biedermann, Nature Physics **12**, 71 (2016).

[246] J. Zeiher, R. van Bijnen, P. Schauß, S. Hild, J. Choi, T. Pohl, I. Bloch, C. Gross, arXiv:1602.06313, (2016)

[247] A. Wilson, C. Ospelkaus, A. P. VanDevender, J. A. Mlynek, K. R. Brown, D. Leibfried, and D. J. Wineland, Appl. Phys. B **105**, 741 (2011).

[248] D. B. Hume, I. Stroescu, M. Joos, W. Muessel, H. Strobel, and M. K. Oberthaler, Phys. Rev. Lett. **111**, 253001 (2013).

[249] J. B. Balewski, A. T. Krupp, A. Gaj, D. Peter, H. P. Büchler, R. Löw, S. Hofferberth and T. Pfau, Nature **502**, 664 (2013).

[250] T. Niederprüm, O. Thomas, T. Manthey, T. M. Weber and H. Ott, arXiv:1503.01586 (2015).

[251] T. Keating, K. Goyal, Y. Jau, G. W. Biedermann, A. J. Landahl, and I. H. Deutsch, Phys. Rev. A **87**, 052314 (2013).

[252] R. M. W. van Bijnen, and T. Pohl, arXiv:1411.3118 (2014).

[253] Y.Y. Jau, A. M. Hankin, T. Keating, I. H. Deutsch, and G. W. Biedermann, arXiv:1501.03862 (2015).

[254] I. Ushijima, M. Takamoto, M. Das, T. Ohkubo, and H. Katori, Nature Photonics **9**, 185 (2015).

[255] J. M. Raimond, M. Brune, and S. Haroche, Rev. Mod. Phys. **73**, 565 (2001).

[256] E.A. Goldschmidt, T. Boulier, R.C. Brown, S.B. Koller, J.T. Young, A.V. Gorshkov, S.L. Rolston, and J.V. Porto, Phys. Rev. Lett. **116**, 113001 (2016).

[257] T. Monz *et al.*, Phys. Rev. Lett. **106**, 130506 (2011).

[258] M. Bishof, X. Zhang, M. J. Martin, and J. Ye, Phys. Rev. Lett. **111**, 093604 (2013).

[259] M. J. Martin, D. Meiser, J. W. Thomsen, J. Ye, and M. J. Holland, Phys. Rev. A **84**, 063813 (2011).

[260] D. Meiser, J. Ye, D. R. Carlson, and M. J. Holland, Phys. Rev. Lett. **102**, 163601 (2009).

[261] M. A. Norcia, M. N. Winchester, J. R. K. Cline, J. K. Thompson, arXiv:1603.05671 (2016).

[262] B. J. Bloom, T. L. Nicholson, J. R. Williams, S. L. Campbell, M. Bishof, X. Zhang, W. Zhang, S. L. Bromley, and J. Ye, Nature **506**, 71 (2014).

[263] H. Katori, M. Takamoto, V. G. Palchikov, and V. D. Ovsiannikov, Phys. Rev. Lett. **91**, 173005 (2003).

[264] M. Takamoto, H. Katori, S. I. Marmo, V. D. Ovsiannikov, and V. G. Palc̀hikov, Phys. Rev. Lett. **102**, 063002 (2009).

[265] W. Happer and B. S. Mathur, Phys. Rev. **163**, 12 (1967).

[266] T. Akatsuka, M. Takamoto, and H. Katori, Nature Physics **4**, 954 (2008).

[267] S. Baur, D. Tiarks, G. Rempe, and S. Dürr, Phys. Rev. Lett. **112**, 073901 (2014).

[268] F. Maucher, N. Henkel, M. Saffman, W. Królikowski, S. Skupin, and T. Pohl, Phys. Rev. Lett. **106**, 170401 (2011).

[269] A. W. Glaetzle, M. Dalmonte, R. Nath, I. Rousochatzakis, R. Moessner, and P. Zoller, Phys. Rev. X **4**, 041037 (2014).

[270] N. Henkel, F. Cinti, P. Jain, G. Pupillo, and T. Pohl Phys. Rev. Lett. **108**, 265301 (2012).

[271] A. Angelone, F. Mezzacapo, and G. Pupillo Phys. Rev. Lett. **116**, 135303 (2016).

[272] M. Mattioli, M. Dalmonte, W. Lechner, and G. Pupillo Phys. Rev. Lett. **111**, 165302 (2013).